CHEMICAL REVIEWS

pubs.acs.org/CR

Review

# Emerging Atomistic Modeling Methods for Heterogeneous Electrocatalysis

*Published as part of Chemical Reviews virtual special issue "Green Hydrogen".*

Zachary Levell,[§] Jiabo Le,[§] Saerom Yu, Ruoyu Wang, Sudheesh Ethirajan, Rachita Rana, Ambarish Kulkarni,* Joaquin Resasco,* Deyu Lu,* Jun Cheng,* and Yuanyue Liu*

Cite This: *Chem. Rev.* 2024, 124, 8620–8656

Read Online

ACCESS | Metrics & More | Article Recommendations

**ABSTRACT:** Heterogeneous electrocatalysis lies at the center of various technologies that could help enable a sustainable future. However, its complexity makes it challenging to accurately and efficiently model at an atomic level. Here, we review emerging atomistic methods to simulate the electrocatalytic interface with special attention devoted to the components/effects that have been challenging to model, such as solvation, electrolyte ions, electrode potential, reaction kinetics, and pH. Additionally, we review relevant computational spectroscopy methods. Then, we showcase several examples of applying these methods to understand and design catalysts relevant to green hydrogen. We also offer experimental views on how to bridge the gap between theory and experiments. Finally, we provide some perspectives on opportunities to advance the field.

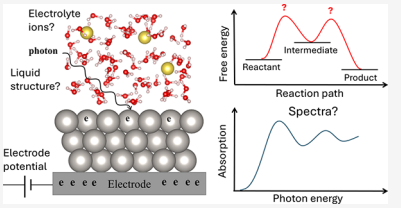




## CONTENTS



## 1. INTRODUCTION

Heterogeneous electrocatalysis lies at the center of various technologies for renewable energy conversion and storage,

Received: October 8, 2023
Revised: May 27, 2024
Accepted: June 10, 2024
Published: July 11, 2024

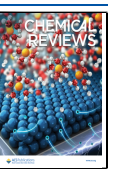




https://doi.org/10.1021/acs.chemrev.3c00735
*Chem. Rev.* 2024, 124, 8620–8656

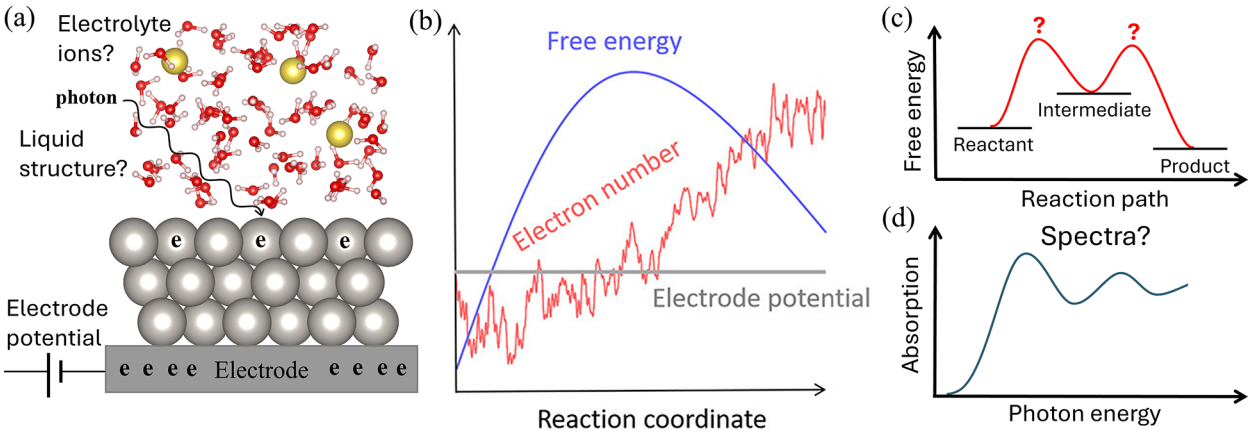


**Figure 1.** (a) Atomistic modeling of heterogeneous electrocatalysis is challenging due to complexities including "liquid structure", "electrolyte ions", and "electrode potential". (b) Electron number evolution during a reaction at fixed electrode potential. Adapted with permission from ref 2. Copyright 2022 American Chemical Society. (c and d) Schematics of the energy evolution and spectroscopic signature.

sustainable manufacturing, and environmental remediation. For example, water electrolysis utilizes the hydrogen evolution reaction (HER) and oxygen evolution reaction (OER) to produce green hydrogen. Most fuel cells rely on the oxygen reduction reaction (ORR) and hydrogen oxidation reaction (HOR) to transform chemical energy into electrical energy. Carbon dioxide reduction ($CO_2R$) converts the greenhouse gas $CO_2$ to valuable chemicals. Nitrate reduction ($NO_3R$) converts the common water pollutant nitrate to important agricultural fertilizer ammonia.

However, existing catalyst systems generally suffer from low activity, selectivity, stability, and/or high cost, which necessitates a better understanding of the performance-limiting factors to facilitate rational design. To achieve this goal, it is important to develop computational tools for understanding and designing catalysts at the atomic level.

Atomistic modeling of heterogeneous electrocatalysis is challenging. As illustrated in Figure 1a, the model includes several critical components: the catalyst surface, the liquid solution, and the electrode potential. The liquid solvent (typically water) has numerous atomic configurations, which are difficult to sufficiently sample. The solvated ions have complex distributions and can strongly affect some reactions. The catalyst can have diverse active site structures, which may change under reaction conditions. The electrode serves as an electron reservoir, which exchanges electrons with the catalyst−liquid system to align their Fermi levels. Since the electrode potential (which determines the electrode's Fermi level) is fixed externally over the time scales of most elementary processes in the catalyst−liquid system and electron exchange is often much faster than these time scales,[1] the electrons in the system should be treated using the grand canonical ensemble (GCE) when modeling these processes. An important consequence is that the number of electrons in the system can change during the process, as shown in Figure 1b. This is distinct from most thermal processes, which instead have a constant number of electrons.

These structural and electronic complexities make atomistic modeling very challenging and hinders accurate calculation of the reaction energy profile (see Figure 1c). To make the calculations more feasible, many studies employ various levels of simplification. Although they have offered valuable insights and enable high throughput screening of catalysts, they fail to explain many important phenomena. Recently, several advanced models have emerged to more effectively describe heterogeneous electrocatalysis, particularly the computationally challenging components and effects such as solvation, electrolyte ions, electrode potential, reaction kinetics, and pH. It is therefore useful to compare these models and demonstrate how they can be used to better understand and predict catalysis. In addition, most computational studies focus on the structures and energetics, while few calculate the spectra (e.g., X-ray absorption spectroscopy (XAS), as illustrated in Figure 1d), which can offer important information about catalysis. Thus, we also review methods for computational spectroscopy with a focus on XAS. We further provide experimental views on how to bridge the gap between theory and experiments. Finally, we provide some perspectives on opportunities to advance the field.

## 2. METHODS

### 2.1. Liquid Solution

Liquid solutions can be modeled implicitly as a dielectric continuum, explicitly with full atomic descriptions, or a balance between these via hybrid models.

**2.1.1. Implicit Solution.** Implicit solvation models efficiently represent the solution by simplifying atomic details. A detailed review of implicit solvation models can be found elsewhere.[3] Here, we review some of the commonly used methods for electrified interfaces. Perhaps the most popular model is the polarizable continuum model, as implemented in VASPsol by Hennig et al.[4−6] In VASPsol, the simulation box is composed of an explicit DFT region and an implicit electrolyte region governed by a linearized Poisson−Boltzmann (PB) equation. These two regions are separated based on the electronic density so that the implicit electrolyte emerges as the electronic density decays. The total free energy $A$ of the system is expressed as

$$A[n(\vec{r}), \phi(\vec{r})] = A_{\mathrm{TXC}}[n(\vec{r})] + \int \phi(\vec{r})\rho_{\mathrm{s}}(\vec{r})\mathrm{d}^3r - \int \epsilon(\vec{r})\frac{|\nabla\phi|^2}{8\pi}\mathrm{d}^3r + \int \frac{1}{2}\phi(\vec{r})\rho_{\mathrm{ion}}(\vec{r})\mathrm{d}^3r + A_{\mathrm{cav}} + A_{\mathrm{ion}} \quad (1)$$

where $n(\vec{r})$ is the electronic charge density, $\phi(\vec{r})$ is the net electrostatic potential of the system, $A_{\mathrm{TXC}}$ is the kinetic and exchange-correlation energies, $\rho_{\mathrm{s}}(\vec{r})$ is the charge density of the DFT region, $\epsilon(\vec{r})$ is the relative permittivity of the electrolyte,


https://doi.org/10.1021/acs.chemrev.3c00735
Chem. Rev. 2024, 124, 8620−8656

$\rho_{ion}(\vec{r})$ is the charge density of the implicit electrolyte ions, $A_{cav}$ is the energy to form a cavity in the implicit solution (which the explicit region occupies), and $A_{ion}$ is the nonelectrostatic contribution to the free energy from the electrolyte ions. By minimizing the total energy, one obtains the ground state of the system.

Recently, Plaisance et al.[7,8] have improved VASPsol to VASPsol++. In particular, the "leakage" of the implicit solvent into small pores within explicit solvent is removed by defining the cavity of the implicit solvent in a nonlocal manner, and the Poisson−Boltzmann equation is extended to be nonlinear to better model the dielectric and ionic responses of highly charged electrodes. As such, these advancements of VASPsol have greatly enhanced the potential of implicit solvent models to simulate heterogeneous catalysis.

Another implicit solvation software is Environ[9−11] within Quantum ESPRESSO, which implements multiple continuum models, thereby having additional functionalities. For example, the implicit solution and the explicit quantum-mechanical region can be separated by electron density, atomic positions, or a nonlocal interface. Electrolyte ions can be modeled by the PB equation, the modified PB equation (MPB; which accounts for the steric repulsion between ions rather than treating them as points as in the original PB theory), or a user-specified charge distribution (e.g., planar charge).

In typical DFT calculations, the system is periodic in all 3 directions. However, real interfaces are not periodic along the direction perpendicular to the catalyst surface. To address this problem, Otani and co-workers[12] developed the effective screening medium (ESM) method, which modifies the Poisson solver part of DFT with the help of a Green's function technique. This removes the periodicity along the surface normal direction and allows for the use of the potential at infinite distance from the surface as the reference. The ESM can be combined with implicit solvation models such as PB/MPB[12] or the reference interaction site model (RISM)[13] to simulate the electrochemical interface. There are several other methods/codes to model the solution for the interface, such as the "solvated jellium" model (SJM; where the counter charge is uniformly distributed in a slab with a continuous dielectric)[14] in GPAW[15−18] and various models implemented in JDFTx[19,20] (e.g., CANDLE,[21] which defines the cavity with a nonlocal functional of the solute electron density and potential, thereby enabling an explicit treatment of the solvent charge asymmetry).

**2.1.2. Explicit and Hybrid Solution.** A more accurate but expensive approach to model the solution is to use explicit atoms. Ideally, one should include a sufficiently large number of atoms so that the properties (e.g., density) of the solution far from the surface converge to those of the bulk solution. However, as will be discussed in section 2.1.3, this often requires a rather large cell and long simulation times, which are difficult to afford with quantum-mechanical methods (e.g., DFT). To reduce the computational cost, one can develop a force field (FF), which is often less accurate than quantum-mechanical methods, to more efficiently describe the interatomic interactions in the solution. This molecular mechanical (MM) treatment can be used together with the quantum-mechanical (QM) treatment for different regions, forming the so-called QM-MM approach. To couple these two subsystems, it is common to use the electrostatic embedding approach,[22−24] which approximates the charge distribution at the MM level to determine a corrected QM energy that accounts for the electrostatic interaction between the two subsystems. Such an approach has been implemented into VASP.[22] Note that when there are atoms exchanging between these two subsystems, a dynamic coupling scheme[25] becomes necessary.

Chan et al.[26] compared the performance of explicit solvation and implicit solvation models. They considered various adsorbates (e.g., *CO, *CHO, *COH, *OCCHO, *OH, and *OOH) to Cu, Au, and Pt surfaces. For explicit solvation, they performed extensive AIMD simulations. For implicit solvation, they considered VASPsol and the SCCS model in Quantum ESPRESSO/Environ, which give nearly identical solvation energies. They found that these implicit solvation models do not provide more accurate energetics over simulations in vacuum. Moreover, the solvation energies of adsorbates are not transferable between metal surfaces.

To explicitly model electrolyte ions, the size of the simulation cell and the number of ions must be considered. The electrical double layer (EDL) is comprised of a compact Stern layer and a diffuse layer, both of which have ionic concentrations different from the bulk solution. To estimate the thickness of the EDL, the Debye length (which is determined by the ionic charge and concentration as well as the solvent dielectric constant) is commonly used. For 1 M aqueous NaCl solution at room temperature, the Debye length ($\lambda_D$) is ∼3 Å, which means that the potential exponentially decays to 36.8% of the surface potential at 3 Å from the surface. However, this is true only for low potentials. Moreover, 36.8% is still non-negligible, and the EDL thickness should depend on the surface charge as well. Saboorian-Jooybari et al. revisited this problem.[27] They showed an analytical solution to the PB equation for the planar surface

$$y(x_D) = 4\tanh^{-1}(\tanh(y_0/4)e^{-x_D})$$

where $y$ is the dimensionless potential $y = \frac{ze\phi}{k_BT}$ ($z$ is the ion charge and $\phi$ is the potential in physical units), $y_0$ is the dimensionless surface potential, and $x_D$ is the dimensionless distance to the surface $x_D = \frac{x}{\lambda_D}$. They further showed that the surface charge density is related to the surface potential as

$$y_0 = 2\sinh^{-1}(\sigma_D/2)$$

Here, $\sigma_D$ is the dimensionless surface charge density defined as

$$\sigma_D = \frac{\sigma}{\sqrt{2\rho^{\infty}\varepsilon_r\varepsilon_0 k_B T}}$$

where $\sigma$ is the surface charge density in physical units, $\rho^{\infty}$ is the bulk number concentration of electrolyte ions, $\varepsilon_r$ is the dielectric constant of the solution, and $\varepsilon_0$ is the dielectric permittivity of vacuum. Therefore, in order to reach $n$% of the surface potential, the distance should be

$$\delta_r = \lambda_d \ln\left(\frac{\tanh\left(\frac{\sinh^{-1}\frac{\sigma_D}{2}}{2}\right)}{\tanh\left(\frac{\sinh^{-1}\frac{\sigma_D}{2}}{200/n}\right)}\right) \quad (2)$$

To have a rough idea about the EDL thickness in a practical system, we consider the Pt(111) surface at 0 V vs SHE in 1 M NaCl aqueous solution. Using VASPsol, we obtain $\sigma$ = 1.25 e/nm$^2$. Then, using eq 2, we find that in order to reduce the potential to be 1% of the surface potential, the distance should be $4.48\lambda_D$ = 13.61 Å.

Regarding the number of ions, intuition suggests that it should be the bulk ionic concentration multiplied by the number of


https://doi.org/10.1021/acs.chemrev.3c00735
Chem. Rev. 2024, 124, 8620−8656

water molecules in the simulation cell plus the extra ions needed to balance the surface charge. However, the resulting concentration is too large. Schmit et al. derived a simple formula (SLTCAP method) to calculate the number of ions[28]

$$N_{\pm} = \nu_w \rho^{\infty} \exp\left(\mp \sinh^{-1}\left(\frac{Q}{2e\nu_w \rho^{\infty}}\right)\right) \quad (3)$$

where $\nu_w$ is the amount of solvent and $Q$ is the charge of the catalyst in the simulation cell. This formula makes the ionic strength in the cell the same as that in the bulk solution. Machado et al. further showed that this equation can be simplified to (SPLIT method)[29]

$$N_{\pm} \approx N_0 \mp \frac{Q}{2} \quad (4)$$

for $N_0 \gg Q$ (the difference between the SLTCAP and the SPLIT methods for $N_0 > 2Q$ is less than 1%). Using the SPLIT method, we estimate that to simulate a 1 M NaCl aqueous solution, if the surface charge amounts to 2e per cell and if there are 56 × 5 = 280 water molecules in the cell, then one needs to include 6 Na and 4 Cl.

Given the large size estimated above, many papers take a simplified approach that puts the explicit ions on a plane near the solid surface (Figure 2a) which represents the Helmholtz plane

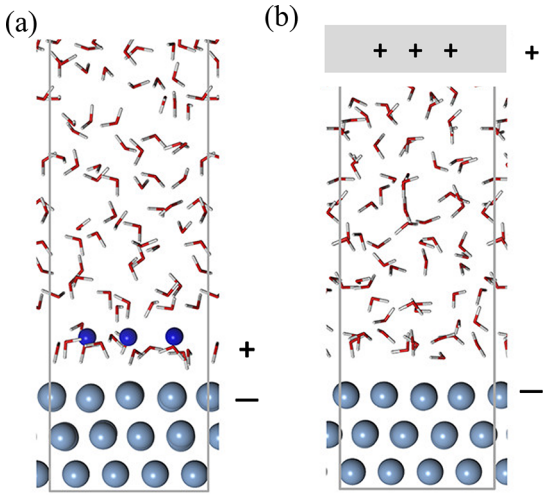


**Figure 2.** Explicit (a) vs implicit (b) electrolyte ions. Adapted with permission from ref 30. Copyright 2021 American Chemical Society.

(HP). The concentration of ions determines the surface charge density (due to the charge balance) and the Fermi level of the cell. Since the number of ions must be an integer, the surface charge and Fermi level are restricted to a small, discrete set of values that may not match the value of interest. This problem can be addressed by using a hybrid solvation model, as discussed below. It is also worth noting that [t91]he presence of electrolyte ions sharply increases the required simulation time to achieve equilibrium, thereby making calculations sensitive to the initial geometry and sampling the solvation structures substantially more difficult.

Similar to the QM-MM approach, implicit and explicit treatments of the solution can also be combined together to balance accuracy and efficiency. For example, the solution region close to the substrate (which requires higher accuracy) can be modeled explicitly, while the bulk solvent can be treated implicitly. By treating the electrolyte ions implicitly and solvent explicitly (Figure 2b), the ion concentration and surface charge (as well as the electrode potential) can be continuously tuned and the atomistic detail of the reaction directly involving solvent molecules can be accurately described. However, unlike the physical system where the ions are immersed into the solvent, this approach separates the ions from the explicit solvent region. Consequently, varying the thickness of the explicit solvent layer will lead to different average distances between the ions and the surface, resulting in different capacitances. Therefore, for a given electrode potential, the surface charge will artificially depend on the thickness of solvent in the model, resulting in different reaction energetics.[31] Finally, we note that the performance of different solvation methods has been evaluated for various systems.[26,32−34]

**2.1.3. Sufficient Sampling.** For explicit modeling, although it is convenient to represent the water as a static ice-like bilayer, the large ensemble of relevant states is often overlooked.[35] This begs the question: how can one sufficiently sample these states? This question further breaks down to (1) how many atoms should be used, and (2) how long the simulation time should be when using molecular dynamics for sampling (which is common). Behler et al.[36] systematically studied the convergence of the Cu(111)−water interface with respect to the water film thickness and the surface cell size. Their systems have water sandwiched between Cu slabs without a vacuum layer. They performed 1 ns NPT MD simulations for equilibration followed by 1 ns NVT simulations for production. They found that in order to have a "bulk water" region where the oxygen density vs distance to the surface is flat and has the same value as bulk water, the water film needs to be ≥30 Å and the surface size must be ≥(6 × 6) units. The radial distribution function of O−O is more sensitive to the system size, which converges at 40 Å water thickness and (8 × 8) surface size. They also analyzed the lifetimes of hydrogen bonds and water molecules residing at the surface, which shows that a 15 Å thick water region or a (3 × 3) surface is too small to reach convergency.

Chan et al.[26] studied simulation size effects for Au(111)−water and Pt(111)−water interfaces. Their systems had a vacuum layer between periodic images along the surface normal (i.e., including the water−vacuum interface). They considered a $(3 \times 2\sqrt{3})$ rectangular surface cell and two water thicknesses: 3 water layers (24 molecules) and 6 layers (48 molecules). They ran DFT-based AIMD simulations for >30 ps with 4 runs for each system. They found that, as shown in shown in Figure 3a−d, for Au(111), a 3 layer thick water is too thin to reach the experimental bulk water density, whereas 6 layers is sufficient (although the density oscillates strongly with respect to the distance to the surface, which is different from Behler et al.'s work[36] where the density profile is flat). Note that some quantities do not exhibit large changes when increasing the water thickness, such as the work function and the number of hydrogen bonds to *OH on the surface. For Pt(111), they found that 3 layer thick water is enough for convergency. It is also worth noting that the standard deviation of the solvation energy for the 4 runs ranges from 0.03 to 0.12 eV depending on the adsorbate and the surface.

Groß et al. studied the effects of surface cell size for the Pt(111)−water interface.[35,37,38] They considered 6 water layers on (3 × 3) and (6 × 6) surfaces (36 water molecules for (3 × 3) and 144 molecules for (6 × 6), respectively). They ran AIMD simulations for 40 ps for equilibration and another 40 ps for production. The oxygen atomic density profiles of these


https://doi.org/10.1021/acs.chemrev.3c00735
Chem. Rev. 2024, 124, 8620−8656

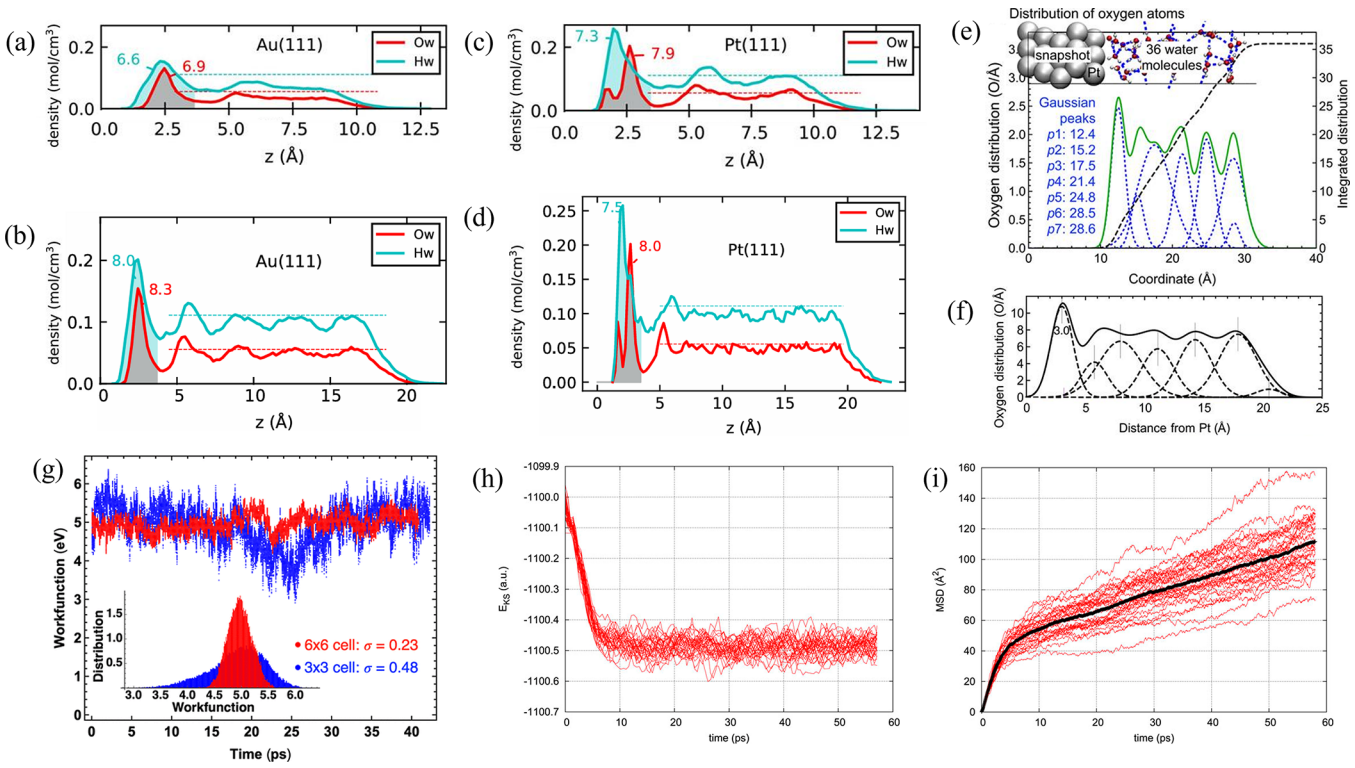


**Figure 3.** (a–d) Planar-averaged atomic densities of oxygen and hydrogen in explicit water over (a and b) Au(111) and (c and d) Pt(111) with (a and c) 3 water layers and (b and d) 6 water layers. The surface is a $(3 \times 2\sqrt{3})$ rectangular cell. The experimental densities of bulk water are shown by dashed lines. (e and f) Density of oxygen in water over Pt(111) with a (e) $3 \times 3$ surface and a (f) $6 \times 6$ surface. The water thickness is 6 layers. (g) Distribution of the work function of a water film over Pt(111) with $3 \times 3$ and $6 \times 6$ surfaces. The water thickness is 6 layers. (h) Block-averaged Kohn–Sham energies of bulk water of 32 runs, and the (i) mean squared displacement of oxygen atoms. (a–d) Adapted with permission from ref 26. Copyright 2020 AIP Publishing. (e) Adapted with permission from ref 37. Copyright 2016 AIP Publishing. (f) Adapted with permission from ref 38. Copyright 2018 AIP Publishing. (g) Adapted with permission from ref 35. Copyright 2022 American Chemical Society. (h and i) Adapted with permission from ref 39. Copyright 2018 AIP Publishing under [CC BY 4.0] [https://creativecommons.org/licenses/by/4.0/].

simulations are displayed in Figure 3e and 3f. They found that the simulated water thickness was sufficient to reach the experimental bulk water density. The different surface cell sizes yielded different work functions: $5.01 \pm 0.48$ eV for the $(3 \times 3)$ cell and $4.96 \pm 0.23$ eV for the $(6 \times 6)$ cell (see Figure 3g). Note that the work functions along the AIMD trajectory varied over a range of ~2 and 1 eV in the smaller and larger unit cells, respectively. It is also worth noting that for the $(3 \times 3)$ cell, the work function and potential energy fluctuated with long periodicities ≈ 40 ps, whereas for the $(6 \times 6)$ cell, such long periodicities were not observed.

To address how long the MD simulation time should be, Gygi et al.[39] systematically analyzed the time evolution of bulk water. They considered 32 samples of 64 water molecules with random initial positions. They ran 58 ps AIMD simulations for each sample and tracked the Kohn–Sham energy, number of hydrogen bonds, pair correlation function, and diffusion coefficient. These quantities require different amounts of time to converge. Particularly, the Kohn–Sham energy (averaged over ~0.5 ps) converges after ~15 ps (see Figure 3h). The diffusion coefficient and average number of hydrogen bonds maintained high uncertainty despite the large number of samples. For example, the diffusion coefficient ranged from $0.9 \times 10^{-5}$ to $3.4 \times 10^{-5}$ cm$^2$/s across the 32 samples (see Figure 3i). This large variation is also confirmed by simulations using a classical force field (TIP4P/2005) with longer duration (1.4 ns).

The papers above focus on the sampling of water. For electrolyte ions, we discussed the general principles of choosing the cell size and the number of ions in section 2.1.2. However, comprehensive convergence tests are still lacking and needed.

## 2.2. Electrode Potential

In the field of computational heterogeneous electrocatalysis, the electrode potential has historically been treated as a linear change to the electron energy.[43] This is a simplification of the actual role of the electrode, which adjusts the Fermi level of the catalyst–liquid system through electron transfer. To fully account for this role, the Fermi level must be modified in the simulation cell.

**2.2.1. Potential Reference Method.** A common approach is to add/remove electrons into/from the cell.[44,45] To avoid energy divergence, these extra electronic charges must be compensated, which can be achieved by introducing implicit electrolyte ions (Figure 2b). Alternatively, one can introduce explicit electron-donating/withdrawing species to change the $E_F$ (Figure 2a). For example, when alkali metal atoms are added into water, they often spontaneously lose electrons to the catalyst, thereby increasing the Fermi level. The latter approach is closer to reality, as counter charges are described by explicit ions. However, it is computationally expensive and only allows for discrete changes in the Fermi level. The former approach is less expensive and enables continuous tuning of the Fermi level.

To determine whether the Fermi level $E_F$ of the simulation cell ($E_F^{Cell}$) has reached the targeted value, we need to compare it with that of a reference electrode ($E_F^{ref}$), which is typically the standard hydrogen electrode (SHE). The most common


https://doi.org/10.1021/acs.chemrev.3c00735
Chem. Rev. 2024, 124, 8620–8656

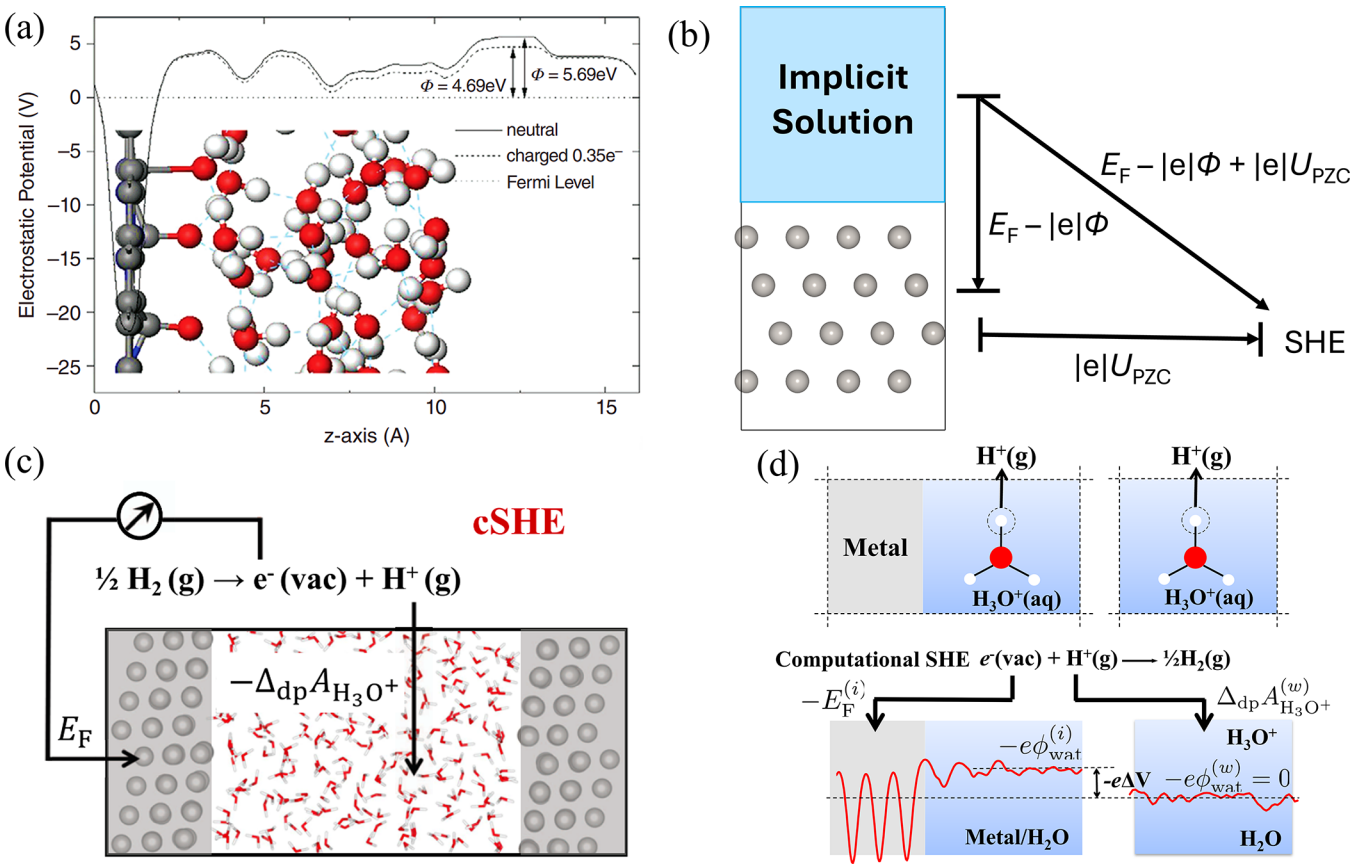


**Figure 4.** Methods for determining the Fermi level vs SHE. (a and b) Potential reference method. In (a), a vacuum is used as the reference, while in (b) an implicit solution is used as the reference. (c) The computational standard hydrogen electrode (cSHE) method and (d) the "two-reference" scheme for determining the deprotonation energy at the interface. (a) Adapted with permission from ref 40. Copyright 2011 Science Direct. (c) Adapted with permission from ref 41. Copyright 2022 AIP Publishing. (d) Adapted with permission from ref 42. Copyright 2017 American Physical Society.

method is to include a region with constant potential in the simulation cell and use it as an intermediate reference[38,40,46]

$$E_F^{Cell} - E_F^{Ref} = (E_F^{Cell} - |e|\Phi) - (E_F^{Ref} - |e|\Phi) \quad (5)$$

where Φ is the electrostatic potential in the reference region. We call this method the "potential reference" (PR) method. $E_F^{Cell} - e\Phi$ can be readily determined from the simulation cell once the reference region is specified. The difficulty is determining $E_F^{ref} - e\Phi$ (since the method changes with the reference region chosen) as detailed below.

If the simulation cell contains a vacuum then one can use it as the reference region (Figure 4a) and take advantage of the fact that $E_F^{SHE} - e\Phi$ has been measured experimentally (which is generally accepted as −4.44 eV[47]). If the simulation cell does not have a vacuum but has an implicit solution, then one can use the implicit solution as the reference region. In this case, an additional reference can be introduced to determine $E_F^{SHE} - e\Phi$. Specifically, one can choose a metal surface whose potential of zero charge (PZC) vs SHE ($U_{PZC}$) has been experimentally measured, put it into contact with the implicit solution, and then calculate the corresponding $E_F - e\Phi$. $E_F - e\Phi$ represents the energy change to take an electron from the implicit solution to that metal, and $|e|U_{PZC}$ represents the work to take the electron from that metal to the SHE. Therefore, the energy change to take the electron from the solution to the SHE, i.e., $E_F^{SHE} - e\Phi$, should be (as depicted in Figure 4b)

$$E_F^{SHE} - e\Phi = E_F - e\Phi + eU_{PZC} \quad (6)$$

Note that different metal surfaces can give different $E_F - e\Phi$, resulting in different $E_F^{SHE} - e\Phi$. In practice, one can consider multiple metal surfaces and take the average value. $E_F^{SHE} - e\Phi$ also varies with the solvation model and the quantum-mechanical method employed. For the VASPsol solvation model and PBE functional, the average $E_F^{SHE} - e\Phi$ derived from multiple metal surfaces is determined to be −4.6 eV.[4]

If the simulation cell does not have a vacuum or an implicit solution but instead has explicit solution, then it can be used as the reference region. Similar to the case of an implicit solution where the metal with known $U_{PZC}$ is introduced as an additional reference to determine $E_F^{SHE} - e\Phi$, here one can use a vacuum.[32] Specifically, we can take out the explicit solution from the simulation cell, put it into contact with a vacuum, and calculate Φ with respect to a vacuum. Then, using the experimental value of the SHE work function, we obtain the $E_F^{SHE} - e\Phi$ for the system with explicit solution.

**2.2.2. Computational Standard Hydrogen Electrode Method.** In addition to the PR approach, one can directly mimic a reference electrode in the calculation. The computational SHE (cSHE) method developed by Cheng and Sprik is a key example of this approach, which is represented in Figure 4c.[48−51] The overall equation for the electrode potential calculation can be written as

$$-eU_{SHE} = E_F^{(i)} - \Delta_{dp}A^{(i)}_{H_3O^+} + \Delta_f G^{g,o}_{H^+} + \Delta E_{ZP} \quad (7)$$



https://doi.org/10.1021/acs.chemrev.3c00735
Chem. Rev. 2024, 124, 8620−8656

where $E_F^{(i)}$ and $\Delta_{dp}A^{(i)}_{H_3O^+}$ denote the Fermi level of the interface and the deprotonation energy of a hydronium ion at the interface. $\Delta_f G^{g,o}_{H^+}$ is the formation energy of a gas-phase proton, and $\Delta E_{ZP}$ is the zero-point energy correction of an O−H bond. Both are constants with values of 15.81 and 0.35 eV, respectively.[52,53] Note that $\Delta_{dp}A^{(i)}_{H_3O^+}$ has no physical meaning due to the artificial Hartree potential shift (HPS) introduced under the periodic boundary condition (PBC). The HPS can be canceled out by coupling the deprotonation energy with the computed Fermi level in the same interface model. Note that the SHE is not suitable for nonaqueous electrochemical cells due to the unknown potential shift caused by the liquid−liquid junction between the reference electrode and the electrolyte. In such cases, reference electrodes like Ag/AgCl and Li metal are preferred. Computational versions of the Ag/AgCl and Li metal electrodes[54,55] have been developed recently, which involve computing the solvation energy of $Cl^-$ and $Li^+$ ions and embedding them into a thermodynamic cycle.

The difficulty of the cSHE method is accurately computing the solvation free energy of a proton in bulk water, which can be resolved with a free energy perturbation-based thermodynamic integration (FEP-TI) scheme. Currently, the use of an AIMD-assisted FEP-TI scheme for calculating the ion solvation energy is computationally demanding, especially when applied to large solid/liquid interface models. To reduce computational costs and expand the use of the "reference electrode" method, Le et al. recently proposed a "two-reference" scheme,[42] where the electrostatic potential of bulk water is used as a secondary reference in addition to the cSHE, as shown in Figure 4d. The key idea of this new approach is coupling the interface model (i) with a pure water model (w). This replaces the need to calculate $\Delta_{dp}A^{(i)}_{H_3O^+}$ in the large interface model with a simpler calculation in a small bulk water model to obtain $\Delta_{dp}A^{(w)}_{H_3O^+}$. The simulation cells in the interface and bulk water models are chemically distinct with separate HPS, thereby having differences in $\Delta_{dp}A_{H_3O^+}$. The HPS difference embedded in $\Delta_{dp}A_{H_3O^+}$ is exactly equal to the HPS-induced difference in the electrostatic potential $\phi_{wat}$ between the models. As such, the electrode potential can be calculated as

$$-eU_{SHE} = E_F^{(i)} - \Delta_{dp}A^{(w)}_{H_3O^+} + e_0\phi^{(i)}_{wat} + \Delta_f G^{g,o}_{H^+} + \Delta E_{ZP} \tag{8}$$

where $\phi^{(i)}_{wat}$ is the averaged electrostatic potential of the bulk water region in the interface model.

After knowing how to adjust the $E_F$ in the simulation cell and how to reference it to the SHE, the final question is what target value should be for a given electrode potential. Intuitively, one would expect it should be equal to that of the electrode, i.e., if the electrode potential is $U$ vs SHE then the Fermi level of the simulation cell should be $-|e|U$ vs SHE. Although this is largely true, the statistics of the grand canonical ensemble is overlooked, which leads to a fluctuating Fermi level for finite systems. This will be discussed in detail in section 2.3.3.

## 2.3. Reaction Energetics

Methods for calculating the energetics of reactions and other processes have been well established for thermochemistry. These methods are largely applicable to heterogeneous electrochemistry with the caveat that one must consider the condition of constant electrode potential ($U_{ext}$, where "ext" denotes the electrode is external to the catalyst−liquid system). However, many studies opt for conventional constant-charge methods to reduce computational complexity. While these approaches are valid when the total system charge remains constant, they are not well suited for modeling many processes in heterogeneous electrocatalysis, where the system often exchanges electrons with the electrode. Thus, techniques that address the $U_{ext}$ are necessary to accurately assess the performance of electrocatalysts. Additionally, pH plays an important role in electrocatalysis. Its effects are typically included in postprocessing as a linear correction term, but may be more significant and complex than this treatment suggests. It is therefore worth reviewing more advanced methods to capture these complexities.

**2.3.1. Thermodynamics.** To calculate electrochemical reaction thermodynamics, the computational hydrogen electrode (CHE) model popularized by Nørskov et al.[43] is widely used to study reactions that formally involve one proton and one electron. To illustrate this approach, consider the Volmer step as an example.[2] In this step, a proton in the aqueous solution is adsorbed onto the catalyst surface coupled with electron transfer. The reaction equation can be nominally written as

$$* + H^+ + e \rightarrow {}^*H \tag{9}$$

where * represents an active site on the catalyst. The thermodynamics of the Volmer step can be calculated as

$$\Delta G = G(^*H) - G(^*) - G(H^+_{aq}) - \mu_e(U_{SHE}) \tag{10}$$

where $G(H^+_{aq})$ is the energy of a proton in aqueous solution and $\mu_e(U_{SHE})$ is the energy of an electron at potential $U_{ext}$ vs SHE. These two terms are given by the following equations

$$G(H^+_{aq}) = G(H^+_{aq}(pH = 0)) - 0.059pH \tag{11}$$

$$\mu_e(U_{SHE}) = \mu_e(0_{SHE}) - |e|U_{SHE} \tag{12}$$

where $G(H^+_{aq}(pH = 0))$ is the energy of a proton in aqueous solution with pH = 0 and $\mu_e(0_{SHE})$ is the energy of an electron at 0 V vs SHE. Inserting eqs 11 and 12 into eq 10, one obtains

$$\Delta G = G(^*H) - G(^*) - G(H^+_{aq}(pH = 0)) - \mu_e(0_{SHE}) + 0.059pH + |e|U_{SHE} \tag{13}$$

It is challenging to directly evaluate $G(H^+_{aq}(pH = 0))$ and $\mu_e(0_{SHE})$ from first principles. Instead, the CHE model makes use of the SHE equilibrium to replace the electron and proton components with the free energy of hydrogen gas, i.e.

$$G(H_2)/2 = G(H^+_{aq}(pH = 0)) + \mu_e(0_{SHE}) \tag{14}$$

Inserting eq 14 into eq 13, one obtains

$$\Delta G = G(^*H) - G(^*) - G(H_{2(g)})/2 + 0.059pH + |e|U_{SHE} \tag{15}$$

where $G(^*H)$, $G(^*)$, and $G(H_{2(g)})$ all can be computed from first principles. Separation of the pH and the electrode potential has been termed the "Generalized CHE".[56]

A key issue with the CHE model is that it neglects the surface charge. Due to the application of $U_{ext}$, * and *H likely have different, nonzero net electronic charges. Therefore, a more accurate expression of eq 9 is

$$^*(Q1) + H^+ + (Q2 - Q1 + 1)e \rightarrow {}^*H(Q2) \tag{16}$$


https://doi.org/10.1021/acs.chemrev.3c00735
Chem. Rev. 2024, 124, 8620−8656

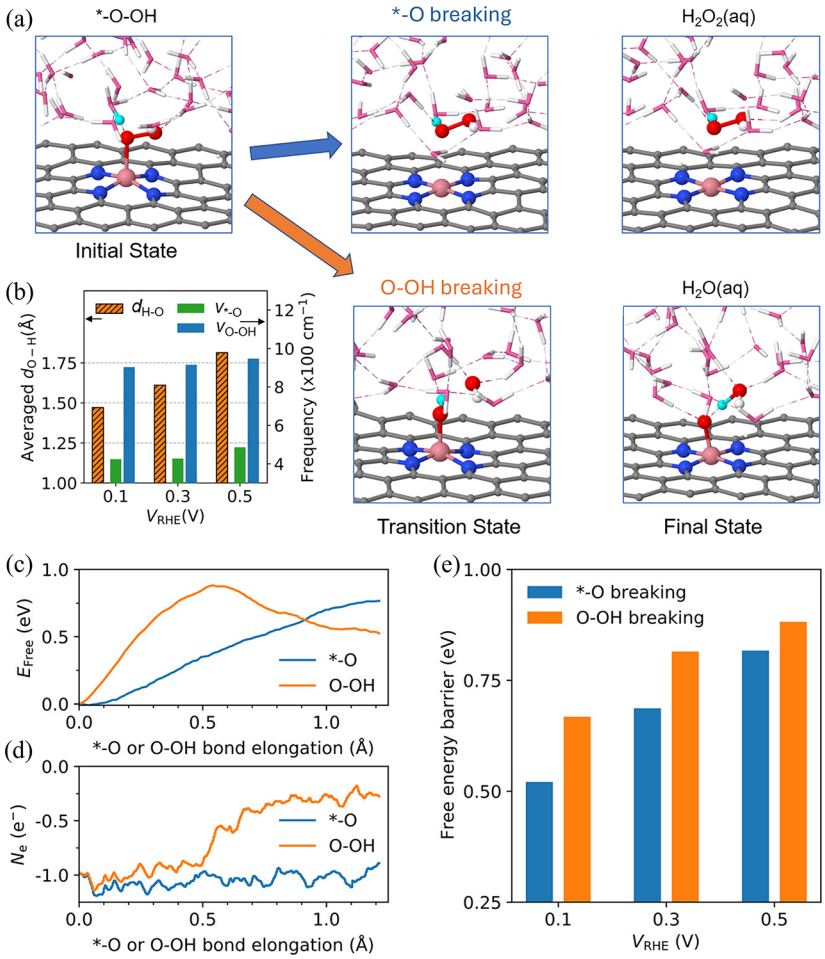


**Figure 5.** (a) Atomic structure evolution along two pathways of the ORR. (b) Bond length and frequency vs electrode potential. (c) Free energy profile for breaking a *−O bond and O−OH bond, and (d) corresponding electron number evolution. (e) Free energy barrier vs electrode potential. Adapted with permission from ref 61. Copyright 2021 American Chemical Society.

where Q1 and Q2 are the extra electronic charges of the catalyst before and after the reaction, respectively. Therefore, instead of calculating the energetics of charge-neutral catalysts, one should calculate the free energies for charged catalysts ($G(^*(Q1))$, $G(^*H(Q2))$) and include the energy contribution by the charge change ((Q2 − Q1 + 1)e). Accordingly, the thermodynamics under constant potential is calculated as

$$\Delta G = G(^*H(Q2)) - G(^*(Q1)) - G(H_{2(g)})/2 + 0.059pH + |e|U_{SHE} - (Q1 - Q2)\mu_e \quad (17)$$

Note that the surface charge not only induces an electric field that interacts with the adsorbate (electrostatic effect) but can also change the electronic state occupation of the catalyst, which may significantly affect the binding strength of the adsorbate (chemical effect).[57]

Many studies using the CHE model do not consider explicit solvation. This may result in significant errors, especially when the reaction species interact strongly with the solution (e.g., through hydrogen bonds), as such interactions change during the reaction (and thus cannot be canceled out). The explicit solvation methods discussed in section 2.1 are useful for addressing this issue.

After calculating the thermodynamics for each elementary step along the reaction path, the thermodynamically limiting step can be identified. The catalyst with a less uphill (or more downhill) thermodynamic limiting step is often considered to be more active. However, this approach assumes that the thermodynamics of each reaction step is strongly correlated with the activation energy, which is often not true.[58−61] Therefore, it is important to directly calculate the kinetics, especially the activation energy of each elementary step, to better understand and evaluate catalysts.

**2.3.2. Kinetics.** Static approaches such as the nudged elastic band method (NEB)[62] have been commonly used to calculate activation energies. These approaches often assume certain structures for the initial and final states and thus overlook the dynamic structures of the liquid. They also oversimplify entropic effects that are due to thermal fluctuations. Dynamic approaches are more accurate at increased computational cost due to better sampling of the phase space. These methods employ constrained or biased molecular dynamics. For example, slow-growth marginally increments the reaction coordinate ($\xi$) at each MD step.[63,64] Blue-moon sampling runs separate MD simulations at different fixed $\xi$ values, where the free energy profile is constructed via thermodynamic integration.[65] Additional $\xi$ values can be included afterward if the reaction profile is determined to be insufficiently sampled. Umbrella sampling is similar to blue-moon sampling but employs potential biases (usually harmonic) along the $\xi$ rather than strictly fixing the coordinates.[66] In this manner, adjacent images can overlap in structure to potentially discover more favorable reaction


https://doi.org/10.1021/acs.chemrev.3c00735
Chem. Rev. 2024, 124, 8620−8656

pathways. Metadynamics similarly introduces artificial biases, but is instead a single calculation with a time-dependent potential that accumulates Gaussian penalties to the energy for nearby structures around each MD step.[67] These biases cause the simulation to eventually escape local minima and subsequently find another minimum. Once the full biased profile converges to be roughly uniform, the real profile can be extracted by removing the biases in processing. It is worth noting that commonly used thermostats (e.g., Nosé−Hoover) may give an uneven temperature distribution in heterogeneous systems, known as the "flying ice cube" effect. This problem can be solved using Langevin dynamics.[68]

Given the computational cost needed for extensive sampling, one may ask if it is necessary and if the electrolyte could remain frozen and unequilibrated throughout each elementary step. To answer this question, Melander analyzed the relevant time scales:[1] the time for reaction, for motion of electrolyte species, and for electron transport in catalysts. They concluded that for reactions with barriers higher than 0.2−0.3 eV, the water and solvated ions should be treated as being completely mobile. For metal catalysts, electron transport is much faster than any relevant reaction, justifying the grand canonical treatment of the electrons. For semiconductors, the electrons are estimated to move at least as fast as the electrolyte ions. Therefore, the grand canonical ensemble should also be used for reactions with barriers > 0.2−0.3 eV. Note that when calculating subsequent steps, the final state of the first step may not match the initial state of the second step.[69] For example, when studying the Volmer−Heyrovsky pathway of the HER in pH-neutral/alkaline media, the final state of the simulated Volmer step ($H_2O + e + * \rightarrow *H + OH^-_{int}$) has $OH^-$ near the interface, while the initial state of the simulated Heyrovsky step does not have $OH^-$ ($H_2O + e + *H \rightarrow H_2 + OH^-_{int}$), as illustrated in Figure 5a. The gap between these two states is the diffusion of $OH^-$ from the interface region to the bulk solution ($OH^-_{int} \rightarrow OH^-_{bulk}$). This process can alternatively be treated as transferring a proton from bulk solution to $OH^-_{int}$ to form $H_2O$, i.e., $OH^-_{int} + H_2O_{bulk} \rightarrow H_2O_{int} + OH^-_{bulk}$. The thermodynamics of this step can be calculated as follows

$$\Delta G = G(OH^-_{bulk}) + G(H_2O_{int}) - G(H_2O_{bulk}) - G(OH^-_{int})$$

where $G(OH^-_{int})$ and $G(H_2O_{int})$ are the energies of the interface systems with $OH^-$ and the converted $H_2O$. This equation can be simplified by observing that $G(H_2O_{bulk}) - G(OH^-_{bulk}) = G(H^+_{bulk})$

$$\Delta G = G(H_2O_{int}) - G(OH^-_{int}) - G(H^+_{bulk})$$

By implementing eq 11 (as $H^+_{bulk} = H^+_{aq}$), the equation can be further reduced

$$\Delta G = G(H_2O_{int}) - G(OH^-_{int}) - G(H^+_{aq}(pH = 0)) + 0.059pH$$

Using the SHE equilibrium shown in eq 14, the proton energy can be related to the energy of hydrogen gas. Thus

$$\Delta G = G(H_2O_{int}) - G(OH^-_{int}) - G(H_{2(g)})/2 + 0.059pH + \mu_e(0_{SHE}) \quad (18)$$

where $G(H_2O_{int})$, $G(OH^-_{int})$, and $G(H_{2(g)})/2$ can be readily determined from DFT calculations. $\mu_e(0_{SHE})$ is known experimentally.

Some electrochemical reactions involve electron transfer to outer-sphere species. To calculate the energetics of such processes, one can use Marcus theory with parameters calculated from first principles. These calculations typically involve the combination of constrained DFT and MD simulation. An example was shown recently by Melander et al., who studied the charging of $CO_2$ during $CO_2R$.[70]

**2.3.3. Constant Potential.** As mentioned previously, processes at electrochemical interfaces often occur under a constant electrode potential ($U_{ext}$) rather than a constant charge. The most direct approach for simulating a constant potential is to tune the electron number ($n_e$) so that the Fermi level ($E_F$) of the simulation cell equals that of the electrode (i.e., $-|e|U_{ext}$)[44,45] and balance the excess electronic charges with implicit ionic charges in the solution. Determining the electron number for a given $U_{ext}$ is essentially a root-finding problem, and various algorithms (e.g., bisection, Newton, Secant) can be used to solve it. Note that when comparing the energy of systems with different $n_e$, one must account for this difference by using the grand potential (also called Landau free energy)[71]

$$\Phi_G = A + E_F n_e \quad (19)$$

where $A$ is the Helmholtz free energy of the system.

This approach overlooks the statistics of electrons. In reality, although the $E_F$ of the electrode is a constant, the $E_F$ of the system is not; instead, it should thermally fluctuate around the electrode's $E_F$. To describe this, Otani et al. developed sets of dynamic equations for AIMD that treat the electrons using a grand canonical ensemble.[72] In the simplest case where the potentiostat is not directly coupled to a thermostat, the electron number is governed by the equation

$$U_{int} - U_{ext} = m_{n_e}\frac{d^2 n_e}{dt^2} \quad (20)$$

where $m_{n_e}$ is a fictitious mass describing the coupling strength between the system and the electrode and $U_{int}$ is the "internal potential" of the system defined as $-E_F/|e|$. The potentiostat can also be directly coupled to either the thermostat for the atoms or a separate thermostat with a different temperature to shorten the required equilibration time.

Wippermann et al. introduced an approach to sample the canonical ensemble at constant temperature and applied electric potential.[73] This approach requires the presence of two "electrodes": one can represent the solid of interest, and the other balances the excess electronic charges on the first electrode and can be realized by a plane of doped Ne atoms[74] in DFT simulation. The electron number under this thermopotentiostat is integrated over a finite time step through the following equation

$$n(t + \Delta t) = n(t) - C_0[U(t) - \Delta U_0](1 - e^{-\Delta t/\tau_\Phi}) + N\sqrt{k_B T C_0(1 - e^{-2\Delta t/\tau_\Phi})} \quad (21)$$

where $\Delta t$ is the MD time step, $C_0$ is the capacitance of the bare electrodes in a vacuum without any dielectric, $\Delta U_0$ is the potential difference between the electrodes set externally, $\tau_\Phi = RC_0$ is the relaxation time constant for the potentiostat, and $N$ is a Gaussian random number that follows $\langle N\rangle = 0$ and $\langle N^2\rangle = 1$. In this fashion, the thermopotentiostat couples the change in


https://doi.org/10.1021/acs.chemrev.3c00735
Chem. Rev. 2024, 124, 8620−8656

potential with thermal fluctuations so that the total change is zero on average.

Liu et al. have implemented various constant-potential algorithms directly into VASP (CP-VASP).[45,61,75] Similar implementations have also been made recently.[7,76] Using CP-VASP, Liu et al. have elucidated the mechanisms of various reactions and catalysts.[45,61] For example, they studied the kinetics of the ORR on Co−N−C by performing constant-potential AIMD simulation. They used the "potential reference" method to determine the $E_F$ vs SHE and tuned the electron number every few steps of slow-growth simulation to match the $E_F$ with the $-|e|U_{ext}$. The counter charges are described by the VASPsol solvation model, and a thin water film is included for explicit solvation. They studied why Co−N−C catalysts can produce $H_2O_2$ through oxygen reduction despite this product being highly thermodynamically unfavorable compared with $H_2O$ formation.[61] Specifically, they calculated the free energy profile for breaking the *−O bond of *OOH (to form $H_2O_2$) and breaking the O−OH bond (to form $H_2O$) to determine the selectivity of $H_2O_2$ vs $H_2O$. Figure 5a shows the structure evolution and Figure 5c shows the free energy profile for these competing steps. Indeed, at the "final" state, breaking the O−OH bond to form $H_2O$ has a lower energy than breaking the *−O bond to form $H_2O_2$, consistent with the thermodynamics. However, $H_2O_2$ has a lower activation energy of formation than $H_2O$, explaining the selectivity preference for $H_2O_2$. Notably, the evolution of the electron number is significantly different during $H_2O$ and $H_2O_2$ formation: in the former case, the system gains ∼1 electron, while in the latter case, the electron number remains nearly constant, as depicted in Figure 5d. These features cannot be captured by conventional constant-charge methods. Moreover, their calculations show that the difference in their activation energies increases as $U_{ext}$ decreases, which is shown in Figure 5e. This trend indicates an increased selectivity for $H_2O_2$ as the potential decreases, which coincides with experimental observations.[77] The enhanced selectivity can be explained by the coupled effects of surface charge and explicit solvation; as $U_{ext}$ decreases, the catalyst surface carries more negative charges, which are then partially transferred to the O bonded to the metal atom. This enhances the hydrogen bonding between O and nearby $H_2O$. Consequently, the H in $H_2O$ is more easily stripped by *OOH, thereby making the formation of $H_2O_2$ more facile.

As another example, Peterson et al.[78] used the SJM to demonstrate that the use of a constant potential method significantly influences the reaction profile of the Volmer step. They calculated the activation barriers through "dyNEB".[79] The solvent environment was modeled explicitly as a single ice layer. The transferred proton was constrained to a one-dimensional coordinate, while all other atoms were geometrically fixed. As the energy depends on the charge transfer as shown in eq 19, intermediate states closer to the final state will be more strongly affected by the potential than intermediates near the initial state. Thus, the reaction coordinate of the transition state decreases as the applied potential decreases. This behavior also explains the nonlinear relationship between the reaction energetics and the electrode potential over large potential windows. Constant-potential approaches are becoming increasingly popular for studying heterogeneous electrochemistry.[80−82]

We note that although the terms "constant potential" and "grand canonical ensemble" have been used almost interchangeably in the literature, they have subtle differences. The grand canonical ensemble describes an ensemble of electrons under constant electrode potential, volume, and temperature. Due to the finite temperature, the Fermi level and the number of electrons will thermally fluctuate, even with a fixed atomic structure. Therefore, calculations that do not consider this thermal fluctuation (e.g., structure relaxation) should preferably not be labeled grand canonical ensemble calculations; instead, they can be referred to as constant-potential calculations.

Constant-potential energetics can be derived from constant-charge calculations, which are generally easier to perform.[71,83−95] The most commonly used method is based on the second-order Taylor expansion of the energy series with respect to the charge $q$

$$E \approx E_0 + q\left.\frac{\partial E}{\partial q}\right|_{q=0} + \frac{1}{2}q^2\left.\frac{\partial^2 E}{\partial q^2}\right|_{q=0} \tag{22}$$

where $E_0$ is the charge-neutral energy, the first derivative is the electrode potential with no surface charge ($\Phi_0$), and the second derivative is the inverse of the capacitance $C$. This energy expression can be reorganized to be

$$E = E_0 + C(\Phi - \Phi_0)\Phi_0 + \frac{C(\Phi - \Phi_0)^2}{2} \tag{23}$$

where the capacitance can be obtained by calculating the potentials with different electron numbers.[71] For a given reaction, one can use this approach to correct the energy of each species and obtain the reaction energetics. As a further simplification, one can use the change in the charge partitioned to the catalyst (plus adsorbate, if applicable) and the change in Fermi level between the final state and the initial state to approximate the capacitance and thus correct the energy of the final state to the same potential as the initial state. This approach is called the "charge extrapolation" method.[90]

Very recently, Beinlich et al. used a capacitor to map constant-charge free energy landscapes to the constant-potential regime.[83] They observed that the canonical potential energy surface (PES) of constant-charge calculations contains the same information (the activation energies in particular) as the grand canonical PES of constant-potential calculations, which can be mapped to each other through a Legendre transformation. They described two approaches: either multiple NEB calculations can be performed and the activation energy corresponding to the desired potential can be interpolated from the data, or capacitor models can be employed to extrapolate the kinetic barrier from a single NEB calculation. These capacitor models include the single-capacitance (SC) approximation where the capacitance is constant, the electronic capacitance (EC) approximation which calculates the local capacitance for the states of interest (IS, TS, and FS), and the electronic and geometric capacitance (EGC) approximation that expands the canonical PES along the potential around a stationary point. Their models accurately recreate the activation energies of the Volmer step on Au(111) predicted by constant-potential calculations at reduced computational cost.

**2.3.4. pH Effects.** Electrolyte pH can have a strong impact on electrocatalysis.[96−98] As discussed previously, the pH effect is often included as a shift for the proton free energy in the CHE model according to the Nernst equation (0.059pH). However, there are important effects beyond this energy shift,[97] including the following. (1) Changes in the proton donor or acceptor, for example, from $H_3O^+$ to $H_2O$ when changing from acidic to alkaline conditions for proton-donating reactions. (2) Changes in the surface charge. For the same RHE potential, a higher pH


https://doi.org/10.1021/acs.chemrev.3c00735
Chem. Rev. 2024, 124, 8620−8656

will decrease the SHE potential, resulting in more negative or fewer positive surface charges. This will change the intrinsic reactivity of the surface[57] and/or the electric field in the EDL interacting with the adsorbate dipole.[99,100] (3) Reactions with $OH^-$ (with pH-dependent concentration) can occur in the solution without interaction from the electrode. For example, the yield of acetate from CO reduction at −0.75 V on Cu nanosheets increased by an order of magnitude as the pH increased.[101] The improved activity was attributed to ketene undergoing a solution-phase reaction with $OH^-$ ions.[102]

Effect 2 can be addressed by the tuning electron number as discussed above. For effects 1 and 3, it is necessary to include an explicit $H_3O^+$ or $OH^-$ molecule in the simulation.[61,103,104] However, the limited cell sizes accessible with DFT restrict simulations to extreme local pH values, which are often different from bulk pH values. To account for the bulk pH effect, one can consider 2 steps:[99,105] the diffusion of a proton from bulk solution to the interface region described by the simulation cell and the reaction in the simulation cell itself. The bulk pH will linearly change the thermodynamics of the first step following the CHE model. However, the bulk pH does not affect the energetics of the second step, which instead depends on the local pH. Therefore, by calculating the first step using the CHE model and the second step using the cell with explicit $H_3O^+$ or $OH^-$, one can obtain an energy diagram as exemplified for the Volmer step in acidic conditions ($H^+_{bulk} + e \rightarrow *H$) in Figure 6b, where

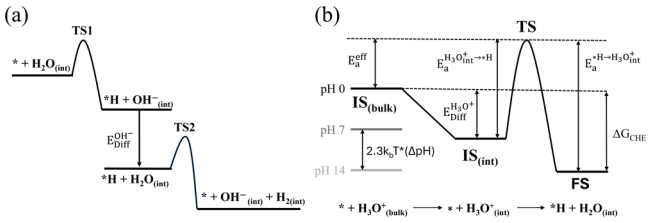


**Figure 6.** (a) To bridge the alkaline HER Volmer step and Heyrovsky step simulated separately using interface models, the diffusion of $OH^-$ away from the interface (achieved by $H^+$ diffusion from the bulk solution) needs to be considered. (b) Calculation of the bulk pH effect as exemplified by the Volmer reaction under acidic conditions. $IS_{(bulk)}$ is the initial state composed of the bare catalyst and $H_3O^+$ in bulk solution, $IS_{(int)}$ is the "initial state" after the proton has diffused to the interface (the catalyst is still bare), and FS is the final state where the catalyst has adsorbed H and no longer has $H_3O^+$ in the interface. The process of $IS_{(int)} \rightarrow TS \rightarrow FS_{(int)}$ is modeled directly, while the level of $IS_{(bulk)}$ is derived using the CHE method. Note that in both figures, the kinetic barriers for diffusion between the interface and the bulk solution are ignored.

the bulk pH effect is included. Note that the local pH determined by the simulation cell can affect the energetics, and it is therefore important to find a representative local pH. Also, this approach does not consider the energy barriers for proton diffusion from the bulk to the interface, which are assumed to be negligible.

## 2.4. Spectra

While several types of spectroscopies are widely used within the experimental electrocatalysis community,[106−112] the use of theoretical methods to predict spectra (i.e., computational spectroscopy) remains less common in the field. Interpretation of experimental spectroscopic data is often convoluted by solvent effects, polarization due to electric fields, changes due to the potential and the pH, the presence of counterions, and restructuring of the catalyst surface under reaction conditions. We believe these challenges, however, present an opportunity for the modeling community to provide complementary insights from well-designed atomistic simulations.[113] Recent advances within the machine learning community and the growing access to exascale computing may enable the development of integrated experiment−theory methods to characterize complex electrochemical interfaces.[109,114,115]

Although the discussion below is focused on X-ray absorption spectroscopy (XAS) and vibrational spectroscopies (e.g., infrared (IR) and Raman), we note that other techniques such as X-ray photoelectron spectroscopy (XPS), ultraviolet−visible (UV−vis) light spectroscopy, electron energy-loss spectroscopy (EELS), and nuclear magnetic resonance (NMR) also have significant application in electrocatalysis.[109,115,116]

**2.4.1. X-ray Absorption Spectroscopy.** *Overview.* XAS is a widely used element-specific technique for characterization of electrocatalysts. XAS can be applied ex situ as well as for operando and in situ experiments.[112] The recent review by Besley et al. provides an excellent primer on DFT methods for calculations of XAS spectra.[117] Also, the review by Timoshenko and Cuenya provides a valuable overview of applying XAS to characterize electrocatalysts.[112] In XAS, the strongly bound core electrons are excited to unoccupied electron states by absorption of a photon. Depending on the principal quantum number of the core electrons, XAS is divided into different edges, e.g., K, L, and M edges corresponding to the first, second, and third shell. Within the same edge, XAS is further differentiated by the total angular momentum, e.g., $L_1$, $L_2$, and $L_3$ edges corresponding to 2s, $2p_{1/2}$, and $2p_{3/2}$ core states (see Figure 7a and the exemplary

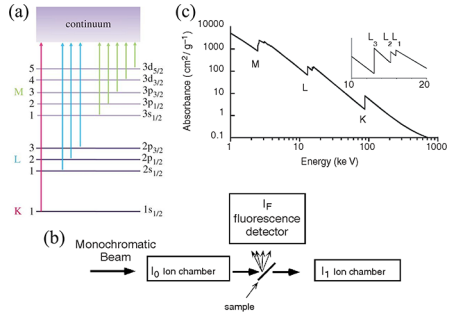


**Figure 7.** X-ray absorption spectroscopy. (a) The physical process of XAS. (b) The standard experimental setup for XAS measurement. (c) Exemplary XAS spectra of lead. (a) Adapted with permission from ref 119. Copyright 2013 The Royal Society. (b and c) Adapted with permission from ref 118. Copyright 2003 Science Direct.

XAS spectra of lead in Figure 7c). In an experiment setup, XAS is commonly measured in either the transmission mode or the fluorescence mode (see Figure 7b).[118] In the transmission mode, the X-ray flux is measured using ionization chambers in front of and behind the sample. In the fluorescence mode, X-rays are collected off the sample that are produced after the core−hole from the initial absorption is filled, which is particularly useful in electrocatalysis studies as it does not require thin samples. Since the edge position varies with the absorbing atom, XAS is an element-specific characterization technique. Furthermore, XAS is sensitive to the local chemical environment of the absorber atom, such as the charge state, coordination number, and local symmetry, making it a powerful local structural probe widely used in physics, chemistry, materials science, and biology.


https://doi.org/10.1021/acs.chemrev.3c00735
Chem. Rev. 2024, 124, 8620−8656

In XAS analysis, the spectrum is typically partitioned into two regions. The near-edge region comprises the spectrum up to ∼50 eV above the absorption edge, known as the X-ray absorption near-edge structure (XANES) region. The portion of the spectrum at higher energies is known as the extended X-ray absorption fine structure (EXAFS) region. In the EXAFS region, oscillations in the spectrum are observed relative to what would be expected for an isolated atom. These oscillations arise due to interference between the ejected photoelectron wave and the waves backscattered by neighboring atoms. Well-established procedures[120] exist for analyzing these interference patterns to extract structural information, such as the atomic distances, elemental identity, and coordination number of atoms around the absorbing atom. To extract accurate structural information, however, EXAFS requires high-fidelity data. This can be difficult to obtain under many experimental conditions, particularly in operando studies, and limits the temporal resolution of the technique. XANES offers several advantages in this respect. XANES is less sensitive to disorder effects and allows useful spectra to be collected much more quickly than EXAFS. XANES contains rich information associated with the electronic structure near the Fermi level, which can be used to deduce the charge state, coordination number, and local symmetry.[121] However, this information is convoluted and contains entangled contributions from several different physical origins. For this reason, quantitative XANES analysis is more challenging than that for EXAFS and often requires more intensive computational efforts.

*Computational Methods.* Computational modeling plays a key role in XAS spectral analysis. The cross section of XAS can be calculated from Fermi's golden rule

$$\sigma(\omega) \propto \omega \sum_{\mathrm{f}} |\langle \Psi_{\mathrm{f}}|\hat{O}|\Psi_0\rangle|^2 \delta(E_{\mathrm{f}} - E_0 - \omega) \tag{24}$$

where $E_0$ and $E_{\mathrm{f}}$ are the total energies of the initial ($|\Psi_0\rangle$) and final many-body states ($|\Psi_{\mathrm{f}}\rangle$). $\hat{O}$ is the transition operator, and its dipole and quadrupole contributions are given by $\hat{O} = \boldsymbol{e}\cdot\boldsymbol{r} + \mathrm{i}/2(\boldsymbol{e}\cdot\boldsymbol{r})(\boldsymbol{q}\cdot\boldsymbol{r})$, where $\boldsymbol{e}$, $\boldsymbol{q}$, and $\boldsymbol{r}$ are the polarization vector and the wave vector of the photon beam and the position operator of the electron.[122] In general, the dipole term is the dominant contribution to XAS. However, the quadrupole term can be important at the pre-edge region when the dipole transition is forbidden, such as the pre-edge of transition metal K-edge XAS in materials with inversion symmetry. To evaluate eq 24 in practice, one often needs to resort to the single-particle representation. Here, we briefly review several popular XAS simulation methods, including the multiple scattering method, linear response (LR) method, core−hole potential (CHP) method, and multiplet ligand-field theory.

**Multiple Scattering Method.** In the multiple scattering method, the spectral features in XAS arise from the quantum inference of the outgoing wave of the photoelectron with its scattering waves from neighboring atoms within the order of the mean free path. Therefore, the absorption coefficient can be calculated from the sum of the scattering magnitude along different scattering paths. These include not only the backscattering, i.e., reflection from neighboring atoms directly back to the absorber atom, but also multiple scattering paths, which involves three or more atoms.[123] Under the single-particle approximation, the many-body wave functions in eq 24 are replaced by their single-particle counterparts. The absorption coefficient is factorized into an atomic background absorption modulated by the X-ray absorption fine structure, $\chi(k)$, expressed as[117,123]

$$\chi(k) = S_0^2 \sum_R \frac{|f_{\mathrm{eff}}(k)|}{kR^2} \sin(2kR + \Phi_k) e^{-2R/\lambda_k} e^{-2\sigma^2 k^2} \tag{25}$$

where $f_{\mathrm{eff}}(k)$ is the effective scattering amplitude at the wave vector $k$ and $\Phi_k$ is the partial wave phase shift at the final state. $R$ and $\lambda_k$ are the interatomic distance and energy-dependent mean free path. The term $e^{-2\sigma^2 k^2}$ accounts for the Debye−Waller factor. The overall prefactor $S_0^2$ represents the many-body effect due to the relaxation of the system in the presence of the core−hole. The multiple scattering method has been routinely used for EXAFS analysis, while XANES analysis is more challenging as it requires summing the scattering path expansion to infinite order and relies on very accurate descriptions of the electronic structure.

**Linear Response Method.** Under the single-particle picture and the linear response framework, eq 24 can be evaluated based on the band structure from DFT

$$\sigma_{\mathrm{LR}}(\omega) \propto \omega \sum_S |\langle S|\hat{O}|0\rangle|^2 \delta(\Omega_s - \omega) \tag{26}$$

where $|0\rangle$ is the DFT ground state and $|S\rangle$ denotes the eigenstate of the electron−core hole Hamiltonian ($H_{\mathrm{eh}}$) with the excitation energy $\Omega_s$. $H_{\mathrm{eh}}$ is typically expressed in the electron−core hole basis. Within time-dependent density functional theory (TDDFT), the solution of $H_{\mathrm{eh}}^{\mathrm{TDDFT}}$ is obtained by solving the core excitation version of Casida's equation.[124] The results can depend on the choice of the exchange-correlation functional or the flavor of the hybrid functional under the generalized Kohn−Sham (KS) scheme.[125] $H_{\mathrm{eh}}$ can also be formulated using many-body perturbation theory under the GW-BSE scheme, where the KS orbital energy is corrected with the GW self-energy and $H_{\mathrm{eh}}^{\mathrm{BSE}}$ is constructed according to the Bethe−Salpeter equation (BSE).[126] $H_{\mathrm{eh}}^{\mathrm{BSE}}$ contains two coupling terms: the exchange interaction between electron−core hole pairs and the screened Coulomb interaction between the electron and the core−hole. The latter is crucial to treat excitations with strong exciton character. Because GW calculations are computationally very expensive, normally they are omitted in practical XAS simulations and $H_{\mathrm{eh}}^{\mathrm{BSE}}$ is solved on DFT orbitals and energy levels.

**Core−Hole Potential Method.** Another popular XAS simulation approach is the core−hole potential method. Intuitively, the presence of the core−hole is approximated by replacing the ionic potential of the absorber atom with the next element in the periodic table, i.e., the $Z + 1$ approximation. In a modern DFT core−hole potential code, the core−hole effect is treated by creating an explicit (full or partial) core−hole in all electron codes or a special core−hole pseudopotential in pseudopotential codes. The screening effects are captured by the relaxation of the valence electrons in the self-consistent field calculation, which yields the electronic states in the presence of typically either one-half (i.e., the transition state) or a full core−hole. At the final state, the core electron can be either placed at the bottom of the conduction band or removed from the system. We denote the single-particle core state of the ground state as $|\Psi_\alpha\rangle$ and the empty states in the core−hole potential calculation as $|\tilde{\Psi}_{\mathrm{f}}\rangle$ with their corresponding KS energy levels as $\varepsilon_\alpha$ and $\tilde{\varepsilon}_{\mathrm{f}}$. The absorption cross section can be expressed as

$$\sigma_{\mathrm{CHP}}(\omega) \propto \omega \sum_{\mathrm{f}} |\langle \tilde{\psi}_{\mathrm{f}}|\hat{O}|\psi_\alpha\rangle|^2 \delta(\tilde{\varepsilon}_{\mathrm{f}} - \varepsilon_\alpha - \omega) \tag{27}$$



https://doi.org/10.1021/acs.chemrev.3c00735
Chem. Rev. 2024, 124, 8620−8656

**Table 1. List of XAS Simulation Software**

| | linear response | | | |
|---|---|---|---|---|
| multiple scattering | TDDFT | BSE | core−hole potential | multiplet ligand field |
| FEFF,[135] FDMNES[136] | ORCA,[137] NWChem[138] | OCEAN,[139] exciting[140] | XSpectra,[141] VASP,[142] ShirleyXAS,[143] StoBe[144] | Quanty,[145] CTM4XAS,[146] EDRIXS[147] |

In periodic systems, the absorber atom is treated as a defect. The system needs to be modeled with a large enough supercell to avoid the spurious interactions between image cells.

There are multiple important differences between the linear response method and the core−hole potential method.[127] Below we discuss several of them.

(1) Screening potential: Under the linear response method, the screening potential is typically constructed under the random phase approximation, i.e., the dielectric response from an infinitesimal perturbation. Under the core−hole potential method, the screening results from electron relaxation with a finite core−hole.[127] This may lead to nontrivial differences between the two methods, especially in semiconductors and insulators. If the core electron is kept in the system at the bottom of the conduction band in the core−hole potential method, it can result in stronger screening than the linear response method.[127]

(2) Edge alignment: The position of the absorption edge is important to determine the chemical shift of the core level. The calculated absolute edge position is subject to the intrinsic Kohn−Sham DFT energy level error. In a pseudopotential calculation, the absolute edge position is not physically meaningful due to the use of the pseudopotential. Therefore, it is more important to obtain an accurate relative edge alignment from one material to another or from one absorption site to another. The absolute edge position can then be obtained by referencing to an experimental standard and applying a constant shift to all simulations. There are several methods to perform edge alignment in different codes, such as the ΔSCF method[128,129] and the correction based on the static screened Coulomb potential of the core−hole.[130] Another promising approach is to evaluate the quasiparticle energy of the core−hole under the GW approximation.[131]

(3) Pre-edge features: The core−hole potential method in its single-particle form has been shown to systematically underestimate the pre-edge intensity in O K-edge XAS, while the BSE method yields much better agreement with experiment. Recent progress on improving the pre-edge line shape using many-electron transition amplitudes within the core−hole potential method can be found in the work of Liang et al.[132]

To systematically understand the importance of the differences between each method, extensive multicode benchmark studies are needed.[127]

**Multiplet Ligand-Field Theory.** The single-particle picture of XAS works well for weakly correlated systems but breaks down when modeling strongly correlated excited states, such as transition metal 3d states or rare earth 4f states. The classic example is transition metal L-edge XAS, where several additional effects need to be considered. These include (1) the spin−orbit coupling, (2) the atomic multiplet effect caused by the interaction between the valence electron states and the core states, and (3) the crystal-field effect from the surrounding ligands.[122] The many-body charge transfer effect due to the core−hole potential can reorder the energy of different electron configurations and is much weaker in XAS than X-ray photoelectron spectroscopy. Due to these effects, transition metal L-edge XAS can exhibit a nontrivial $L_3$ to $L_2$ ratio different from the expected 2:1.

Multiplet ligand-field theory (MLFT) is a model Hamiltonian approach describing the many-body physics of a single cation surrounded by nearest-neighbor ligands. Pertinent to the transition metal L-edge problem, in the Ballhausen notation the Hamiltonian is expressed as[133,134]

$$\begin{aligned}\hat{H} = &\sum_{i,j} \epsilon_{\mathrm{d}_{i,j}} \hat{d}_i^{\dagger} \hat{d}_j + \sum_{i,j} \epsilon_{\mathrm{p}} \hat{p}_i^{\dagger} \hat{p}_j + \zeta_{\mathrm{d}} \sum_{i,j} \langle d_i | \vec{l} \cdot \vec{s} | d_j \rangle \hat{d}_i^{\dagger} \hat{d}_j \\ &+ \zeta_{\mathrm{p}} \sum_{i,j} \langle p_i | \vec{l} \cdot \vec{s} | p_j \rangle \hat{p}_i^{\dagger} \hat{p}_j + \sum_{i,j,k,l} U_{ijkl}^{\mathrm{dd}} \hat{d}_i^{\dagger} \hat{d}_j^{\dagger} \hat{d}_l \hat{d}_k \\ &+ \sum_{i,j,k,l} U_{ijkl}^{\mathrm{dp}} \hat{d}_i^{\dagger} \hat{p}_j^{\dagger} \hat{p}_l \hat{d}_k \end{aligned} \tag{28}$$

where $\epsilon_{\mathrm{d}}$ and $\epsilon_{\mathrm{p}}$ are the d and p single-electron orbital energies and $\hat{d}_i^{\dagger}$ ($\hat{d}_i$) and $\hat{p}_i^{\dagger}$ ($\hat{p}_i$) are their creation (annihilation) operators. $U_{ijkl}^{\mathrm{dd}}$ and $U_{ijkl}^{\mathrm{dp}}$ are Hubbard $U$ parameters of the on-site d orbitals and d−p interactions, respectively. $\zeta_{\mathrm{d}}$ and $\zeta_{\mathrm{p}}$ are spin−orbit coupling constants.

Traditionally, the atomic parameters in $\hat{H}$ can be solved from single-atom calculations, while the rest are empirical parameters. There have been several efforts to determine the parameters from ab initio calculations (see, e.g., ref 134 and references therein). For a given set of parameters, the MLFT Hamiltonian can be solved efficiently to yield the eigenstates and eigenenergies, which are then used to evaluate the spectral function.

**XAS Simulation Software.** A list of XAS simulation software is summarized in Table 1, grouped according to the method used. This list is by no means meant to be complete. The most appropriate software depends on how successfully the level of theory can capture the desired physics considering computational cost as a practical concern.

*Summary.* While there are many codes that exist in the literature pertaining to the simulation of XAS data, the approach for seeking the correct solution to model the data is highly sample and element specific. In most cases, it is important to understand the quality of data, experimental limitations, and detailed systematic changes that could impact the electron and core−hole interactions and the generation of scattering paths. Close collaboration between the experimental and the theory groups is necessary to ensure that the simulated spectra are consistent with the experimental measurements.

**2.4.2. Vibrational Spectroscopy.** Vibrational spectroscopic methods, including Raman and Fourier transform infrared (FTIR)-based techniques, are powerful tools to monitor surface transformations, characterize active sites, and identify bound intermediates under reaction conditions. While FTIR probes the changes in the dipole,[111,148,149] Raman spectroscopy measures the inelastic scattering arising from changes in the polarizability due to molecular motions. Both have been widely used to experimentally study electrocatalysis.

Vibrational frequencies can also be computed from first principles—these studies are routinely used within the


https://doi.org/10.1021/acs.chemrev.3c00735
Chem. Rev. 2024, 124, 8620−8656

**Table 2. Ab Initio Computed Values for the PZC ($U_{PZC}$) vs SHE of the Pt(111)/Water Interface[a]**

| solvent model | functional | $U_{PZC}$ (V) | $\Phi_M$ (eV) | $\Delta\Phi$ (eV) | $\Delta\Phi_{el}$ (eV) | $\Delta\Phi_{ori}$ (eV) |
|---|---|---|---|---|---|---|
| explicit liquid[42] | PBE-D3 | 0.2 | 5.8 | −1.1 | −1.3 | 0.2 |
| explicit liquid[152] | rVV10 | 0.36 | 5.83 | −1.03 | −1.32 | 0.29 |
| explicit liquid—vacuum[37,38] | RPBE-D3 | 0.52 | 5.51 | −0.55 | −1.25 | 0.7 |
| explicit liquid—vacuum[152] | rVV10 | 0.56 | 5.83 | −0.83 | −1.32 | 0.49 |
| explicit liquid—CM[153] | PBE-D3 | 0.23 | 5.74 | −1.07 | −1.1 | 0.03 |
| CM[154] | PBE | 0.31 | 5.52 | −0.77 | −0.77 | 0 |
| CM[155] | RPBE | 1.13 | 5.96 | −0.39 | −0.39 | 0 |
| experiment[156−158] | | 0.2−0.3 | 5.9 | ∼−1.2 | | |

[a]The Volta potential difference ($\Delta\Phi$) and its electronic and orientational components are also shown. In each of these studies, $\Phi_{SHE}$ is set at 4.44 eV.[47] The experimental values are included for comparison.

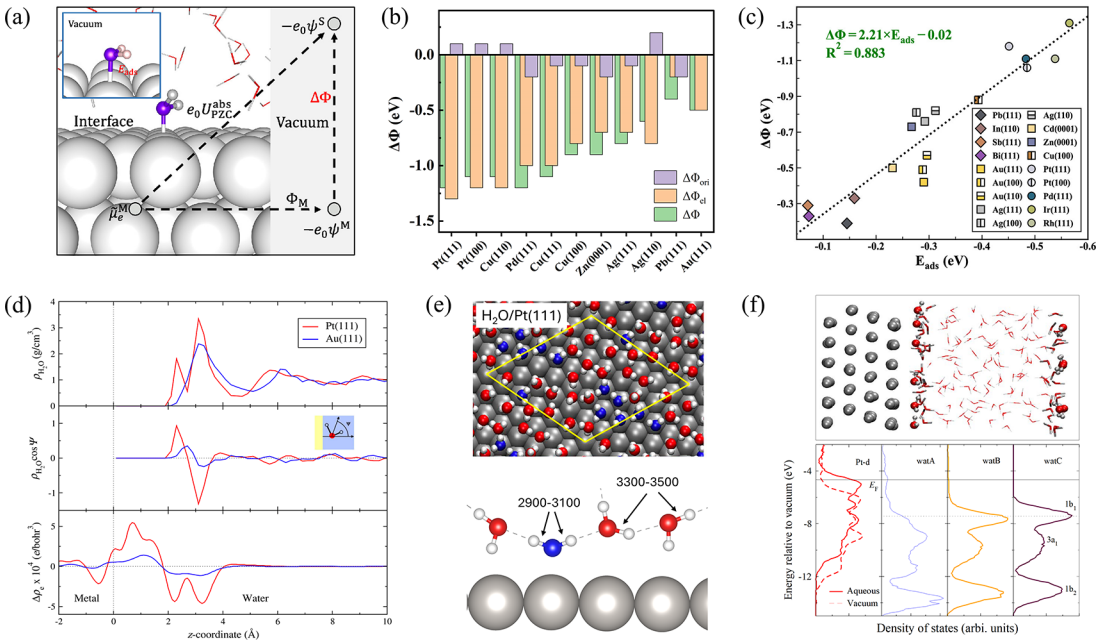


**Figure 8.** Summary of the interfacial structure and potential change at the PZC condition. (a) Schematic diagram for depicting the relationship between the PZC, the metal work function ($\Phi_M$), and the Volta potential difference ($\Delta\Phi$). (b) $\Delta\Phi$ and its decomposed $\Delta\Phi_{ori}$ and $\Delta\Phi_{el}$ for various metal/water interfaces are compared. (c) Correlation between $\Delta\Phi$ and the surface binding energy of water ($E_{ads}$). (d) The distribution of the water density ($\rho_{H_2O}$) and dipole orientation ($\rho_{H_2O}$ cos Ψ) along the surface normal direction of the Pt(111) surface is demonstrated along with the electron redistribution ($\Delta\rho_e$) at the Pt(111)/water interface. (e) An AIMD snapshot of the Pt(111)/water interface is also shown along with a proposed model of the interface water at PZC. (f) Electronic density of states of different water at the Pt(111)/water interface. (a−c) Adapted with permission from ref 162. Copyright 2021 American Chemical Society. (d and f) Adapted with permission from ref 42. Copyright 2017 American Physical Society. (e) (Top) Adapted with permission from ref 163. Copyright 2018 Science Direct. (Bottom) Adapted with permission from ref 164. Copyright 2018 Physical Chemistry Chemical Physics.

heterogeneous catalysis community to verify transition state geometries. Similar methods are also used to complement experimental adsorption studies using various probe molecules (e.g., CO, NO, deuterated acetonitrile). In the "finite difference" approach, starting from a geometry-optimized structure (obtained using the appropriate electronic structure theory method), the positions of the atoms are perturbed and the changes in the forces on each atom are measured. The change in the force for each displacement provides the Hessian matrix, which is then transformed to yield the eigenvalues and the eigenvectors. The eigenvalues represent the harmonic vibrational modes of the system that can be compared to experimental measurements. In addition to this approach, density functional perturbation theory can also be used. The latter is advantageous as the finite difference approach is often very sensitive to the size of the initial displacement.

However, these "static" approaches assume that the molecular vibrations are entirely harmonic. Although this remains a reasonable assumption for high-frequency stretching modes for gas-phase reactions, adsorbate vibrations are often strongly influenced by the dynamics of the solvent molecules under electrocatalytic conditions. In such scenarios, the phonon modes are obtained using the Fourier transform of the velocity autocorrelation function (VACF). This approach is more accurate as it captures the anharmonicity of the vibrational modes at the relevant temperatures. However, sufficiently long molecular dynamics simulations are required to ensure equilibration, which challenges the capability of AIMD. For instance, Li et al.[113] used a combination of classical molecular dynamics (LAMMPS, Reax-FF) and AIMD (VASP, PBE functional, 1 fs time step) for their studies. The system is pre-equilibrated using classical molecular dynamics (250 ps) using a previously developed reactive force field.[150] These classically


https://doi.org/10.1021/acs.chemrev.3c00735
Chem. Rev. 2024, 124, 8620−8656

derived structures are used as the starting points for subsequent AIMD runs (15−25 ps, 1 fs time step) where only the last 10 ps (i.e., $10^4$ snapshots) are used for VACF analysis and VDOS calculations. In contrast, similar simulations within the classical DFT-parametrized force field community rely on longer simulations with $10^7$−$10^8$ energy/force calls (i.e., 1−10 ns, assuming a 1 fs time step).[151] This represents a 2−3 orders of magnitude gap between the ab initio modeling and the classical simulation communities. One approach to overcome the accuracy−cost trade-off lies in the development of machine learning-based potentials capable of describing the dynamics of solid/liquid interfaces, which will be discussed in the Outlook section.

## 3. APPLICATIONS

### 3.1. Potential of Zero Charge

The potential of zero charge (PZC), which is the potential at which there is no net free charge on the electrode surface, is an important property of the electrochemical interface. In some cases, the PZC of an interface can be accurately measured experimentally[159] and can be used as a reference for validating modeled electrode/electrolyte interfaces. As listed in Table 2, the computed PZC ($U_{PZC}$) vs SHE for the Pt(111)/water interface can vary by approximately 1 V depending on the functional and solvent models employed. Using an AIMD-modeled liquid to represent the solvent phase and the cSHE to calculate the potential shows good agreement with the experimental PZC. Le et al.[42] and Bramley et al.[152] employed these methods and estimated the PZC of the Pt(111)/water interface to be 0.2 and 0.36 V vs SHE, respectively, which are both close to the experimental value of approximately 0.3 V vs SHE.[37,38,152] However, when an explicit liquid−vacuum model is used, the PZC of Pt(111) is generally overestimated by 0.2−0.3 V.[37,38,152] This error is likely due to an inaccurate description of the surface potential of the water−vacuum interface. Recent work by Li and colleagues[153] has shown that replacing the vacuum with a continuum model (CM) reduces the structural relaxation of surface water and thus lowers the error from the surface potential, resulting in a more accurate calculation of the PZC.

In developing solvation models, researchers primarily aim to accurately describe the interaction between the electrode and the solvent. However, it should be noted that the accuracy of the calculated work function of the metal surface ($\Phi_M$) also affects the $U_{PZC}$. This is related to the choice of density functional, model size, and *K*-points sampling. For instance, using the same PBE functional, the calculated $\Phi_M$ of Pt(111) may differ by approximately 0.3 eV due to differences in model size and the description of *K*-points, as presented in Table 2. To avoid this additional error and focus on the electrode−solvent interaction, the Volta potential difference ($\Delta\Phi$) is introduced.[49,160−162] This is defined as the potential difference between $\Phi_M$ and $U_{PZC}$ at the absolute scale (see Figure 8a). Table 2 reveals that the $\Delta\Phi$ computed with liquid or liquid−CM models to represent the solvation effect shows good agreement with experimental results. In contrast, large deviations from experiment are observed for models with a liquid/vacuum interface, particularly for the work of Sakong and colleagues[37,38] (−0.55 vs −1.2 eV), which suggests the existence of an underlying error in modeling the surface potential of the water/vacuum interface with AIMD simulations.

The molecular origin of $\Delta\Phi$ at the interface can be more clearly understood by separating it into two independent contributions: the potential change induced by the orientation dipole of interfacial water ($\Delta\Phi_{ori}$) and the potential change from the electron redistribution due to the electrode−solvent interaction ($\Delta\Phi_{el}$). As shown in Table 2, for all listed AIMD-simulated results, their $\Delta\Phi_{el}$ values are close to one another (1.1−1.3 eV), indicating that this effect is less dependent on the choice of density functional and model size. Therefore, the difference in $\Delta\Phi$ mainly arises from $\Delta\Phi_{ori}$. Given that the water structure at the electrode/solvent interface is similar for different AIMD simulations, the large variation in $\Delta\Phi_{ori}$ should come from the orientation dipole at the solvent/vacuum interface, which is known to be difficult to equilibrate.

Moreover, it was revealed that the $\Delta\Phi_{el}$ component of $\Delta\Phi$ plays a decisive role in the interfacial potential change at the PZC of the surface. Traditionally, electron redistribution at the interface (see Figure 8d) is considered a "pushback effect",[165] where the presence of water pushes the spilled electron back to the metal surface, causing a dipole change. In contrast, recent work suggests that it is more appropriate to assign the electron redistribution to the polarization of surface water, which is strongly supported by the observation of chemisorbed water at the interface via AIMD simulations.[42,152,153] For the Pt(111)/water interface, it is shown in Figures 8d and 8e that chemisorbed water stably sits on the top site of Pt(111) and has a characteristic peak ($z$ = 2.3 Å) in the directional distribution profile of water density. The nature of the chemical bonding with the metal surface is further confirmed by density of states (DOS) analysis of water, as shown in Figure 8f. The DOS of chemisorbed water (denoted "watA") shares some features with the d band of Pt(111).[19] Further evidence for the presence of chemisorbed water on Pt(111) is provided by the calculated O−H stretching frequency of chemisorbed water on Pt(111) at ∼3000 $cm^{-1}$ with the vibrational density of states analysis, which is largely red shifted from the vibrational frequency of bulk water (∼3400 $cm^{-1}$).[164,166] The large red shift is proposed to be caused by enhanced hydrogen bonding strength due to the electron deficiency of chemisorbed water.

The importance of surface water chemisorption in determining the interfacial potential elucidates why the DFT/CM method fails to predict the PZC accurately for reactive metals such as Pt, Pd, and Ru. Although CM models can redistribute the electrons of the metal surface through the pushback effect, careful parametrization of the model can result in a close prediction of PZC and $\Delta\Phi$ for the Pt(111)/water interface, as listed in Table 2.[152,154,155] However, this does not necessarily indicate that the electronic structure of the interface is accurately described in the DFT/CM model. As shown in Figure 8b, $\Delta\Phi_{el}$ is the dominant component of $\Delta\Phi$ for low-index metal surfaces in general. As $\Delta\Phi_{el}$ is related to the surface binding energy of water ($E_{ads}$), a linear correlation between $\Delta\Phi$ and $E_{ads}$ has been proposed. This hypothesis has been validated with data from over 20 surfaces, as depicted in Figure 8c.[162] In a subsequent study, it was suggested that the binding energy of OH* could also serve as a descriptor of $\Delta\Phi$ with the energy span in OH* binding for different materials being wider than that of water.[167] With the aid of the linear correlation shown in Figure 8c, it becomes possible to estimate the PZC of a solid/water interface without costly AIMD simulations. Additionally, it offers an approach for rationally adjusting the PZC with surface modification strategies, thus regulating the strength of the electric field at the interface and specific reaction potential. A


https://doi.org/10.1021/acs.chemrev.3c00735
Chem. Rev. 2024, 124, 8620−8656

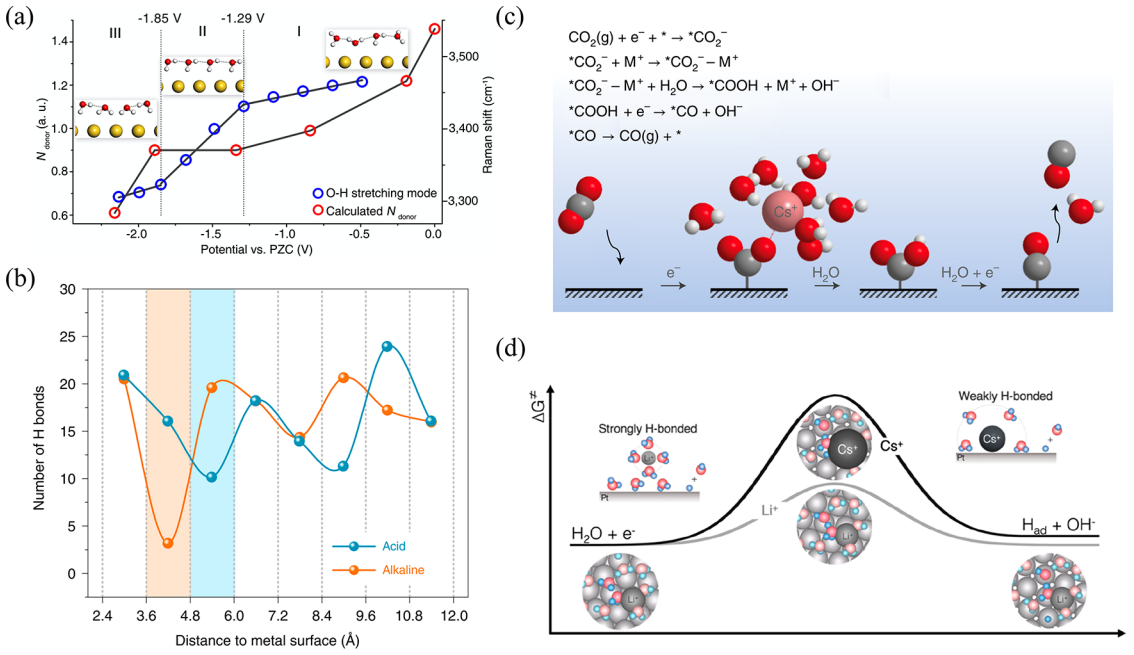


**Figure 9.** Potential- and cation-dependent structures of electric double layers. (a) Illustration of the orientation dipole and hydrogen bonding network of interfacial water on an Au(111) surface at different potentials. Adapted with permission from ref 169. Copyright 2019 Nature. (b) Distribution of water hydrogen bond numbers along the Pt(111)−*H surface normal direction at acidic and alkaline conditions. Adapted with permission from ref 113. Copyright 2022 Nature. (c) Hydration structure of a $Cs^+$ ion at the interface and its interaction with surface-adsorbed $CO_2$. Adapted with permission from ref 170. Copyright 2021 Nature. (d) Demonstration of the cation-dependent interfacial water hydrogen bonding network and its relevance to the energy of the Volmer reaction. Adapted with permission from ref 171. Copyright 2021 American Chemical Society.

similar concept has been used to understand the promotion of the alkaline hydrogen evolution reaction (HER) activity on the Pt surface after Ni or $Ni(OH)_2$ deposition.[157,168]

### 3.2. Structure and Capacitance of Electric Double Layers

Electrochemical interface modeling has seen recent use as a method to better understand how the microscopic structure of metal/aqueous solution interfaces responds to varying electrochemical conditions. For instance, Salmeron et al.[172] utilized XAS to elucidate the EDL structure of a Au(111) surface as a function of potential. They found that decreasing the potential breaks hydrogen bonds of interface water and orients the dangling hydrogens toward the surface. Li et al.[169] have recently investigated the potential-dependent structure of interfacial water at Au(111)/aqueous solution interfaces, as depicted in Figure 9a. At the PZC, it was found that interfacial water has no preferred orientation. By negatively shifting the potential to −1.29 V vs PZC, nearly all interfacial water reorients with one O−H bond pointing down to the surface, forming what is called "one-H-down" water. This configuration remains stable within a wide potential window (from −1.29 to −1.85 V vs PZC) and is attributed to the combined effects of the water−field dipole interaction, water−water hydrogen bonding, and water−metal short-range electrostatic interaction. Negatively shifting the electrode potential further causes the one-H-down water to turn into a configuration where both O−H bonds point toward the electrode surface. This change is due to the alignment of the water dipole with the electric field, which breaks the stabilized hydrogen bonding network formed by the one-H-down water structure. The potential-dependent structural changes of water were found to be well correlated with changes in the O−H stretching frequency of water measured with in situ Raman spectroscopy as shown in Figure 9a. The trends were attributed to a synergistic effect between a vibrational Stark effect and a change in the number of hydrogen bonds with potential.

At potentials more positive than the PZC, water prefers to orient with its "O" atom pointing toward the surface due to electrostatic interactions with the interfacial electric field. It should be noted that the configuration of the "O-down" water is also constrained by the water−surface chemical interaction, i.e., the hybridization of the $1b_1$ orbital of water and the d band of the metal. Recently, Le et al. reported that on the positively charged Pt(111) surface, the surface plane of water is only tilted by ∼30° and forms a two-dimensional hydrogen bonding network in the surface plane direction.[173] The orientation of water is expected to have more freedom on less reactive metal surfaces, such as Au and Ag.[174] Recent findings have also shown that the surface charge density impacts not only the structure of the first water layer but also that of subsequent water layers. Figure 9b illustrates the comparison of the structure of Pt(111)−*H/aqueous solution interfaces at HER potentials modeled by Li and co-workers.[113] They found that in alkaline conditions (where the surface is more negatively charged), the number of hydrogen bonds formed at the subwater layer is significantly lower than in acidic conditions (where the surface is less negatively charged). Based on the similar hydrogen binding energies (HBE) in acidic and alkaline conditions, Li et al. suggested that the difference in hydrogen bond connectivity, which affects interfacial proton transfer, is the main reason for the sluggish HER activity of Pt in alkaline solution.

Recent research using AIMD has also investigated the solvation structure of ions (primarily cations) at interfaces. The results have shown that the ion solvation structure is dependent on both the surface charge density and the ionic nature. Under conditions of low surface charge, the hydration shell around the ion is complete, whereas at high surface charge, the hydration shell will be partially peeled off, resulting in direct


https://doi.org/10.1021/acs.chemrev.3c00735
Chem. Rev. 2024, 124, 8620−8656

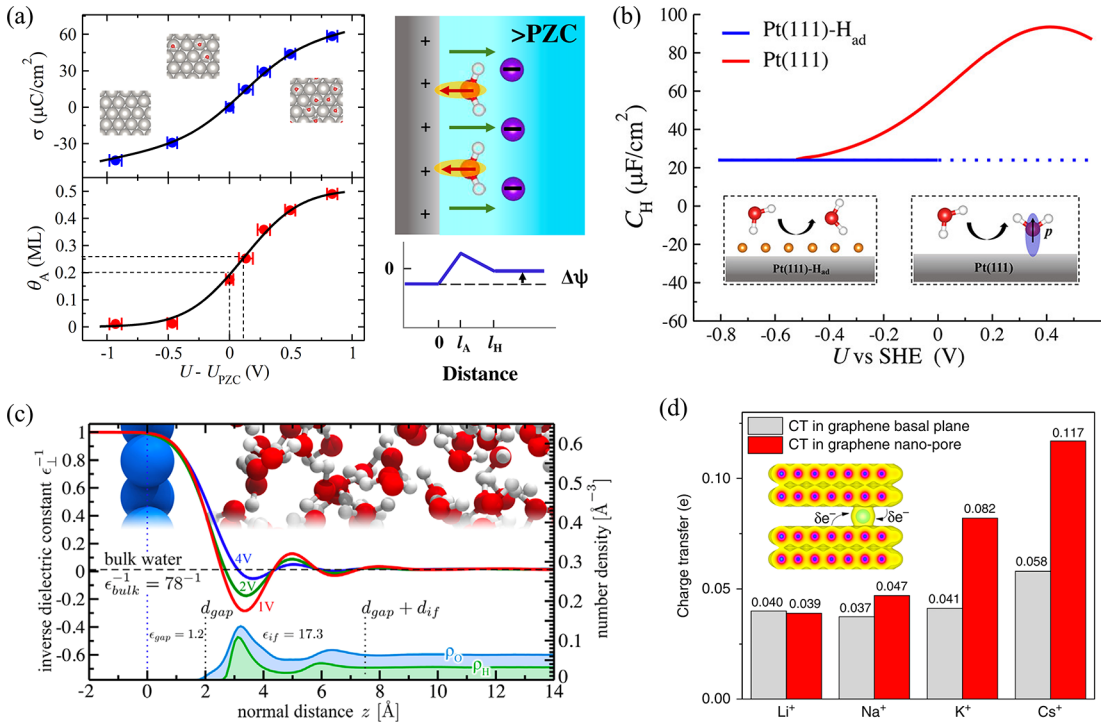


**Figure 10.** New insights into the interfacial capacitance beyond the conventional Helmholtz model. (a) Incorporation of a chemisorbed water layer within the Helmholtz model with its surface coverage proposed to follow the Frumkin adsorption isotherm. Adapted with permission from ref 173. Copyright 2020 Science under [CC BY 4.0] [https://creativecommons.org/licenses/by/4.0/]. (b) Comparison of the differential Helmholtz capacitance curve in the presence and absence of the water chemisorption layer. Adapted with permission from ref 175. Copyright 2021 American Chemical Society. (c) Modeling of the electrostatic potential distribution profiles at a graphene/water interface under different applied potentials using classical MD. Adapted with permission from ref 73. Copyright American Physical Society under [CC BY 4.0] [https://creativecommons.org/licenses/by/4.0/]. (d) Comparison of the extent of charge transfer between different cations and graphene. Adapted with permission from ref 185. Copyright 2019 Nature under [CC BY 4.0] [https://creativecommons.org/licenses/by/4.0/].

contact between the ion and the surface.[175] Additionally, ions with lower hydration energies, such as $Cs^+$, are more easily dehydrated than those with higher hydration energies, such as $Li^+$.[176−178] This indicates that the ion solvation structure at the interface is a result of the competition between the surface charge and the ion hydration energy.[170,177−184] Electrolyte cations play important roles in various reactions. They can affect the stability of reaction intermediates (see Figure 9c)[170,177−184] or change the hydrogen bonding network of the solvent (see Figure 9d),[171] thereby promoting or suppressing the reaction. The role of cations in catalysis will be discussed in greater detail in section 3.3 in the context of the HER on Pt(111).

The traditional view of the Helmholtz layer at an electrochemical interface describes its behavior as a parallel-plate capacitor, where the solvent inside serves as a uniform dielectric medium. However, recent theoretical studies have challenged this view. For instance, it has been pointed out that there is often some form of chemisorbed water at the reactive metal/aqueous interface. As shown in Figure 10a, its surface coverage ($\theta_A$) depends on the electrode potential, following the Frumkin adsorption isotherm.[173,186] The newly proposed Helmholtz model considers this chemisorbed water explicitly due to its polarized dipole from chemical bonding with the metal surface. As the electrode potential is shifted, the dipole of the chemisorbed water layer changes in the opposite direction to the charging of the surface. Thus, it was expected that the behavior of the potential-dependent $\theta_A$ can enhance the capacitance of the interface. Figure 10b shows the differential Helmholtz capacitance versus potential computed by AIMD for the Pt(111)/aqueous solution interface, and it is a bell-shaped curve. A similar shape has been observed in experiments for the measured differential Helmholtz capacitance of nearly all transition metals in aqueous solution.[187−189] Conventionally, the formation of the capacitance peak was thought to be due to the structural reorientation of interfacial water at high potential bias.[81] However, based on the AIMD simulation results, Le et al.[173] proposed that the capacitance peak is formed due to the adsorption/desorption of water at varying potentials. This explanation was further supported by modeling Pt(111)−*H/water interfaces, in which all of the Pt(111) sites were passivated by hydrogen atoms, preventing water adsorption. As shown in Figure 10b, without potential-dependent water chemisorption, the Helmholtz capacitance is nearly constant with changing electrode potential.[175]

Another layer of complexity regarding the Helmholtz layer is the existence of a low dielectric region, also known as the gap layer, between the electrode and the solvent. This gap layer is suggested to be present due to Pauli repulsion, and its width is dependent on the electrode material.[73,190,191] As shown in Figure 10c, Deißenbeck et al.[73] conducted classical MD simulations and found a 2 Å wide gap region for an inert electrode/water interface. The computed dielectric constant inside the gap was found to be only 1.2, which is close to the permittivity of vacuum. However, it should be noted that the gap width is generally overestimated in classical MD simulations due to a simplified representation of the electrode charge. Recently, Li et al.[163] calculated the electronic structure of the electrode and found that the gap width for the graphene/aqueous solution


https://doi.org/10.1021/acs.chemrev.3c00735
Chem. Rev. 2024, 124, 8620−8656

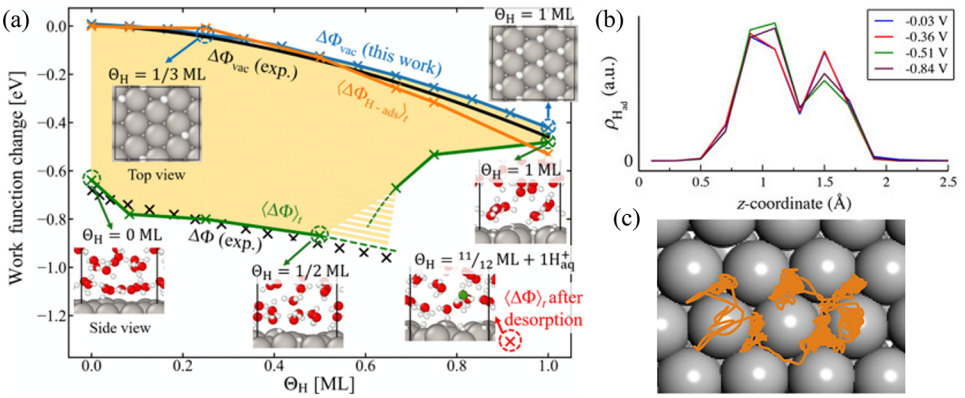


**Figure 11.** (a) Hydrogen coverage versus work function under vacuum (blue) and in explicit water solvent (green). In solution, the work function experiences a kink around $\Theta_H \approx 0.66$ ML. The gray, red, white, and green spheres represent Pt, the H and O of water, and the O of $H_3O^+$ (after *H desorption), respectively. (b) Hydrogen distribution as a function of potential (referenced to SHE). The peak at $z \approx 1$ Å corresponds to the hollow sites, and the peak at $z \approx 1.5$ Å corresponds to the top sites. (c) Representative hydrogen trajectory on Pt(111) during 10 ps of AIMD. (a) Adapted with permission from ref 203. Copyright 2021 American Physical Society under [CC BY 4.0] [https://creativecommons.org/licenses/by/4.0/]. (b and c) Adapted with permission from ref 175. Copyright 2021 American Chemical Society.

interface is approximately 1.4 Å, while for transition metals such as Cu, the gap is nearly absent due to surface spilled over electrons. The low dielectric constant of the gap layer can explain why the AIMD-computed Helmholtz capacitance of graphene is much lower than that of transition metals. Recent studies have also revisited the effect of cations on the interfacial capacitance. The capacitance trend $Cs^+ > K^+ > Li^+$ has been measured on different electrode materials, such as a CO-covered Pt(111) surface,[192] graphene,[193] and highly ordered pyrolytic graphite,[194] and is generally attributed to the difference in their hydration radius. $Cs^+$ has the lowest hydration radius and thus stays closest to the surface, resulting in the highest capacitance. However, it has also been proposed that $Cs^+$ may have an overscreening effect[195,196] due to its ability to dehydrate at the interface, which is supported by infrared spectroscopy results that indicate the measured concentration of $Cs^+$ at interface is much higher than that of other alkali metal ions.[197] It was proposed that the overscreening effect can increase the interfacial capacitance, which was then confirmed by AIMD simulations.[195] For graphene, another possible explanation for the cation-dependent capacitance was suggested: it was proposed by Zhan et al.[89] that dehydrated cations can have partial charge transfer with graphene, and the amount of transferred electrons follows the trend $Cs^+ > K^+ > Li^+$, as shown in Figure 10d. The phenomenon of cation-specific adsorption can significantly alter the quantum capacitance of graphene, thereby enhancing the total interfacial capacitance.

### 3.3. Mechanism of the HER on Pt(111)

The hydrogen evolution reaction (HER) on Pt(111) is among the most extensively studied electrochemical systems due to its relative simplicity and practical importance. Here, we review new insights into hydrogen coverage and HER kinetics enabled by advanced simulations.

**3.3.1. H Coverage.** The distribution of hydrogen atoms on the platinum surface is an ongoing research topic. Even at potentials above the reaction equilibrium potential (0 V vs RHE), hydrogen atoms are already deposited on the surface of Pt.[198] These adsorbates are referred to as underpotential deposited (UPD) H. Experiments suggest that approximately two-thirds of the surface is covered at the equilibrium potential.[199,200] Consistent with this, Nørskov et al.[201] and Chan et al.[202] calculated the differential free energy of *H formation on the hollow sites of Pt(111) versus coverage and found that indeed it reaches zero at approximately 2/3 ML and 0 V vs RHE. The saturation of UPD H was also investigated through AIMD simulations by Neugebauer et al.[203] by computing the work function in both a vacuum (blue) and a solvated environment (green) as a function of hydrogen coverage, as shown in Figure 11a. Their calculation with explicit water molecules included planar neon as a counter electrode. All of the hydrogen atoms are placed in hollow sites. In their simulation with explicit solvation, the work function steadily decreases as the hydrogen coverage increases up to $\Theta_H < 0.66$ ML. At $\Theta_H \approx 0.66$ ML, the work function exhibits an inflection point at which it begins to sharply increase, thereby suggesting continued hydrogen adsorption is unfavorable. They further corroborate this conclusion by demonstrating that one of the H adatoms spontaneously desorbs in their $\Theta_H = 1$ ML simulation after about 25 ps. They attribute the critical saturation of $\Theta_H = 0.66$ ML to the waters reaching a maximum electric field screening from reorientation.

It should be noted that the *H are mobile and may diffuse between the hollow sites and the top sites. To investigate this, Laasonen et al.[204] performed 40 ps AIMD simulations with explicit water. They considered multiple coverages with *H occupying the hollow sites and observed that *H diffused to the top sites during equilibration. As they increased the coverage, they found *H mobility decreased due to repulsion from nearby adatoms. Cheng et al.[175] expanded on this work by running 10 ps AIMD simulations with explicit water and sodium ions. They varied the sodium ion concentration to tune the electrode potential, which they determined using the cSHE. Their results suggest that at $\Theta_H = 2/3$ ML, roughly 1/6 ML of *H resides on the top sites (with 1/2 ML at the hollow sites) under applied potentials below −0.5 V vs SHE. As the potential increased, a greater proportion of *H occupies the top sites. These trends are summarized in Figure 11b. In contrast to Laasonen et al.'s prediction that *H remains top bound, they found that *H exhibits facile diffusion back and forth between the hollow and the top sites during AIMD, as shown in Figure 11c.

**3.3.2. Kinetics—Acidic.** Under acidic conditions, the HER proceeds by the following elementary steps


https://doi.org/10.1021/acs.chemrev.3c00735
Chem. Rev. 2024, 124, 8620−8656

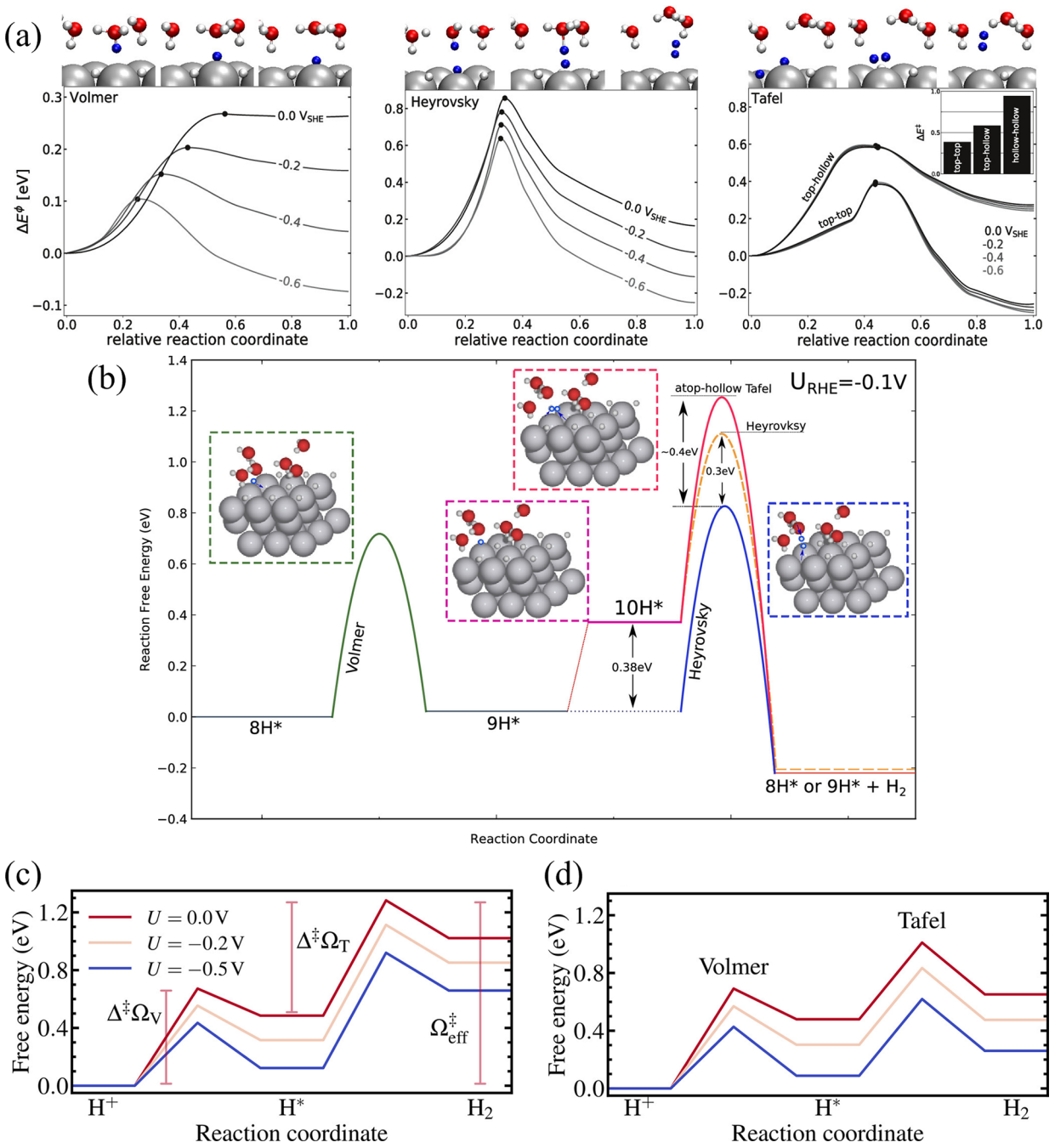


**Figure 12.** (a) Reaction profiles of the Volmer, Heyrovsky, and Tafel steps of the HER at various electrode potentials. The structural snapshots depict the initial, transition, and final states. The bar graph inset for the Tafel mechanism shows that the activation energy follows the trend (top−top) < (top−hollow) < (hollow−hollow). The white, blue, red, and silver atoms represent passive hydrogen, participating hydrogen, oxygen, and platinum, respectively. (b) Reaction profile comparing the barriers for the Heyrovsky step at 1 ML in the hollow sites (9 *H) and the Heyrovsky/Tafel steps at >1 ML with an additional atop *H (10 *H). The Heyrovsky step at 1 ML exhibits the lowest barrier due to the unfavorable adsorption of top-bound *H. (c and d) Free energy profiles for the Volmer−Tafel mechanism for 2/3 ML coverage (c) and 1 ML coverage (d). The potentials are referenced to SHE. (a) Adapted with permission from ref 211. Copyright American Chemical Society. (b) Adapted with permission from ref 202. Copyright 2020 American Chemical Society. (c and d) Adapted with permission from ref 212. Copyright 2021 American Chemical Society under [CC BY 4.0] [https://creativecommons.org/licenses/by/4.0/].

Volmer: $H_3O^+ + e + * \rightarrow {}^*H + H_2O$ (step 1)

Tafel: ${}^*H + {}^*H \rightarrow H_2 + *$ (step 2a)

Heyrovsky: $H_3O^+ + e + {}^*H \rightarrow H_2 + * + H_2O$ (step 2b)

where * depicts the active site of the catalyst and *H is an adsorbed hydrogen atom. The HER initiates with the Volmer step and completes a catalytic turnover through either the Heyrovsky step or an additional Volmer step followed by the Tafel step. These pathways are called the Volmer−Heyrovsky and Volmer−Tafel mechanisms, respectively. It is valuable to know the dominant pathway and the rate-limiting step. In


https://doi.org/10.1021/acs.chemrev.3c00735
Chem. Rev. 2024, 124, 8620−8656

principle, these can be determined experimentally by measuring the Tafel slope and comparing it to a kinetic model. However, many have argued that the kinetic measurements of the HER on Pt in acidic conditions are corrupted by mass transport limitations at any potential.[205,206] This indicates that experimentally measured Tafel slopes may not reflect the intrinsic reaction kinetics.[207]

Several experimental studies have measured the apparent activation energy. Markovic et al.[199] studied the HER over platinum single crystals with different facets in a 0.05 M $H_2SO_4$ solution, reporting an activation energy of 0.19 eV on Pt(111) near the reversible potential ($|\eta| < 10$ mV). Schmickler et al.[208] also examined Pt(111) in 0.05 M $H_2SO_4$ at a slightly higher overpotential (60 mV < $|\eta|$ < 150 mV) and measured an activation energy closer to 0.5−0.6 eV. Zeradjanin et al.[209] recently measured the HER kinetics of flat polycrystalline electrodes in 0.1 M $HClO_4$ and reported an activation energy of 0.5 eV at 0 V vs RHE. Similar to Tafel slopes, mass transport limitations can corrupt measured apparent activation energies. Thus, caution must be taken when interpreting the data, and more reliable experimental measurements are needed for comparison with computational models.

Nørskov et al.[201] were among the first to computationally analyze the kinetics of the HER on Pt(111). They employed size extrapolation to treat the constant electrode potential effect and included an explicit ice bilayer to describe the solvent. They ran static NEB calculations at various hydrogen coverages and extrapolated the reaction barriers at 0 V vs SHE. They obtained reaction barriers of 0.69, 1.40, and 0.85 eV for the Volmer, Heyrovsky, and Tafel reactions, respectively. Their results suggest the HER proceeds through the Volmer−Tafel mechanism and the Tafel step is rate limiting. Jónsson et al.[210] also performed NEB calculations of the HER on Pt(111) with 1 ML H coverage in the hollow sites as well as size extrapolation to account for the constant potential. They considered both an ice bilayer and an eigencluster model combined with VASPsol's implicit solvation model. They observed 0.87 and 0.81 eV barriers for the Tafel reaction with the cluster and bilayer models, respectively. The Heyrovsky step exhibited barriers of 1.41 and 1.62 eV for the cluster and bilayer models, thereby supporting that the Tafel mechanism is dominant. However, the cluster model only displayed a 0.48 eV barrier for the Volmer step, whereas the bilayer had a 0.69 eV barrier. They attribute this discrepancy to the flexibility of the cluster model, which can more easily maintain the hydrogen bonding network throughout the reaction. Thus, their results agree with Nørskov et al. in that the Tafel step is rate limiting.

Peterson et al.[211] employed the climbing-image NEB method with the solvated jellium model and explicit ice bilayers. Their model includes a full monolayer of *H in the hollow sites with an additional top-bound *H as the HER active intermediate. The reaction barriers under potentials ranging from 0 to −0.6 V vs SHE are shown in Figure 12a. At 0 V vs SHE, they found that the activation energies of the Volmer, Heyrovsky, and Tafel steps were approximately 0.27, 0.83, and 0.40 eV, respectively. As such, their results concur that the Tafel mechanism is preferred and that the Tafel step is rate limiting in the relevant overpotential regime. They found that the barrier for the Tafel step was minimized by the combination of two top-bound *H rather than combining the top-bound *H with *H in the hollow sites.

Chan et al.[202] also studied the HER kinetics using explicit water clusters to describe solvation, charge extrapolation to address the constant potential, and NEB to calculate the barriers. They considered an applied potential of −0.1 V vs RHE to obtain 1 ML H coverage on the hollow sites. They compared the pathways involving the hollow *H at 1 ML and the atop *H at >1 ML. The reaction profile is displayed in Figure 12b. They found that top-bound *H is unlikely to play a role in the HER mechanism. Instead, they observed the HER proceeds through the Volmer−Heyrovsky mechanism involving hollow *H with a barrier of 0.69 eV for the Volmer step, 0.77 eV for the Heyrovsky step, and 1.24 eV for the Tafel step. They also performed microkinetic modeling assuming a charge transfer coefficient of 0.5 and found a Tafel slope of 120 mV/dec.

Each of the above references used the NEB method to identify the transition state and obtain the activation energy; however, as discussed in section 2.3, NEB cannot account for statistically diverse solvent geometries present at room temperature. To address this limitation, Laasonen et al.[212] used constrained molecular dynamics and thermodynamic integration to more accurately model the surface water interface. They used charge extrapolation to include the constant-potential effect. The reaction profiles at $\Theta_H$ = 2/3 ML and $\Theta_H$ = 1 ML are shown in Figure 12c and 12d, respectively. For both the Volmer and the Tafel steps, only top-bound *H is considered and the hollow sites are bare in accordance with their previous results. They obtained the following kinetic barriers. Volmer: 0.67 eV (1 ML), 0.69 eV (2/3 ML). Tafel: 0.53 eV (1 ML), 0.80 eV (2/3 ML). They only considered the Volmer−Tafel mechanism and did not investigate the competitive Heyrovsky mechanism. However, the shallow thermodynamic well of H* causes the apparent activation energy to be greater than 1 eV for both coverages, which is too large to explain the facile HER kinetics observed on Pt in acidic conditions.

**3.3.3. Kinetics—Alkaline.** In alkaline conditions, the proton source for the HER changes from hydronium to water. $H_2O$ is known to have greater resistance to dissociation than $H_3O^+$, thereby raising the HER activation energy.[105,213] The reaction elementary steps in basic solution are as follows

$$\text{Volmer: } H_2O + e + * \rightarrow {}^*H + OH^- \quad \text{(step 1)}$$

$$\text{Tafel: } {}^*H + {}^*H \rightarrow H_2 + * \quad \text{step 2a)}$$

$$\text{Heyrovsky: } H_2O + e + {}^*H \rightarrow H_2 + * + OH^- \quad \text{(step 2b)}$$

It is possible that the hydroxide produced from water dissociation is adsorbed on the catalyst surface, but most studies show that this is not the case for Pt and less oxophilic metals.[214] Similar to acidic conditions, experimental kinetic studies have been conducted to attempt to identify the rate-determining steps for the HER in alkaline electrolytes. As the kinetics of the HER are known to be ∼2 orders of magnitude slower at pH 13 than those at pH 1, experimental measurements are more likely to reflect intrinsic reaction kinetics rather than transport rates.[215] In principle, Tafel analysis can be performed to understand the nature of the rate-limiting step as each step will yield different Tafel slopes. It is important to note that cardinal values of the Tafel slope are made with assumed values of adsorbate coverage.[216] Many studies have argued that the Volmer step is rate limiting over Pt based on measured Tafel slopes close to 120 mV/decade. However, this Tafel slope is also consistent with the Heyrovsky step being rate limiting if the *H coverage is close to 1 ML.[216] As for the apparent activation energy under alkaline conditions, Markovic et al.[217] exper-


https://doi.org/10.1021/acs.chemrev.3c00735
Chem. Rev. 2024, 124, 8620−8656

Table 3. Experimental and Computational HER Mechanism and Kinetic Barriers on Pt(111)[a]

| publication | system | method | barriers | mechanism |
|---|---|---|---|---|
| Markovic[199] (1997, Exp) | acid; 0.05 M $H_2SO_4$; $\|\eta\|$ < 10 mV | | A, 0.19 | |
| Schmickler[208] (2017, Exp) | acid; 0.05 M $H_2SO_4$; 60 mV < $\|\eta\|$ < 150 mV | | A, 0.5−0.6 | |
| Nørskov[201] (2010, DFT) | acid; various ML; hollow *H | NEB; size extrapolation, ice bilayer | V, 0.69; H, 1.40; T, 0.85 | Tafel |
| Jónsson[210] (2019, DFT) | acid; 1 ML coverage; hollow *H | NEB; size extrapolation, ice bilayer | V, 0.69; H, 1.62; T, 0.81 | Tafel |
| Jónsson[210] (2019, DFT) | acid; 1 ML coverage; hollow *H | NEB; size extrapolation, eigencluster | V, 0.48; H, 1.41; T, 0.87 | Tafel |
| Peterson[211] (2019, DFT) | acid; 1 ML coverage; hollow *H | NEB; solvated jellium, ice bilayer | V, 0.27; H, 0.83; T, 0.4 | Tafel |
| Chan[202] (2020, DFT) | acid; −0.1 V vs RHE; 1 ML coverage; hollow *H | NEB; solvated jellium, water clusters | V, 0.69; H, 0.77; T, 1.24 | Heyrovsky |
| Laasonen[212] (2021, DFT) | acid; 2/3 ML coverage; atop *H | cMD; charge extrapolation | V, 0.67; T, 0.80; A, 1.28 | Tafel (assumed) |
| Laasonen[212] (2021, DFT) | acid; 1 ML coverage; atop *H | cMD; charge extrapolation | V, 0.69; T, 0.53; A, 1.01 | Tafel (assumed) |
| Chan[105] (2019, DFT) | acid; dilute *H | NEB; charge extrapolation; ice monolayer | V, 0.04; H, 0.20; T, 0.72 | Heyrovsky |
| Markovic[217] (2002, Exp) | base; 0.1 M KOH; ∼0 V vs RHE | | A, 0.48 | |
| Chan[105] (2019, DFT) | base; dilute *H | NEB; charge extrapolation; ice monolayer, $Na^+$ cation | V, 0.42; H, 1.20; T, 0.72 | Heyrovsky |

[a]All barriers are at 0 V vs SHE (unless otherwise specified) and are given in terms of eV. For the barriers, A is the apparent barrier, V is the barrier for the Volmer step, H is for the Heyrovsky step, and T is for the Tafel step.

imentally measured the apparent HER activation energy of Pt(111) in 0.1 M KOH to be 0.48 eV at the reversible potential.

Chan et al.[105] computationally evaluated HER barriers on Pt(111) in both acidic and basic solutions to elucidate reasons for measured differences in activity. They utilized an ice monolayer with $H_3O^+$ as the proton source for the acidic simulations and an ice bilayer with an explicit sodium cation for alkaline conditions where the proton donor is $H_2O$. They did not include any H adsorbed prior to the Volmer step. The potential effects were assessed with the charge extrapolation method. They evaluated kinetic barriers via climbing-image NEB and fit their results to a microkinetic model. The activation energies are as follows: Volmer, acidic 0.04 eV; Volmer, alkaline 0.42 eV; Heyrovsky, acidic 0.20 eV; Heyrovsky, alkaline 1.20 eV; Tafel (both conditions) 0.72 eV. Their calculated Tafel barrier had a large uncertainty at 0.3 eV, and the resulting microkinetic model depended greatly on this value. To better match experimental behavior, they constructed polarization curves with different Tafel barriers. They observed that the Tafel-mediated HER (with a Tafel barrier of 0.62 eV) exhibited an additional flat region at low current densities/overpotentials, which is not consistent with experimental polarization curves. Conversely, the Heyrovsky-mediated HER (with a Tafel barrier of 0.77 eV) followed the same qualitative trends as experiments. They concluded from this comparison that the Heyrovsky mechanism is preferred under both acidic and alkaline conditions. They confirm that the lower HER rate in alkaline conditions relative to acidic conditions is primarily due to the higher barrier for water dissociation.

Abild-Pedersen et al.[218] have circumvented the immense computational costs of simulating charge transfer and solvent thermal fluctuations by developing a novel technique that separates the potential energy surfaces of the solvent and substrate. The interaction is recovered through adiabatic coupling, and the potential energy surface is tuned to the applied potential. This method allows them to examine diverse solvent structures and hydrogen coverages. They observe that the electrode−water distance affects the relative degree of rate control for the Heyrovsky and Tafel steps, suggesting that the solvent dynamics play a critical role in determining the overall reaction mechanism. They also construct theoretical $I-V$ curves at pH 13 and determine that the Tafel mechanism dominates at small overpotentials (<−0.23 V vs RHE), whereas the Heyrovsky mechanism is preferred at larger overpotentials.

It should be noted that for the HER under alkaline conditions, the choice of electrolyte cation in solution plays an important role. Experiments show that on Pt, Pd, and Ir, the HER rates decrease as the cation size increases (i.e., $Li^+ > Na^+ > Rb^+ > Cs^+$), while on Au, Ag, and Cu, the activity trend is in the opposite direction.[176,219] Various theories have been put forth, but they either fall short of fully explaining the experimental data or lack sufficient evidence. For example, (1) one popular theory is that cations modify the water dissociation energetics,[171,176,220,221] which implies either the Volmer or the Heyrovsky step is rate limiting for the alkaline HER. As the cation size increases, its hydration becomes weaker, and thus, it more easily approaches the electrode surface.[171,176,220−222] Some studies have suggested that a larger, closer-to-surface cation lowers the barrier by more readily stabilizing the $OH^-$ generated from water dissociation,[176] while others have argued against this notion[171] as they believe large cations destroy the hydrogen bonding structure and thus slow the HER. Neither effect in isolation can explain the opposite activity trends observed for Cu/Ag/Au and Ir/Pd/Pt. (2) In addition to modifying the energetics of water dissociation, cations are also proposed to influence the removal of $OH^-$ from the surface to the bulk solution.[176] However, there is ongoing debate about whether cations facilitate[223] or impede[176] this removal. (3) For Pt, in addition to directly influencing water dissociation, it has been suggested that alkali metal cations indirectly affect the HER by altering the concentration of hydroxyl adsorbates on the surface.[221] In this theory, a higher concentration of *OH results in a higher HER


https://doi.org/10.1021/acs.chemrev.3c00735
Chem. Rev. 2024, 124, 8620−8656

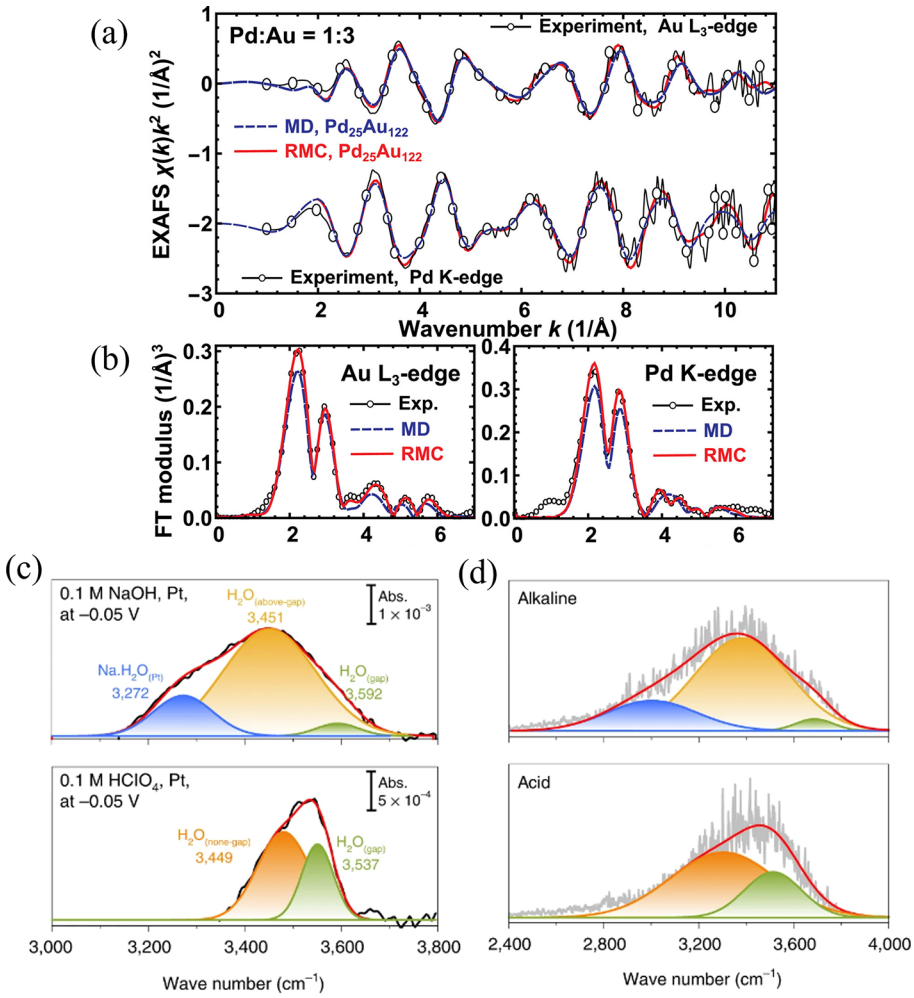


**Figure 13.** (a) PdAu nanoparticle EXAFS spectra for the Au $L_3$-edge and the Pd K-edge. (b) Fourier transform of the EXAFS data. In both figures, the black circles represent experimental data, the blue curve shows the MD-EXAFS data with the best fit, and the red curve shows the MD-EXAFS data after RMC/EA refinement. (c) Deconvolution of the experimental O−H stretching vibration peak at −0.05 V vs SHE. (d) Deconvolution of the computational O−H stretching vibration peak at −0.05 V vs SHE. (a and b) Adapted with permission from ref 228. Copyright 2017 AIP Publishing. (c and d) Adapted with permission from ref 113. Copyright 2022 Nature.

rate because it promotes water dissociation by acting as both an electronically favored proton acceptor and a geometrically favored proton donor. Larger cations destabilize the *OH, thereby lowering the HER rate. Although this may be true for ultrathin Pt nanowires,[221] the presence of *OH species on the flat Pt(111) surface is generally considered negligible, if not entirely absent.[214] (4) Larger cations are suggested to block the active sites more readily. However, such blocking occurs only under conditions of high overpotential or elevated cation concentration.[224] More experimental and computational studies are needed to further understand cation effects.

**3.3.4. Summary.** Each of the results discussed above are summarized in Table 3. There is no clear consensus on the kinetic mechanism for the HER over Pt. The variance in computational data can be attributed to the use of different methods, which have different treatments for the solution, electrode potential, and H coverage. To obtain more accurate results, we recommend the use of constant-potential AIMD plus hybrid solvation.[45,61] As discussed in section 2, constant-potential AIMD can sample numerous structures and charge states, and hybrid solvation can account for the chemical interaction between the catalyst/adsorbate and the solution as well as implicit electrolyte ions. The system size should be as large as possible, and the simulation time should also be as long as possible to ensure sufficient sampling. Advanced enhanced sampling techniques can be used to accelerate the sampling. Moreover, we notice most computational studies for alkaline conditions do not include explicit cations, which play an important role as discussed above. Therefore, we recommend revisiting those studies with the inclusion of explicit cations.

Although there are limited amounts of experimental data, interpreting the data needs special caution. Particularly, under acidic conditions where the HER is generally fast, it is challenging to measure the true reaction kinetics due to convolution by the mass transport as discussed in the Kinetics—Acidic section. Mass transport is also important in the context of CO2R, where improved hydrodynamics are found to change ethylene and methane Tafel slopes.[225] It is also worth noting that in addition to the activation energy, the pre-exponential frequency factor in the Arrhenius equation is also important to the reaction kinetics. For example, Zeradjanin et al.[209] showed that the most HER-active metals have higher activation energies than other d-block metals, which affirms the importance of the frequency factor on the activity trends. Development of experimental techniques to accurately resolve these kinetic quantities is highly desired.


https://doi.org/10.1021/acs.chemrev.3c00735
Chem. Rev. 2024, 124, 8620−8656

### 3.4. Spectrum Calculation Examples

Computational XAS has proven to be a powerful method to help resolve catalyst structure and charge state. Co−oxyhydroxides ($CoO_x(OH)_y$) have emerged as potential catalysts for the oxygen evolution reaction (OER). Their activities are highly dependent on the oxidation state and the coordination environment of Co. Furthermore, the OER is known to induce structural changes that obfuscate operando spectroscopic data. To help resolve the structure and charge state, Bergmann et al.[226] performed computational XANES with DFT+U calculations and BSE to study the performance of four distinctly synthesized Co−oxyhydroxide electrocatalysts. By comparing their spectra to operando XANES, they determine that approximately 70% of $Co^{2+}$ in the Co−oxyhydroxides oxidized to $Co^{3+}$ and $Co^{4+}$ after OER conditioning. Furthermore, they demonstrate that each of their Co−oxyhydroxide catalysts transform into a universal highly active structural motif under the OER, regardless of the initial configuration. Thus, their computational spectroscopic calculations elucidated in situ structural changes that were inaccessible through experimental analysis alone. The authors suggest that these findings were not limited to Co-based electrocatalysts and could be applicable to general structure evolution for similar materials during the OER.

Metallic nanoparticles (NPs) are excellent candidates for catalysis due to their physical and chemical tunability.[227] XAS is often used as a powerful tool to probe the structure of monometallic and multimetallic nanomaterials and to correlate the structure of NPs with their chemical and catalytic properties. However, conventional approaches to analyze XAS overlook the heterogeneity of the NPs. A more accurate approach is to directly calculate the XAS of hypothetical structures and compare them with experimental data, which avoids artifacts of conventional EXAFS analysis based on the nonlinear least-squares fitting. For example, Frenkel et al.[228] ran classical MD simulations of bimetallic PdAu NPs to generate thousands of structures that were then analyzed with FEFF to determine the ensemble-averaged EXAFS data. They compared their results to experiments and determined their spectra obtained from classical MD were sufficient to distinguish NPs of different size and composition. However, the interatomic distance distribution, which is critical for resolving experimental EXAFS, remained ambiguous. Although AIMD could produce a more accurate distribution of structures, high computational cost prohibits its usage for NPs of significant size. They instead refined their MD data through a reverse Monte Carlo (RMC) and evolutionary algorithm (EA) method. This approach involves rapidly screening EXAFS of slightly displaced structures to potentially discover a closer match with experiment. An example comparing their theoretical and experimental EXAFS spectra is shown in Figure 13a along with their Fourier transforms in Figure 13b. Notably, the theoretical models with best fit were slightly more Au rich than those in the nominal compositions. In this manner, Frenkel et al. improved their PdAu NP models so that the interatomic distances were accurately reflected in their EXAFS data and the match with experimental EXAFS was excellent. This research highlights the utility of computational spectroscopy for identifying precise atomic structures that are difficult to resolve experimentally.

Machine learning (ML) techniques have been used together with computational spectroscopy to help resolve catalyst structure. For example, Frenkel et al.[229] used computational XANES and neural networks (NN) for refining the 3D geometry of Pt nanoparticles. They used FEFF and FDMNES to calculate theoretical XANES spectra of many NP structures as input for the NN. A ML model was then trained to predict structures from spectroscopic data alone. In this manner, the authors utilized theoretical XANES to build a data set to train a NN model that can directly predict catalyst structure from XANES data. This approach allows one to solve the structure from its experimental XANES, as demonstrated by reconstructing the average size, shape, and morphology of well-defined Pt nanoparticles. It also allows on-the-fly XANES analysis and is a promising approach for high-throughput and time-dependent studies.

As an example of calculation of vibrational spectroscopy data using the velocity autocorrelation function (VACF), we summarize the recent findings from Li et al.[113] The authors combine AIMD simulation and in situ surface-enhanced infrared adsorption spectroscopy (SEIRAS) to elucidate the origin of the sluggish HER kinetics in alkaline conditions using Pt-based catalysts. Here, the theoretical vibrational density of states (VDOS) (i.e., phonon modes) was computed by taking the Fourier transform of the velocity autocorrelation functions of the AIMD trajectories. Comparing the experimental (Figure 13c) and computed vibrational spectra (Figure 13d) allowed the authors to deconvolute and assign O−H stretching peaks corresponding to different regions in the electrical double layer. The match between the computational and experimental spectra indicates that the structures obtained from the AIMD simulations are realistic. The AIMD simulations show that there are "gaps" in the hydrogen bond network under alkaline conditions, which reduces the connectivity of H bond networks in the EDL and thus lowers the HER rate by slowing the rate of hydrogen transfer through the electrolyte. Although not obvious visually due to the different scale bars used in Figure 13c and 13d, we note that theory-predicted peaks are significantly broader than the experimental measurements; these inconsistencies could arise due to the simplicity of the computation model and/or time scales of the simulation.

### 3.5. Electrocatalyst Stability

The stability of an electrocatalyst is equally as critical to evaluating its performance as its activity and selectivity. Stability is greatly influenced by operating conditions, which include the pH and electrode potential for heterogeneous electrocatalysis. Pourbaix diagrams, which are phase diagrams with varying pH and potential (instead of temperature and pressure), depict the thermodynamic profile of an aqueous electrochemical system.[230] Pressure and temperature are typically held constant at standard conditions for these diagrams.

To compute the Pourbaix diagram, one first needs to identify the possible species in the electrochemical system and their reaction relations. Here, we demonstrate the calculation process using an Fe−N−C catalyst.[231] In addition to the solid catalyst, Fe can exist in the following dissolved species: $[Fe(H_2O)_m]^{2+}$, $[Fe(H_2O)_m]^{3+}$, $Fe(OH)_2$, $Fe(OH)_3$, and $FeO_4^{2-}$. The reaction energy for dissolving Fe from the catalyst into solution with 1 M concentration at a given pH and $U_{SHE}$ can be computed as

$$\Delta G = -E_{ad} - E_{coh} + ne(E^0 - U_{SHE}) - mk_bT\ln(10)\mathrm{pH}$$

where $E_{ad}$ is the adhesion energy of Fe in Fe−N−C, $E_{coh}$ is the cohesive energy of bulk Fe metal, $E^0$ is the standard electrode potential for the corresponding solvated species, $n$ is the number of electrons exchanged to form that species from bulk Fe, and $m$ is the number of protons exchanged. $E_{ad}$ is computable via DFT, whereas the other terms can be obtained from the experimental literature. Based on this equation, one can determine at what


https://doi.org/10.1021/acs.chemrev.3c00735
Chem. Rev. 2024, 124, 8620−8656

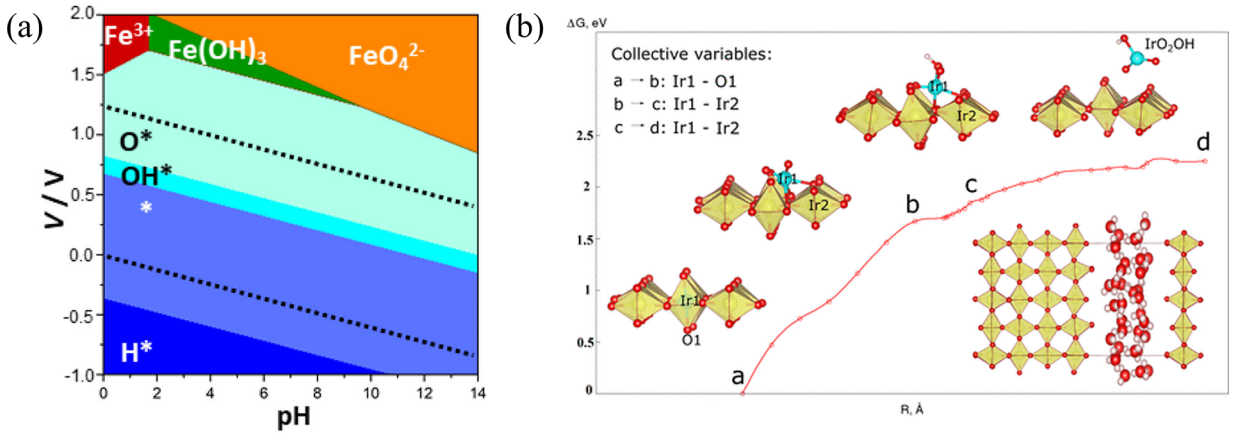


**Figure 14.** (a) Theoretical Pourbaix diagram of Fe−N−C. Adapted with permission from ref 231. Copyright 2024 American Chemical Society under [CC BY 4.0] [https://creativecommons.org/licenses/by/4.0/]. (b) Free energy profile of Ir dissolution from $IrO_2$(110). The insets along the profile depict metastable structures along the degradation pathway. The final state shows the fully dissolved $IrO_2H$ product. The inset in the lower right corner shows the simulation cell. Adapted with permission from ref 235. Copyright 2020 American Chemical Society.

potentials and pHs $\Delta G$ is positive (meaning that the Fe prefers to stay in the catalyst) or negative (meaning that the Fe prefers to be dissolved). Moreover, the Fe in the catalyst can be covered by different adsorbates, and the thermodynamics of adsorption can be calculated using the CHE method as a function of potential and pH. These results are combined to build the Pourbaix diagram, as shown in Figure 14a. The typical reduction/oxidation adsorbates (*H, *OH, *O, and *OOH) on Fe−N−C are considered in this study. It is worth noting that Materials Project has calculated the Pourbaix diagrams for vast amounts of materials.[232−234]

While Pourbaix diagrams are useful for thermodynamic analysis, kinetics also play an important role in determining stability.[236] The approaches used for calculating reaction kinetics as discussed in section 2.3 can be applied to study degradation kinetics. As an example, Alexandrov et al. systematically studied the dissolution of $IrO_2$ during the OER.[235] Particularly, they modeled the dissolution of Ir first through slow growth to enact bond formation/breaking followed by blue-moon sampling to obtain more accurate activation barriers, as shown in Figure 14b. They examined multiple different collective variables during dissolution to ensure the resulting intermediates adhered to the most thermodynamically favorable pathway. Although such types of studies that directly compute the degradation barriers are rare due to the high computational cost, they deserve more efforts to better understand and improve catalyst stability. It is also worth noting that degradation pathways can be varied and complex, which presents another challenge. Taking Fe−N−C for the ORR as an example, in addition to direct etching of the Fe atom, C atoms near Fe can also be corroded. As an example of a computational study for this degradation mechanism, Greeley et al.[237] recently calculated the potential where neighboring C is attacked (forming *O or *OH on the C) and used it to assess the stability for a variety of Fe−N−C structures. Therefore, it is necessary to thoroughly investigate degradation pathways to more effectively assess the catalyst stability. Finally, we note that some catalysts (e.g., subnanoclusters) are fluxional and isomerize much faster than the catalyzed reaction. In this case, simulations must consider the thermal ensemble of isomers, not just the ground state.[238,239]

## 4. EXPERIMENTAL PERSPECTIVES

While this review focuses on the use of quantum-chemical calculations to understand and optimize the production of renewable hydrogen, it is important to consider how experimental measurements can be most effectively carried out to validate and inform these theoretical models.

### 4.1. Experimental Protocols

For comparison with computational studies, it is critical to establish effective experimental protocols for measuring electrocatalytic activity and to use control tests to validate these protocols. The first variable that experimental protocols should aim to control is the influence of unwanted impurities. Impurities can arise from various sources, including electrolyte salts, electrode polishing slurries, the electrochemical cell, and reference and counter electrodes. To minimize the influence of impurities, it is first critical to thoroughly clean all electrochemical cells and components that contact the electrolyte, such as stir bars and rotation disk sheaths, prior to use. The cleaning procedure generally involves oxidizing organic impurities, dissolving trace metals in strong acid, and thorough rinsing in deionized water to remove any dissolved species. A sample procedure is provided.[240]

(1) Soak the cell and components in 0.5 M $H_2SO_4$ solution containing 1 g/L $KMnO_4$ for at least 24 h.

(2) Soak the cell and components in piranha solution (1 M $H_2SO_4$ and 6% $H_2O_2$) for at least 30 min.

(3) Rinse the cell in deionized water three times and boil at least 5 times, refreshing the water between boiling steps.

Another important consideration is the electrode polishing procedure before use. Commonly used alumina slurries used for mechanical polishing can leave Al-containing residues on the electrode surface, which can influence the measured catalytic performance.[241] Diamond and silicon carbide polishes are more electrochemically inert and therefore recommended.[242] For testing hydrogen evolution reaction catalysts, the use of a Pt counter electrode is strongly discouraged.[243] Under oxidizing potentials, Pt can form soluble species that can be cathodically deposited on the working electrode and artificially inflate the performance of nonprecious metal catalysts or change the surface area of Pt-based materials. This is also a common issue for in situ spectroscopic measurements where Pt can not only


https://doi.org/10.1021/acs.chemrev.3c00735
Chem. Rev. 2024, 124, 8620−8656

corrupt activity measurements but also introduce spectroscopic artifacts once deposited onto the working electrode.[244] For alkaline conditions, etching of borosilicate glass cells can introduce impurities into the electrolyte which can be deposited onto the working electrode. Most notably, iron impurities introduced this way have been shown to dramatically affect the performance of OER catalysts.[245] Electrochemical testing for alkaline systems should be performed on corrosion-resistant polymer cells, such as PTFE, and rigorous electrolyte purification techniques should be used.[246] Postreaction characterization is also recommended to verify the absence of foreign species on the electrode surface, although impurities can have important catalytic consequences while escaping detection by analytical techniques.

Further, it is crucial to accurately report electrode potentials. While electrode potentials are typically measured against an experimentally convenient reference electrode, such as Ag/AgCl, $Hg/Hg_2SO_4$, Hg/HgO, etc., they are typically reported against the reversible hydrogen electrode (RHE) scale. In this conversion, care should be taken to explicitly measure the potential of the reference electrode rather than assuming it.[247] Additionally, standard laboratory pH meters are often only accurate at a range of pH values near neutral, which does not correspond to the extreme pH values where electrocatalysis tests are conducted. Therefore, a pH meter suitable for these pH values should be used, and the values should be checked against standard values.[248] Alternatively, the direct use of an RHE as a reference electrode is ideal, and these are available commercially or can be easily fabricated.[249]

The most effective way to validate an experimental protocol is to test the activity of a benchmark standard catalyst. Excellent sources of benchmark activity data have been previously reported for the HER/HOR and OER/ORR.[250−252] Reproducing known benchmark activity data for a standard catalyst gives a higher degree of confidence in data reported for a new catalyst formulation or for new testing conditions. The use of benchmark catalysts also allows for comparison across different laboratories and experiments, thereby improving the reliability and reproducibility of the results. Developing effective experimental protocols will help to ensure more accurate and reliable electrocatalytic measurements for comparison with computational studies.

### 4.2. Collection and Reporting of Catalytic Activity

Density functional theory calculations provide information on the energetics of reaction elementary steps, which can be used to determine the intrinsic rate of reaction through a rate expression. This intrinsic rate is most precisely described by the turnover frequency (TOF), which describes the number of product molecules generated per active site per unit time.[253] To determine the TOF, it is necessary to quantify the rate of formation of products experimentally, rather than assuming their value from the amount of charge passed during an electrochemical experiment. Additionally, in cases where the source of products is ambiguous, isotopic labeling can be used to confirm their source (e.g., $^{15}N_2$ labeling for electrochemical reduction of $N_2$ to $NH_3$ if the current density of producing $NH_3$ is small).[254,255]

To define a turnover frequency, it is also essential to quantify the number of catalytically active sites. Ideally, a molecule that binds specifically to the active sites of interest can be used to count their number. For some systems, well-established protocols are available.[250,256] These techniques typically measure the charge associated with desorption, also known as stripping, of the titrant from the catalyst surface. Underpotentially deposited hydrogen, copper, and carbon monoxide are commonly used titrants for Pt catalysts and can often provide reasonably consistent results.[256] However, not all reaction chemistries and catalytic materials have specific titrants available, and the nature of the active sites for many electrocatalysts is unknown. As an alternative, it is possible to normalize electrochemical rates of reaction by the electrochemically accessible surface area (ECSA), which can be quantified by measuring the capacitance of the electrode in a potential region where no Faradaic processes occur.[257] Experimentally, this involves measuring the current response of the electrode at various scan rates. The current and scan rate will be linearly related with a slope equal to the double-layer capacitance of the electrode. This capacitance can then be compared to that of a flat surface to obtain a relative surface area or roughness factor. Typically assumed values of the specific capacitance of flat surfaces are between 10 and 120 $\mu F/cm^2$. While this analysis has limitations that have been discussed elsewhere, we strongly believe that normalizing to the active surface area is better than not considering the surface area at all.[257,258]

To understand the intrinsic catalytic activity, it is also crucial to ensure that the rates of reaction are controlled by kinetics rather than mass or charge transport. Reaction rates are kinetically controlled when the rates of surface elementary processes are slow compared to diffusion of the reactants to and from the surface and transfer of electrons to and from the active sites. External mass transport limitations can be determined by varying mixing in the electrochemical cell, such as by changing the rotation rate of a rotating disk electrode. Varying the rotation rate changes the thickness of the stagnant boundary layer at the electrode surface and the maximum flux of reactants to the electrode surface by diffusion. If the reaction is kinetically controlled, varying the mixing should not impact the measured rates. For the HER and OER, external mass transport is usually rapid enough to have limited impact on the measured rates, except for exceptionally active catalysts (such as Pt for the HER in acid).[205] Internal mass transport limitations or charge transport limitations are more common and can be assessed by varying the catalyst loading on the electrode surface.[259] Under kinetic control, specific activities or TOFs should be independent of catalyst loading. Dilution of active sites in conductive but inert carbon support is a useful way to demonstrate the absence of transport limitations, similar to commonly employed Madon−Boudart tests in thermochemical catalysis.[259,260] Demonstrating the lack of mass or charge transport limitations is a crucial criterion for fundamental studies on electrocatalysts to understand their intrinsic behavior. We hope that tests for transport limitations become more commonly practiced in the future.

### 4.3. Understanding the Nature of Electrocatalytic Active Sites

Density functional theory (DFT) calculations have become an essential tool for understanding the mechanism of catalytic reactions.[261,262] To perform a DFT calculation, a model of the active site is required. This decision is nontrivial even when considering simple metal catalysts, which present many possible active sites and surface terminations. The number of possible active sites increases tremendously when more complex catalytic materials (e.g., bimetallics, sulfides, nitrides, and phosphides) are considered.[263] To help confine the number of plausible


https://doi.org/10.1021/acs.chemrev.3c00735
Chem. Rev. 2024, 124, 8620−8656

active site structures, detailed experimental characterization of the catalyst is needed.

While experimental characterization of the catalyst after air exposure and before catalytic testing is useful, it is important to note that the catalyst can change significantly upon exposure to electrochemical conditions. Electrochemical testing of catalysts often involves highly oxidizing or reducing conditions that can drastically alter the catalyst's chemical state. For instance, $CO_2$RR catalysts are often tested at applied potentials near −1 V vs RHE. These potentials are far negative of the potentials where oxides/hydroxides of commonly used $CO_2$RR catalysts are stable[264] (e.g., ∼1.4 V negative of the reduction potential of $Cu^+$ at pH 7). Thus, most $CO_2$RR catalysts will exist in a metallic state under the reaction conditions irrespective of their starting composition. Similarly, for the OER, the active phase of the catalyst will inevitably be some form of oxide or oxyhydroxide regardless of the starting material due to the extremely oxidizing conditions of the reaction.[265] Therefore, while research efforts have been aimed at understanding the activity of phosphides, nitrides, sulfides, and selenides, these materials are not present at the surface under OER conditions.[266] Even metal oxides can undergo significant restructuring and amorphization under OER conditions.[267] Catalysts can also corrode or dissolve under the corrosive conditions of the OER, particularly in acid.[268] It should not be assumed that this does not occur on the basis of stable electrochemical performance. Catalysts can undergo significant structural changes that are not accompanied by decreases in activity. In fact, dissolution or amorphization is often accompanied by roughening and increases in electrochemically accessible surface area, resulting in increased current densities.[268]

Even stable electrocatalysts may degrade when exposed to open-circuit conditions upon introduction into the electrochemical cell.[269] For example, metal phosphides that are active for the HER oxidize at mildly oxidizing conditions, corrupting the measured performance and changing the nature of the active sites involved.[270] Techniques that limit these structural transformations, such as the use of potential protection, should therefore be given more consideration. Furthermore, it is critical to study the structure and composition of the catalyst under operating conditions to gain a comprehensive understanding of its performance. Spectroscopic techniques that use probes compatible with liquid electrolytes such as Raman and hard X-ray absorption/emission could provide such information. Additionally, characterization of the electrolyte using inductively coupled plasma (ICP) can be performed to look for evidence of corrosion or dissolution of the catalyst in operando conditions.[268]

### 4.4. Experimental Measurements for Comparison with Computational Studies

As we have discussed, it is crucial to produce reliable and accurate reactivity data that is validated against benchmark standards, normalized by the number of sites, and free from corruption due to impurities or mass/charge transport limitations. Once reliable experimental protocols are established, more detailed measurements can be done to enhance the connection between computation and experiment.[271] As we have mentioned, commonly employed Tafel analysis has limitations for multielectron transfer reactions and thus should be employed cautiously. Cardinal values of Tafel slopes carry implicit assumptions of adsorbate coverage, and multiple rate-limiting steps may be compatible with a single value. For instance, a Tafel slope of 120 mV/dec is consistent with both a Volmer step at zero coverage and a Heyrovsky step at full coverage for the HER.[216] Furthermore, coverages may change with potential, leading to changes in the Tafel slope.[272] Extraction of Tafel slopes from experimental data may even be biased depending on the voltage window chosen. Thus, measured slopes should not be overinterpreted.[273]

Kinetic analysis that is commonly employed in thermochemical catalysis is seldom carried out in electrocatalysis research and could yield a wealth of mechanistic information. Temperature-dependent measurements can be carried out to extract activation enthalpies and entropies. These studies should account for potential changes in the equilibrium potential of the reference electrode used with temperature. It is also important to note that these apparent barriers may encompass both kinetic activation energies and thermodynamic adsorption energies, so care should be taken when interpreting their physical significance. Once true kinetic activation energies are extracted, these can be compared with those obtained from DFT calculations. Experimental measurements of changing the reactant, product concentrations, or partial pressures can also be used to extract reaction orders which can help differentiate between competing mechanisms. A microkinetic model can provide expected orders of reaction under different adsorbate coverages. Kinetic tests utilizing isotopically labeled molecules can provide useful mechanistic insights. Isotope exchange rate measurements can evaluate the reversibility of chemical steps, while kinetic isotope effect measurements can gauge the kinetic significance of a specific reaction step.

In addition to their value for understanding the structure and composition of the catalyst, operando spectroscopy can be leveraged to inform kinetic measurements and computational studies.[274] Spectroscopic measurements can be used to look for evidence of certain reaction intermediates and to monitor changes in their coverage (with potential, reactant concentration, temperature, etc.). Spectroscopy can also be a useful tool for understanding the structure of the medium surrounding the catalyst as it can have an important influence on the reactivity in electrocatalytic systems.[176−178,275−279]

We suggest that more fundamental kinetic studies should be carried out on well-defined catalytic structures such as single-crystalline metallic or oxide substrates.[200] For instance, a limited number of single-crystal or oriented thin film studies have been done on the most highly active $IrO_2$ and $RuO_2$ catalysts for the OER, and even fewer report activation energies or other kinetic tests that could be compared to computational models.[280−284] For nonsingle-crystalline materials, studies on less complex catalyst formulations, such as low surface area polycrystalline thin films, would still be of significant value. High-fidelity experiments on well-defined materials could facilitate the development of activity trends among a large class of materials and serve as a reliable database for testing and validating computational work. With more complete experiments, more effective comparisons can be made with detailed calculations that seek to describe the entire energetic landscape of electrocatalytic reactions rather than the thermodynamics or kinetics of single elementary steps.

## 5. OUTLOOK

The field of computational heterogeneous electrocatalysis has steadily advanced in recent years. As shown above, there exist various models providing a diverse range of balances between accuracy and computational efficiency that enable future studies



https://doi.org/10.1021/acs.chemrev.3c00735
Chem. Rev. 2024, 124, 8620−8656

to select the techniques that are best suited to their investigation. However, even the simplest systems present enormous complexity as models are made progressively more realistic. These challenges have largely prevented the community from reaching clear consensus about even the most fundamental catalytic properties.

As perhaps true for any computational field, it is always desirable to make the methods more accurate and more efficient. In the following, we will present our perspectives on how to improve the accuracy and efficiency of computational heterogenous electrocatalysis models.

DFT has been the main workhorse for electronic structure calculations thanks to its balanced compromise between accuracy and speed. However, approximate exchange−correlation functionals limit DFT's accuracy, and different functionals can give vastly different results in some cases. Many-electron wave function methods have been developed for more accurate treatment of electronic exchange and correlation, although at greater computational cost than DFT. To bridge this gap, a promising solution is quantum embedding methods.[285] For example, in density functional embedding theory (DFET),[286] the system is divided into a cluster of atoms that requires more accurate treatment and a surrounding environment that may be periodic. The interaction between these regions is described by an embedding potential, which is chosen such that the sum of the electron densities of the cluster and the environment reproduces the total electron density. This embedding potential is then used as an external potential in higher level (e.g., wave function methods) calculations for the embedded cluster. The total energy can be obtained as[286]

$$E_{\text{tot}} = E_{\text{tot}}^{\text{DFT}} + (E_{\text{emb,cluster}}^{\text{CW}} - E_{\text{emb,cluster}}^{\text{DFT}})$$

where $E_{\text{tot}}^{\text{DFT}}$ is the DFT energy of the full system, $E_{\text{emb,cluster}}^{\text{CW}}$ is the energy of the cluster treated with the correlated-wave function method, and $E_{\text{emb,cluster}}^{\text{DFT}}$ is the DFT energy of the same cluster. The terms in parentheses thus account for the exchange−correlation energy of the electrons in the cluster, which is not accounted for properly by DFT. Quantum embedding methods have been used in a few papers to study electrocatalytic reactions.[287−291] However, these methods are still limited to relatively small scales that struggle to capture other complexities (e.g., solvent dynamics) at electrochemical interfaces. At the very least, these methods can provide a benchmark to evaluate the performance of different DFT functionals.

In parallel to developing more accurate methods beyond DFT, it is equally important to develop more efficient methods that enable large-scale simulations with accuracy comparable to DFT. To reduce computational cost, force fields (FF) can be developed to replace ab initio methods for force calculations. The conventional approach to create a FF is to manually construct a functional describing the interactions between atoms, which is quite difficult for complex systems. Machine learning (ML) has recently emerged as an easier and generalizable approach to create FFs.[292] ML FFs typically decompose the total energy of a system into the sum of atomic energies, which are determined by the local environment of each atom through a learnable functional form. The forces are then obtained as the negative gradients of the total energy with respect to the atomic positions. Particularly, with on-the-fly learning,[293−295] one can update the ML FF using new structures encountered during MD that are significantly different from those in the training set, thereby maintaining the accuracy of the FF.

Some recent studies have applied ML FFs to accelerate MD simulations of solid−liquid interfaces.[36,296,297] For example, Behler et al.[36] studied the copper−water interface for various copper facets using a ML neural network (NN) potential that was trained with DFT AIMD calculations. The supercells for their ML FF calculations contained approximately 2200−2800 atoms (depending on the facet) and were simulated for a full nanosecond. The increased system size and simulation time scale enabled them to rigorously sample the solvent dynamics that are prohibitively expensive with AIMD and inaccurately modeled with classical FFs. It should be noted that the electrochemical interface often contains long-range interactions (particularly Coulombic interactions), which are challenging to describe with conventional short-range FFs. Recent efforts to address this challenge can be found in the literature.[298,299] We emphasize that ML FFs must be trained on accurate data. This requires careful choice of the model for simulation as well as awareness of the limitations of the underlying quantum-mechanical method.

It is also worth pointing out that most existing computational studies aiming to understand and assess catalyst performance are based on thermodynamics. However, the catalytic performance is ultimately determined by the reaction rate. Thus, kinetics plays a more definitive role in understanding and assessing catalysts. More efforts should be spent to study reaction kinetics. Constant-potential AIMD simulations with hybrid solvation offer a promising approach to study reaction kinetics.[45,61] Also, as mentioned in section 3.5, catalyst stability (particularly the kinetics of degradation) deserves more attention as it is equally important to catalyst performance as catalyst activity and selectivity.

Similarly, in computational spectroscopy, first-principles methods are accurate but suffer from high computational cost and the extensive expertise required to design these simulations. These challenges create roadblocks for electrocatalysis applications, particularly for high-throughput analysis that needs to sample a large materials space, and for real time spectral interpretation that is essential for autonomous experimentation. A promising route to address these challenges is to develop data-driven spectral analysis approaches that combine physics-based methods with data analytics tools. Here, we summarize the key research areas in data-driven spectral analysis. (1) Benchmarking is an important step to quantify the effects of key approximations and implementations in different computational spectroscopy methods/codes, validate theory against experiment, and identify areas of method development to improve predictive power. Despite well-established efforts in the ground state DFT field,[300] similar work is scarce in the X-ray spectroscopy field.[127] (2) Due to the complexity in preparing spectral simulations, it is important to standardize input file generation for high-throughput simulations. The development of effective workflows would enable beginners to perform calculations by providing default input parameters and suggestions based on systematic benchmarks. These workflows would also ensure the reproducibility and interoperability of simulation data sets. There are existing tools in public databases, such as pymatgen in Materials Project,[301] and several spectral workflow codes that have been developed, such as Corvus[302] and Lightshow.[303] (3) Diverse data sets are needed for extracting structure-spectrum relationships from a wide chemical and conformational space. These data sets are essential


https://doi.org/10.1021/acs.chemrev.3c00735
Chem. Rev. 2024, 124, 8620−8656

for providing training sets for ML surrogates. There are several XAS databases available for materials[304−307] and molecules.[308] (4) Similar to the concept of ML FFs, ML models can be trained to predict XAS spectra from atomic structure models, such as the forward model.[308−312] Leveraging a spectral database constructed from first-principles simulations, the trained ML model can make predictions in fractions of a second and bypass computationally intensive simulations. In the opposite direction, supervised or unsupervised ML models can be trained to extract key physical descriptors (such as charge state, coordination number, and local symmetry) from XAS spectra to solve the inverse problem.[229,304,310,313−319] As generative AI like ChatGPT and Bard are having a big impact in our society, researchers are starting to explore applications of generative AI for developing interpretable ML models to disentangle abstract structure−spectrum relationships.[320]

In summary, novel computational techniques have improved understanding and prediction within the field of heterogeneous electrocatalysis. However, fundamental disagreements are common throughout the community, even for simple systems such as the HER on Pt(111). Difficulties in experimental measurements hinder the unambiguous evaluation of these models with different strengths and limitations. The electrocatalysis community may benefit from the thermocatalysis community in learning how they address similar problems. It is our hope that this review will spark more interest, efforts, and collaborations aimed at developing methods and benchmarking them over model systems.

## AUTHOR INFORMATION


### Corresponding Authors

**Ambarish Kulkarni** − *Department of Chemical Engineering, University of California, Davis, California 95616, United States;* orcid.org/0000-0001-9834-8264; Email: arkulkarni@ucdavis.edu

**Joaquin Resasco** − *Department of Chemical Engineering, The University of Texas at Austin, Austin, Texas 78712, United States;* orcid.org/0000-0001-6374-9877; Email: resasco@utexas.edu

**Deyu Lu** − *Center for Functional Nanomaterials, Brookhaven National Laboratory, Upton, New York 11973, United States;* orcid.org/0000-0003-4351-6085; Email: dlu@bnl.gov

**Jun Cheng** − *State Key Laboratory of Physical Chemistry of Solid Surfaces, iChEM, College of Chemistry and Chemical Engineering, Xiamen University, Xiamen 361005, China; Laboratory of AI for Electrochemistry (AI4EC), Tan Kah Kee Innovation Laboratory, Xiamen 361005, China;* orcid.org/0000-0001-6971-0797; Email: chengjun@xmu.edu.cn

**Yuanyue Liu** − *Texas Materials Institute and Department of Mechanical Engineering, The University of Texas at Austin, Austin, Texas 78712, United States;* orcid.org/0000-0002-5880-8649; Email: Yuanyue.liu@austin.utexas.edu

### Authors

**Zachary Levell** − *Texas Materials Institute and Department of Mechanical Engineering, The University of Texas at Austin, Austin, Texas 78712, United States*

**Jiabo Le** − *Ningbo Institute of Materials Technology and Engineering, Chinese Academy of Sciences, Ningbo 315201, China;* orcid.org/0000-0002-6570-5912

**Saerom Yu** − *Texas Materials Institute and Department of Mechanical Engineering, The University of Texas at Austin, Austin, Texas 78712, United States*

**Ruoyu Wang** − *Texas Materials Institute and Department of Mechanical Engineering, The University of Texas at Austin, Austin, Texas 78712, United States*

**Sudheesh Ethirajan** − *Department of Chemical Engineering, University of California, Davis, California 95616, United States;* orcid.org/0000-0002-8144-2657

**Rachita Rana** − *Department of Chemical Engineering, University of California, Davis, California 95616, United States;* orcid.org/0000-0002-5812-9312

Complete contact information is available at: https://pubs.acs.org/10.1021/acs.chemrev.3c00735


### Author Contributions

[§]Z.L. and J.L.: These authors contributed equally.

### Notes

The authors declare no competing financial interest.

### Biographies

Zachary Levell graduated from the University of Illinois at Urbana−Champaign with his B.S. degree in Materials Science and Engineering in 2020. He is currently a Ph.D. candidate in the Materials Science program at the University of Texas at Austin. His research is focused on studying heterogeneous electrocatalysis with first-principles methods.

Jia-Bo Le earned his Ph.D. degree from the University of Aberdeen in 2017 under the guidance of Jun Cheng. He then joined Xiamen University as a postdoctoral researcher from 2018 to 2020. Currently, he is an associate professor at the Ningbo Institute of Materials Technology and Engineering, Chinese Academy of Sciences. His research focuses on developing methods for modeling the electric double layer and elucidating the mechanisms of electrocatalytic reactions.

Saerom Yu is a Ph.D. candidate in Materials Science and Engineering at the University of Texas at Austin. She obtained her B.S. degree in Chemical Engineering from Soongsil University, South Korea and her M.S. degree in Energy from Texas A&M University. She worked as a research intern at the Center for Hydrogen and Fuel Cell Research, Korea Institute of Science and Technology. Her research focuses on understanding electrochemical processes at solid−liquid interfaces from first principles.

Ruoyu Wang earned his Bachelor's degree in Physics from Southern University of Science and Technology (SUSTech) in 2020. He is currently pursuing his Ph.D. degree in the Materials Science and Engineering program at the University of Texas at Austin.

Sudheesh Kumar Ethirajan is a Ph.D. candidate at the University of California, Davis, studying various physicochemical processes in MOFs at the quantum scale. His research combines machine learning, density functional theory, and rare-event sampling methods to capture atomic events over extended time scales. He earned his M.S. degree in Chemical Engineering from Carnegie Mellon University in 2020.

Rachita Rana is a postdoctoral associate at the Massachusetts Institute of Technology. She earned her Ph.D. degree from the University of California, Davis in 2023. With background in both computational and experimental catalysis, her research spans from atomically dispersed catalysts to nano- and mesoporous catalysts. Her current work is focused on investigating the promotional effects of electric fields on catalytic reactions.



https://doi.org/10.1021/acs.chemrev.3c00735
Chem. Rev. 2024, 124, 8620−8656

Ambarish Kulkarni is an associate professor in the Chemical Engineering Department at the University of California, Davis. He received his Ph.D. degree from the Georgia Institute of Technology in 2014 followed by a postdoctoral fellowship at Stanford University. Since 2018, his group has been using multiscale molecular modeling and machine learning tools to elucidate reaction mechanisms, interpret experimentally measured spectra, and accelerate the design of novel materials.

Joaquin Resasco is an assistant professor of Chemical Engineering at the University of Texas at Austin. A native of Argentina, he earned his B.S. degree in Chemical Engineering at the University of Oklahoma and his Ph.D. degree in Chemical Engineering at the University of California, Berkeley under the guidance of Alex Bell. Following his Ph.D. studies, he was a postdoctoral scholar with Phil Christopher at the University of California, Santa Barbara. Since starting at the University of Texas in 2021, his work has received a number of recognitions including the NSF CAREER Award, the SHPE Young Investigator Award, AIChE's 35 under 35, the ACS PRF New Investigator Award, the ACS Materials Au Rising Star in Materials Science, and Forbes 30 under 30.

Deyu Lu is a scientist at the Center for Functional Nanomaterials, Brookhaven National Laboratory, United States. He obtained his Ph.D. degree from the University of Illinois at Urbana−Champaign in 2005. His research interest is to develop and apply first-principle methods to understand fundamental physical properties of materials. Current research topics include computational X-ray spectroscopy and understanding the structure−property relationship of materials using machine learning methods.

Jun Cheng received his Ph.D. degree in Theoretical Chemistry from the Queen's University Belfast in 2008. He spent 5 years at the University of Cambridge as a postdoctoral fellow in the theory sector in chemistry and a junior research fellow at Emmanuel College. He is currently a professor at the College of Chemistry and Chemical Engineering, Xiamen University. His research interests are computational electrochemistry and theoretical catalysis. In particular, his group focuses on developing computational methods combining electronic structure theory, machine learning potential, and molecular dynamics to simulate electrochemical interfaces and catalyst dynamics. He is an Associate Editor of *The Journal of Chemical Physics* and has received the Alexander Kuznetsov Prize for Theoretical Electrochemistry of the International Society of Electrochemistry.

Yuanyue Liu is an assistant professor at the Texas Materials Institute and Department of Mechanical Engineering at the University of Texas at Austin. He is also affiliated with the Center for Electrochemistry and Oden Institute for Computational Engineering and Sciences. He received his B.S. degree from the University of Science and Technology of China (USTC) in 2008 and Ph.D. degree from Rice University in 2014, both in Materials Science. Then, he performed postdoctoral studies at the National Renewable Energy Laboratory (NREL) and California Institute of Technology before joining the University of Texas in Fall 2017. His research focuses on developing and applying computational methods to study energy and electronic materials and processes at the atomic level.

## ACKNOWLEDGMENTS

Z.L., S.Y., R.W., and Y.L. acknowledge the support by the NSF (2029442) and the Welch Foundation (F-1959). J.C. acknowledges funding from the National Science Fund for Distinguished Young Scholars (Grant No. 22225302), the National Natural Science Foundation of China (Grant Nos. 92161113, 21991151, 21991150, and 22021001), the Fundamental Research Funds for the Central Universities (Grant Nos. 20720220008, 20720220009, and 20720220010), the Laboratory of AI for Electrochemistry (AI4EC), and IKKEM (Grant Nos. RS2023100101 and RD2022070501). J.L. appreciates the financial support from the National Natural Science Foundation of China (Grant Nos. 22272193 and 21902136), the Yongjiang Talent Introduction Program (Grant No. 2021A-115-G), and the Ningbo Natural Science Foundation (Grant No. 2022J294). D.L. acknowledges the support from the U.S. Department of Energy, Office of Science, Office Basic Energy Sciences, under Award Number FWP PS-030. This research used theory and computation resources of the Center for Functional Nanomaterials (CFN), which is a U.S. Department of Energy Office of Science User Facility, at Brookhaven National Laboratory under Contract No. DE-SC0012704.

## REFERENCES

(1) Melander, M. M. Frozen or dynamic? — An atomistic simulation perspective on the timescales of electrochemical reactions. *Electrochim. Acta* **2023**, *446*, 142095.
(2) Zhao, X.; Levell, Z. H.; Yu, S.; Liu, Y. Atomistic Understanding of Two-dimensional Electrocatalysts from First Principles. *Chem. Rev.* **2022**, *122* (12), 10675−10709.
(3) Ringe, S.; Hörmann, N. G.; Oberhofer, H.; Reuter, K. Implicit Solvation Methods for Catalysis at Electrified Interfaces. *Chem. Rev.* **2022**, *122* (12), 10777−10820.
(4) Mathew, K.; Kolluru, V. S. C.; Mula, S.; Steinmann, S. N.; Hennig, R. G. Implicit self-consistent electrolyte model in plane-wave density-functional theory. *J. Chem. Phys.* **2019**, *151* (23), 234101.
(5) Mathew, K.; Sundararaman, R.; Letchworth-Weaver, K.; Arias, T. A.; Hennig, R. G. Implicit solvation model for density-functional study of nanocrystal surfaces and reaction pathways. *J. Chem. Phys.* **2014**, *140* (8), 084106.
(6) *VASPsol GitHub Page*; https://github.com/henniggroup/VASPsol (accessed 2024−03−12).
(7) Islam, S. M. R.; Khezeli, F.; Ringe, S.; Plaisance, C. An implicit electrolyte model for plane wave density functional theory exhibiting nonlinear response and a nonlocal cavity definition. *J. Chem. Phys.* **2023**, *159* (23), 234117.
(8) *VASPsol++ GitLab Page*. https://gitlab.com/cplaisance/vaspsol_pp (accessed 2024−03−12).
(9) Andreussi, O.; Dabo, I.; Marzari, N. Revised self-consistent continuum solvation in electronic-structure calculations. *J. Chem. Phys.* **2012**, *136* (6), 064102.
(10) Giannozzi, P.; Andreussi, O.; Brumme, T.; Bunau, O.; Buongiorno Nardelli, M.; Calandra, M.; Car, R.; Cavazzoni, C.; Ceresoli, D.; Cococcioni, M.; et al. Advanced capabilities for materials modelling with Quantum ESPRESSO. *J. Phys.: Condens. Matter* **2017**, *29* (46), 465901.
(11) *Environ. Download Website*. http://www.quantum-environ.org/ (accessed 2024−03−12).
(12) Otani, M.; Sugino, O. First-principles calculations of charged surfaces and interfaces: A plane-wave nonrepeated slab approach. *Phys. Rev. B* **2006**, *73* (11), 115407.
(13) Haruyama, J.; Ikeshoji, T.; Otani, M. Electrode potential from density functional theory calculations combined with implicit solvation theory. *Phys. Rev. Mater.* **2018**, *2* (9), 095801.
(14) Kastlunger, G.; Lindgren, P.; Peterson, A. A. Controlled-Potential Simulation of Elementary Electrochemical Reactions: Proton Discharge on Metal Surfaces. *J. Phys. Chem. C* **2018**, *122* (24), 12771−12781.
(15) Petrosyan, S. A.; Rigos, A. A.; Arias, T. A. Joint Density-Functional Theory: Ab Initio Study of Cr2O3 Surface Chemistry in Solution. *J. Phys. Chem. B* **2005**, *109* (32), 15436−15444.
(16) Letchworth-Weaver, K.; Arias, T. A. Joint density functional theory of the electrode-electrolyte interface: Application to fixed electrode potentials, interfacial capacitances, and potentials of zero charge. *Phys. Rev. B* **2012**, *86* (7), 075140.


https://doi.org/10.1021/acs.chemrev.3c00735
*Chem. Rev.* 2024, 124, 8620−8656

(17) Gunceler, D.; Letchworth-Weaver, K.; Sundararaman, R.; Schwarz, K. A.; Arias, T. A. The importance of nonlinear fluid response in joint density-functional theory studies of battery systems. *Modell. Simul. Mater. Sci. Eng.* **2013**, *21* (7), 074005.
(18) *GPAW Wiki*; https://wiki.fysik.dtu.dk/gpaw/index.html (accessed 2024−03−12).
(19) Sundararaman, R.; Letchworth-Weaver, K.; Schwarz, K. A.; Gunceler, D.; Ozhabes, Y.; Arias, T. A. JDFTx: Software for joint density-functional theory. *SoftwareX* **2017**, *6*, 278−284.
(20) *JDFTx Main Page*; https://jdftx.org/index.html (accessed 2024−03−12).
(21) Sundararaman, R.; Goddard, W. A., III The charge-asymmetric nonlocally determined local-electric (CANDLE) solvation model. *J. Chem. Phys.* **2015**, *142* (6), 064107.
(22) Abidi, N.; Steinmann, S. An Electrostatically Embedded QM/MM Scheme for Electrified Interfaces. *ChemRxiv*, **2023**; DOI: 10.26434/chemrxiv-2023-3t227
(23) Shin, S.-J.; Kim, D. H.; Bae, G.; Ringe, S.; Choi, H.; Lim, H.-K.; Choi, C. H.; Kim, H. On the importance of the electric double layer structure in aqueous electrocatalysis. *Nat. Commun.* **2022**, *13* (1), 174.
(24) Lim, H.-K.; Kwon, Y.; Kim, H. S.; Jeon, J.; Kim, Y.-H.; Lim, J.-A.; Kim, B.-S.; Choi, J.; Kim, H. Insight into the Microenvironments of the Metal-Ionic Liquid Interface during Electrochemical CO2 Reduction. *ACS Catal.* **2018**, *8* (3), 2420−2427.
(25) Pezeshki, S.; Lin, H. Recent developments in QM/MM methods towards open-boundary multi-scale simulations. *Mol. Simul.* **2015**, *41* (1−3), 168−189.
(26) Heenen, H. H.; Gauthier, J. A.; Kristoffersen, H. H.; Ludwig, T.; Chan, K. Solvation at metal/water interfaces: An ab initio molecular dynamics benchmark of common computational approaches. *J. Chem. Phys.* **2020**, *152* (14), 144703.
(27) Saboorian-Jooybari, H.; Chen, Z. Calculation of re-defined electrical double layer thickness in symmetrical electrolyte solutions. *Results in Physics* **2019**, *15*, 102501.
(28) Schmit, J. D.; Kariyawasam, N. L.; Needham, V.; Smith, P. E. SLTCAP: A Simple Method for Calculating the Number of Ions Needed for MD Simulation. *J. Chem. Theory Comput.* **2018**, *14* (4), 1823−1827.
(29) Machado, M. R.; Pantano, S. Split the Charge Difference in Two! A Rule of Thumb for Adding Proper Amounts of Ions in MD Simulations. *J. Chem. Theory Comput.* **2020**, *16* (3), 1367−1372.
(30) Le, J.-B.; Yang, X.-H.; Zhuang, Y.-B.; Jia, M.; Cheng, J. Recent Progress toward Ab Initio Modeling of Electrocatalysis. *J. Phys. Chem. Lett.* **2021**, *12* (37), 8924−8931.
(31) Levell, Z.; Liu, Y. Activation Energies of Heterogeneous Electrocatalysis: A Theoretical Perspective. *ACS Materials Au* **2024**, *4*, 129.
(32) Hörmann, N. G.; Guo, Z.; Ambrosio, F.; Andreussi, O.; Pasquarello, A.; Marzari, N. Absolute band alignment at semiconductor-water interfaces using explicit and implicit descriptions for liquid water. *npj Computational Materials* **2019**, *5* (1), 100.
(33) Pasumarthi, V.; Yu, H.; Akhade, S. A.; Abild-Pedersen, F.; Varley, J. B.; Bajdich, M. A Comparative Study of Electrical Double Layer Effects for CO Reduction Reaction Kinetics. *J. Phys. Chem. C* **2023**, *127* (34), 16850−16860.
(34) Zhao, H.; Lv, X.; Wang, Y.-G. Realistic Modeling of the Electrocatalytic Process at Complex Solid-Liquid Interface. *Advanced Science* **2023**, *10* (32), 2303677.
(35) Groß, A.; Sakong, S. Ab Initio Simulations of Water/Metal Interfaces. *Chem. Rev.* **2022**, *122* (12), 10746−10776.
(36) Natarajan, S. K.; Behler, J. Neural network molecular dynamics simulations of solid-liquid interfaces: water at low-index copper surfaces. *Phys. Chem. Chem. Phys.* **2016**, *18* (41), 28704−28725.
(37) Sakong, S.; Forster-Tonigold, K.; Groß, A. The structure of water at a Pt(111) electrode and the potential of zero charge studied from first principles. *J. Chem. Phys.* **2016**, *144* (19), 194701.
(38) Sakong, S.; Groß, A. The electric double layer at metal-water interfaces revisited based on a charge polarization scheme. *J. Chem. Phys.* **2018**, *149* (8), 084705.
(39) Dawson, W.; Gygi, F. Equilibration and analysis of first-principles molecular dynamics simulations of water. *J. Chem. Phys.* **2018**, *148* (12), 124501.
(40) Yu, L.; Pan, X.; Cao, X.; Hu, P.; Bao, X. Oxygen reduction reaction mechanism on nitrogen-doped graphene: A density functional theory study. *J. Catal.* **2011**, *282* (1), 183−190.
(41) Chen, A.; Le, J.-B.; Kuang, Y.; Cheng, J. Modeling stepped Pt/water interfaces at potential of zero charge with ab initio molecular dynamics. *J. Chem. Phys.* **2022**, *157* (9), 094702.
(42) Le, J.; Iannuzzi, M.; Cuesta, A.; Cheng, J. Determining Potentials of Zero Charge of Metal Electrodes versus the Standard Hydrogen Electrode from Density-Functional-Theory-Based Molecular Dynamics. *Phys. Rev. Lett.* **2017**, *119* (1), 016801.
(43) Nørskov, J. K.; Bligaard, T.; Logadottir, A.; Kitchin, J.; Chen, J. G.; Pandelov, S.; Stimming, U. Trends in the exchange current for hydrogen evolution. *J. Electrochem. Soc.* **2005**, *152* (3), J23.
(44) Taylor, C. D.; Wasileski, S. A.; Filhol, J.-S.; Neurock, M. First principles reaction modeling of the electrochemical interface: Consideration and calculation of a tunable surface potential from atomic and electronic structure. *Phys. Rev. B* **2006**, *73* (16), 165402.
(45) Yu, S.; Levell, Z.; Jiang, Z.; Zhao, X.; Liu, Y. What Is the Rate-Limiting Step of Oxygen Reduction Reaction on Fe-N-C Catalysts? *J. Am. Chem. Soc.* **2023**, *145* (46), 25352−25356.
(46) Skúlason, E.; Karlberg, G. S.; Rossmeisl, J.; Bligaard, T.; Greeley, J.; Jónsson, H.; Nørskov, J. K. Density functional theory calculations for the hydrogen evolution reaction in an electrochemical double layer on the Pt(111) electrode. *Phys. Chem. Chem. Phys.* **2007**, *9* (25), 3241−3250.
(47) The absolute electrode potential: an explanatory note (Recommendations 1986). *J. Electroanal. Chem. Interfacial Electrochem.* **1986**, *209* (2), 417−428. .
(48) Cheng, J.; Sprik, M. Aligning electronic energy levels at the TiO2/H2O interface. *Phys. Rev. B* **2010**, *82* (8), 081406.
(49) Cheng, J.; Sprik, M. Alignment of electronic energy levels at electrochemical interfaces. *Phys. Chem. Chem. Phys.* **2012**, *14* (32), 11245−11267.
(50) Cheng, J.; Liu, X.; VandeVondele, J.; Sulpizi, M.; Sprik, M. Redox Potentials and Acidity Constants from Density Functional Theory Based Molecular Dynamics. *Acc. Chem. Res.* **2014**, *47* (12), 3522−3529.
(51) Cheng, J.; VandeVondele, J. Calculation of Electrochemical Energy Levels in Water Using the Random Phase Approximation and a Double Hybrid Functional. *Phys. Rev. Lett.* **2016**, *116* (8), 086402.
(52) Cheng, J.; Sulpizi, M.; Sprik, M. Redox potentials and pKa for benzoquinone from density functional theory based molecular dynamics. *J. Chem. Phys.* **2009**, *131* (15), 154504.
(53) Costanzo, F.; Sulpizi, M.; Valle, R. G. D.; Sprik, M. The oxidation of tyrosine and tryptophan studied by a molecular dynamics normal hydrogen electrode. *J. Chem. Phys.* **2011**, *134* (24), 244508.
(54) Yang, X.-H.; Cuesta, A.; Cheng, J. Computational Ag/AgCl Reference Electrode from Density Functional Theory-Based Molecular Dynamics. *J. Phys. Chem. B* **2019**, *123* (48), 10224−10232.
(55) Wang, F.; Cheng, J. Automated workflow for computation of redox potentials, acidity constants, and solvation free energies accelerated by machine learning. *J. Chem. Phys.* **2022**, *157* (2), 024103.
(56) Rossmeisl, J.; Chan, K.; Ahmed, R.; Tripković, V.; Björketun, M. E. pH in atomic scale simulations of electrochemical interfaces. *Phys. Chem. Chem. Phys.* **2013**, *15* (25), 10321−10325.
(57) Kim, D.; Shi, J.; Liu, Y. Substantial impact of charge on electrochemical reactions of two-dimensional materials. *J. Am. Chem. Soc.* **2018**, *140* (29), 9127−9131.
(58) Plaisance, C. P.; van Santen, R. A. Structure Sensitivity of the Oxygen Evolution Reaction Catalyzed by Cobalt(II,III) Oxide. *J. Am. Chem. Soc.* **2015**, *137* (46), 14660−14672.
(59) Exner, K. S.; Anton, J.; Jacob, T.; Over, H. Full Kinetics from First Principles of the Chlorine Evolution Reaction over a RuO2(110) Model Electrode. *Angew. Chem., Int. Ed.* **2016**, *55* (26), 7501−7504.
(60) Exner, K. S. A Universal Descriptor for the Screening of Electrode Materials for Multiple-Electron Processes: Beyond the Thermodynamic Overpotential. *ACS Catal.* **2020**, *10* (21), 12607−12617.

(61) Zhao, X.; Liu, Y. Origin of Selective Production of Hydrogen Peroxide by Electrochemical Oxygen Reduction. *J. Am. Chem. Soc.* **2021**, *143* (25), 9423−9428.
(62) Henkelman, G.; Jónsson, H. Improved tangent estimate in the nudged elastic band method for finding minimum energy paths and saddle points. *J. Chem. Phys.* **2000**, *113* (22), 9978−9985.
(63) Sprik, M.; Ciccotti, G. Free energy from constrained molecular dynamics. *J. Chem. Phys.* **1998**, *109* (18), 7737−7744.
(64) Jarzynski, C. Nonequilibrium equality for free energy differences. *Phys. Rev. Lett.* **1997**, *78* (14), 2690.
(65) Ciccotti, G.; Ferrario, M. Blue moon approach to rare events. *Mol. Simul.* **2004**, *30* (11−12), 787−793.
(66) Kästner, J. Umbrella sampling. *Wiley Interdisciplinary Reviews: Computational Molecular Science* **2011**, *1* (6), 932−942.
(67) Bussi, G.; Laio, A. Using metadynamics to explore complex free-energy landscapes. *Nature Reviews Physics* **2020**, *2* (4), 200−212.
(68) Korpelin, V.; Kiljunen, T.; Melander, M. M.; Caro, M. A.; Kristoffersen, H. H.; Mammen, N.; Apaja, V.; Honkala, K. Addressing Dynamics at Catalytic Heterogeneous Interfaces with DFT-MD: Anomalous Temperature Distributions from Commonly Used Thermostats. *J. Phys. Chem. Lett.* **2022**, *13* (11), 2644−2652.
(69) Qin, X.; Vegge, T.; Hansen, H. A. Cation-coordinated inner-sphere CO2 electroreduction at Au-water interfaces. *J. Am. Chem. Soc.* **2023**, *145* (3), 1897−1905.
(70) Qin, X.; Hansen, H. A.; Honkala, K.; Melander, M. M. Cation-induced changes in the inner- and outer-sphere mechanisms of electrocatalytic CO2 reduction. *Nat. Commun.* **2023**, *14* (1), 7607.
(71) Gauthier, J. A.; Dickens, C. F.; Ringe, S.; Chan, K. Practical Considerations for Continuum Models Applied to Surface Electrochemistry. *ChemPhysChem* **2019**, *20* (22), 3074−3080.
(72) Bonnet, N.; Morishita, T.; Sugino, O.; Otani, M. First-Principles Molecular Dynamics at a Constant Electrode Potential. *Phys. Rev. Lett.* **2012**, *109* (26), 266101.
(73) Deißenbeck, F.; Freysoldt, C.; Todorova, M.; Neugebauer, J.; Wippermann, S. Dielectric Properties of Nanoconfined Water: A Canonical Thermopotentiostat Approach. *Phys. Rev. Lett.* **2021**, *126* (13), 136803.
(74) Surendralal, S.; Todorova, M.; Finnis, M. W.; Neugebauer, J. First-Principles Approach to Model Electrochemical Reactions: Understanding the Fundamental Mechanisms behind Mg Corrosion. *Phys. Rev. Lett.* **2018**, *120* (24), 246801.
(75) *Dr. Yuanyue Liu Research Group Home Page*; https://sites.utexas.edu/yuanyue-liu/ (accessed 2024−03−11).
(76) Xia, Z.; Xiao, H. Grand Canonical Ensemble Modeling of Electrochemical Interfaces Made Simple. *J. Chem. Theory Comput.* **2023**, *19* (15), 5168−5175.
(77) Sun, Y.; Silvioli, L.; Sahraie, N. R.; Ju, W.; Li, J.; Zitolo, A.; Li, S.; Bagger, A.; Arnarson, L.; Wang, X.; et al. Activity-selectivity trends in the electrochemical production of hydrogen peroxide over single-site metal-nitrogen-carbon catalysts. *J. Am. Chem. Soc.* **2019**, *141* (31), 12372−12381.
(78) Chen, X.; Kastlunger, G.; Peterson, A. A. Fundamental Drivers of Electrochemical Barriers. *Phys. Rev. Lett.* **2023**, *131* (23), 238003.
(79) Lindgren, P.; Kastlunger, G.; Peterson, A. A. Scaled and Dynamic Optimizations of Nudged Elastic Bands. *J. Chem. Theory Comput.* **2019**, *15* (11), 5787−5793.
(80) Ikeshoji, T.; Uchida, T.; Otani, M.; Osawa, M. First-principles molecular dynamics simulation for electrochemical hydrogen production by 4,4′-bipyridine molecular catalyst on silver electrode. *J. Electroanal. Chem.* **2017**, *800*, 13−18.
(81) Bouzid, A.; Pasquarello, A. Atomic-Scale Simulation of Electrochemical Processes at Electrode/Water Interfaces under Referenced Bias Potential. *J. Phys. Chem. Lett.* **2018**, *9* (8), 1880−1884.
(82) Bouzid, A.; Gono, P.; Pasquarello, A. Reaction pathway of oxygen evolution on Pt(1 1 1) revealed through constant Fermi level molecular dynamics. *J. Catal.* **2019**, *375*, 135−139.
(83) Beinlich, S. D.; Kastlunger, G.; Reuter, K.; Hörmann, N. G. Controlled Electrochemical Barrier Calculations without Potential Control. *J. Chem. Theory Comput.* **2023**, *19* (22), 8323−8331.
(84) Gauthier, J. A.; Dickens, C. F.; Heenen, H. H.; Vijay, S.; Ringe, S.; Chan, K. Unified Approach to Implicit and Explicit Solvent Simulations of Electrochemical Reaction Energetics. *J. Chem. Theory Comput.* **2019**, *15* (12), 6895−6906.
(85) M, V.; Singh, S.; Bononi, F.; Andreussi, O.; Karmodak, N. Thermodynamic and kinetic modeling of electrocatalytic reactions using a first-principles approach. *J. Chem. Phys.* **2023**, *159* (11), 111001.
(86) Warburton, R. E.; Soudackov, A. V.; Hammes-Schiffer, S. Theoretical Modeling of Electrochemical Proton-Coupled Electron Transfer. *Chem. Rev.* **2022**, *122* (12), 10599−10650.
(87) Hörmann, N. G.; Beinlich, S. D.; Reuter, K. Converging Divergent Paths: Constant Charge vs. Constant Potential Energetics in Computational Electrochemistry. *J. Phys. Chem. C* **2024**, *128*, 5524−5531.
(88) Rossmeisl, J.; Skúlason, E.; Björketun, M. E.; Tripkovic, V.; Nørskov, J. K. Modeling the electrified solid-liquid interface. *Chem. Phys. Lett.* **2008**, *466* (1−3), 68−71.
(89) Chan, K.; Nørskov, J. K. Potential dependence of electrochemical barriers from ab initio calculations. *journal of physical chemistry letters* **2016**, *7* (9), 1686−1690.
(90) Chan, K.; Nørskov, J. K. Electrochemical barriers made simple. *journal of physical chemistry letters* **2015**, *6* (14), 2663−2668.
(91) Hörmann, N. G.; Andreussi, O.; Marzari, N. Grand canonical simulations of electrochemical interfaces in implicit solvation models. *J. Chem. Phys.* **2019**, *150* (4), 041730.
(92) Andreussi, O.; Nattino, F.; Georg Hörmann, N. Continuum Embedding Models for Electrolyte Solutions in First-Principles Simulations of Electrochemistry. *Atomic-Scale Modelling of Electrochemical Systems* **2021**, 93−137.
(93) Beinlich, S. D.; Kastlunger, G.; Reuter, K.; Hörmann, N. G. A Theoretical Investigation of the Grand- and the Canonical Potential Energy Surface: The Interplay between Electronic and Geometric Response at Electrified Interfaces. *arXiv***2023**; DOI: 10.48550/arXiv.2307.09817.
(94) Hutchison, P.; Warburton, R. E.; Soudackov, A. V.; Hammes-Schiffer, S. Multicapacitor Approach to Interfacial Proton-Coupled Electron Transfer Thermodynamics at Constant Potential. *J. Phys. Chem. C* **2021**, *125* (40), 21891−21901.
(95) Agrawal, N.; Wong, A. J.-W.; Maheshwari, S.; Janik, M. J. An efficient approach to compartmentalize double layer effects on kinetics of interfacial proton-electron transfer reactions. *J. Catal.* **2024**, *430*, 115360.
(96) Strmcnik, D.; Uchimura, M.; Wang, C.; Subbaraman, R.; Danilovic, N.; van der Vliet, D.; Paulikas, A. P.; Stamenkovic, V. R.; Markovic, N. M. Improving the hydrogen oxidation reaction rate by promotion of hydroxyl adsorption. *Nat. Chem.* **2013**, *5* (4), 300−306.
(97) Govindarajan, N.; Xu, A.; Chan, K. How pH affects electrochemical processes. *Science* **2022**, *375* (6579), 379−380.
(98) Chan, K. A few basic concepts in electrochemical carbon dioxide reduction. *Nat. Commun.* **2020**, *11* (1), 5954.
(99) Liu, X.; Schlexer, P.; Xiao, J.; Ji, Y.; Wang, L.; Sandberg, R. B.; Tang, M.; Brown, K. S.; Peng, H.; Ringe, S.; et al. pH effects on the electrochemical reduction of CO(2) towards C2 products on stepped copper. *Nat. Commun.* **2019**, *10* (1), 32.
(100) Blizanac, B. B.; Lucas, C. A.; Gallagher, M. E.; Arenz, M.; Ross, P. N.; Marković, N. M. Anion Adsorption, CO Oxidation, and Oxygen Reduction Reaction on a Au(100) Surface: The pH Effect. *J. Phys. Chem. B* **2004**, *108* (2), 625−634.
(101) Luc, W.; Fu, X.; Shi, J.; Lv, J.-J.; Jouny, M.; Ko, B. H.; Xu, Y.; Tu, Q.; Hu, X.; Wu, J.; et al. Two-dimensional copper nanosheets for electrochemical reduction of carbon monoxide to acetate. *Nature Catalysis* **2019**, *2* (5), 423−430.
(102) Heenen, H. H.; Shin, H.; Kastlunger, G.; Overa, S.; Gauthier, J. A.; Jiao, F.; Chan, K. The mechanism for acetate formation in electrochemical CO(2) reduction on Cu: selectivity with potential, pH, and nanostructuring. *Energy Environ. Sci.* **2022**, *15* (9), 3978−3990.
(103) Goodpaster, J. D.; Bell, A. T.; Head-Gordon, M. Identification of Possible Pathways for C-C Bond Formation during Electrochemical

Reduction of CO2: New Theoretical Insights from an Improved Electrochemical Model. *J. Phys. Chem. Lett.* **2016**, *7* (8), 1471−1477.
(104) Gauthier, J. A.; Lin, Z.; Head-Gordon, M.; Bell, A. T. Pathways for the Formation of C2+ Products under Alkaline Conditions during the Electrochemical Reduction of CO2. *ACS Energy Lett.* **2022**, *7* (5), 1679−1686.
(105) Lamoureux, P. S.; Singh, A. R.; Chan, K. pH effects on hydrogen evolution and oxidation over Pt (111): insights from first-principles. *ACS Catal.* **2019**, *9* (7), 6194−6201.
(106) Resasco, J.; Abild-Pedersen, F.; Hahn, C.; Bao, Z.; Koper, M. T. M.; Jaramillo, T. F. Enhancing the connection between computation and experiments in electrocatalysis. *Nature Catalysis* **2022**, *5* (5), 374−381.
(107) Timoshenko, J. Spectroscopy predicts catalyst functionality. *Nature Catalysis* **2022**, *5*, 469−470.
(108) Stevens, M. B.; Kreider, M. E.; Patel, A. M.; Wang, Z.; Liu, Y.; Gibbons, B. M.; Statt, M. J.; Ievlev, A. V.; Sinclair, R.; Mehta, A.; et al. Identifying and Tuning the In Situ Oxygen-Rich Surface of Molybdenum Nitride Electrocatalysts for Oxygen Reduction. *ACS Appl. Energy Mater.* **2020**, *3* (12), 12433−12446.
(109) Trindell, J. A.; Duan, Z.; Henkelman, G.; Crooks, R. M. Well-Defined Nanoparticle Electrocatalysts for the Refinement of Theory. *Chem. Rev.* **2020**, *120* (2), 814−850.
(110) Wöhl, J.; Kopp, W. A.; Yevlakhovych, I.; Bahr, L.; Koß, H.-J.; Leonhard, K. Completely Computational Model Setup for Spectroscopic Techniques: The Ab Initio Molecular Dynamics Indirect Hard Modeling Approach. *J. Phys. Chem. A* **2022**, *126* (18), 2845−2853.
(111) Chen, M.; Liu, D.; Qiao, L.; Zhou, P.; Feng, J.; Ng, K. W.; Liu, Q.; Wang, S.; Pan, H. In-situ/operando Raman techniques for in-depth understanding on electrocatalysis. *Chem. Eng. J.* **2023**, *461*, 141939.
(112) Timoshenko, J.; Roldan Cuenya, B. In Situ/Operando Electrocatalyst Characterization by X-ray Absorption Spectroscopy. *Chem. Rev.* **2021**, *121* (2), 882−961.
(113) Li, P.; Jiang, Y.; Hu, Y.; Men, Y.; Liu, Y.; Cai, W.; Chen, S. Hydrogen bond network connectivity in the electric double layer dominates the kinetic pH effect in hydrogen electrocatalysis on Pt. *Nature Catalysis* **2022**, *5* (10), 900−911.
(114) Kosmala, T.; Baby, A.; Lunardon, M.; Perilli, D.; Liu, H.; Durante, C.; Di Valentin, C.; Agnoli, S.; Granozzi, G. Operando visualization of the hydrogen evolution reaction with atomic-scale precision at different metal-graphene interfaces. *Nature Catalysis* **2021**, *4* (10), 850−859.
(115) Steinmann, S. N.; Wei, Z.-Y.; Sautet, P. Theory and experiments join forces to characterize the electrocatalytic interface. *Proc. Natl. Acad. Sci. U. S. A.* **2019**, *116* (16), 7611−7613.
(116) Tong, Y. J. In situ electrochemical nuclear magnetic resonance spectroscopy for electrocatalysis: Challenges and prospects. *Current Opinion in Electrochemistry* **2017**, *4* (1), 60−68.
(117) Rehr, J. J.; Ankudinov, A. L. Progress in the theory and interpretation of XANES. *Coord. Chem. Rev.* **2005**, *249* (1), 131−140.
(118) Penner-Hahn, J. E. X-ray absorption spectroscopy. *Comprehensive Coordination Chemistry II* **2003**, *2*, 159−186.
(119) Borfecchia, E.; Garino, C.; Salassa, L.; Lamberti, C. Synchrotron ultrafast techniques for photoactive transition metal complexes. *Philosophical Transactions of the Royal Society A: Mathematical, Physical and Engineering Sciences* **2013**, *371* (1995), 20120132.
(120) Rehr, J. J.; Albers, R. C. Theoretical approaches to x-ray absorption fine structure. *Rev. Mod. Phys.* **2000**, *72* (3), 621−654.
(121) Timoshenko, J.; Shivhare, A.; Scott, R. W. J.; Lu, D.; Frenkel, A. I. Solving local structure around dopants in metal nanoparticles with ab initio modeling of X-ray absorption near edge structure. *Phys. Chem. Chem. Phys.* **2016**, *18* (29), 19621−19630.
(122) De Groot, F.; Kotani, A. *Core level spectroscopy of solids*; CRC Press, 2008.
(123) Rehr, J. J.; Albers, R. C. Theoretical approaches to x-ray absorption fine structure. *Reviews of modern physics* **2000**, *72* (3), 621.
(124) Casida, M. E. Time-dependent density functional response theory for molecules. In *Recent Advances In Density Functional Methods: (Part I)*; World Scientific, 1995; pp 155−192.
(125) Marques, M. A. L.; Maitra, N. T.; Nogueira, F. M. S.; Gross, E. K. U.; Rubio, A. *Fundamentals of time-dependent density functional theory*; Springer, 2012.
(126) Onida, G.; Reining, L.; Rubio, A. Electronic excitations: density-functional versus many-body Green's-function approaches. *Reviews of modern physics* **2002**, *74* (2), 601.
(127) Meng, F.; Maurer, B.; Peschel, F.; Selcuk, S.; Hybertsen, M.; Qu, X.; Vorwerk, C.; Draxl, C.; Vinson, J.; Lu, D. Multicode benchmark on simulated Ti K-edge x-ray absorption spectra of Ti-O compounds. *Phys. Rev. Mater.* **2024**, *8* (1), 013801.
(128) Hamann, D. R.; Muller, D. A. Absolute and approximate calculations of electron-energy-loss spectroscopy edge thresholds. *Physical review letters* **2002**, *89* (12), 126404.
(129) England, A. H.; Duffin, A. M.; Schwartz, C. P.; Uejio, J. S.; Prendergast, D.; Saykally, R. J. On the hydration and hydrolysis of carbon dioxide. *Chem. Phys. Lett.* **2011**, *514* (4−6), 187−195.
(130) Vinson, J. Advances in the ocean-3 spectroscopy package. *Phys. Chem. Chem. Phys.* **2022**, *24* (21), 12787−12803.
(131) Yao, Y.; Golze, D.; Rinke, P.; Blum, V.; Kanai, Y. All-electron BSE@ GW method for K-edge core electron excitation energies. *J. Chem. Theory Comput.* **2022**, *18* (3), 1569−1583.
(132) Liang, Y.; Vinson, J.; Pemmaraju, S.; Drisdell, W. S.; Shirley, E. L.; Prendergast, D. Accurate X-Ray Spectral Predictions: An Advanced Self-Consistent-Field Approach Inspired by Many-Body Perturbation Theory. *Phys. Rev. Lett.* **2017**, *118* (9), 096402.
(133) Carlin, R. L. Introduction to ligand field theory (Ballhausen. Carl J.). *J. Chem. Educ.* **1963**, *40*, 390.
(134) Haverkort, M. W.; Zwierzycki, M.; Andersen, O. K. Multiplet ligand-field theory using Wannier orbitals. *Phys. Rev. B* **2012**, *85* (16), 165113.
(135) Kas, J. J.; Vila, F. D.; Pemmaraju, C. D.; Tan, T. S.; Rehr, J. J. Advanced calculations of X-ray spectroscopies with FEFF10 and Corvus. *Journal of Synchrotron Radiation* **2021**, *28* (6), 1801−1810.
(136) Joly, Y.; Bunău, O.; Lorenzo, J.-E.; Galera, R.-M.; Grenier, S.; Thompson, B. Self-consistency, spin-orbit and other advances in the FDMNES code to simulate XANES and RXD experiments. *J. Phys.: Conf. Ser.* **2009**, *190*, 012007.
(137) Neese, F. The ORCA program system. *Wiley Interdisciplinary Reviews: Computational Molecular Science* **2012**, *2* (1), 73−78.
(138) Valiev, M.; Bylaska, E. J.; Govind, N.; Kowalski, K.; Straatsma, T. P.; Van Dam, H. J. J.; Wang, D.; Nieplocha, J.; Aprà, E.; Windus, T. L.; et al. NWChem: A comprehensive and scalable open-source solution for large scale molecular simulations. *Comput. Phys. Commun.* **2010**, *181* (9), 1477−1489.
(139) Vinson, J.; Rehr, J. J.; Kas, J. J.; Shirley, E. L. Bethe-Salpeter equation calculations of core excitation spectra. *Phys. Rev. B* **2011**, *83* (11), 115106.
(140) Gulans, A.; Kontur, S.; Meisenbichler, C.; Nabok, D.; Pavone, P.; Rigamonti, S.; Sagmeister, S.; Werner, U.; Draxl, C. exciting: a full-potential all-electron package implementing density-functional theory and many-body perturbation theory. *J. Phys.: Condens. Matter* **2014**, *26* (36), 363202.
(141) Taillefumier, M.; Cabaret, D.; Flank, A.-M.; Mauri, F. X-ray absorption near-edge structure calculations with the pseudopotentials: Application to the K edge in diamond and alpha-quartz. *Phys. Rev. B* **2002**, *66* (19), 195107.
(142) Karsai, F.; Humer, M.; Flage-Larsen, E.; Blaha, P.; Kresse, G. Effects of electron-phonon coupling on absorption spectrum: K edge of hexagonal boron nitride. *Phys. Rev. B* **2018**, *98* (23), 235205.
(143) Prendergast, D.; Galli, G. X-ray absorption spectra of water from first principles calculations. *Physical review letters* **2006**, *96* (21), 215502.
(144) Triguero, L.; Pettersson, L. G. M.; Ågren, H. Calculations of near-edge x-ray-absorption spectra of gas-phase and chemisorbed molecules by means of density-functional and transition-potential theory. *Phys. Rev. B* **1998**, *58* (12), 8097−8110.
(145) Haverkort, M. W. Quanty for core level spectroscopy-excitons, resonances and band excitations in time and frequency domain. *J. Phys.: Conf. Ser.* **2016**, *712*, 012001.


https://doi.org/10.1021/acs.chemrev.3c00735
*Chem. Rev.* 2024, 124, 8620−8656

(146) Stavitski, E.; de Groot, F. M. F. The CTM4XAS program for EELS and XAS spectral shape analysis of transition metal L edges. *Micron* **2010**, *41* (7), 687−694.
(147) Wang, Y. L.; Fabbris, G.; Dean, M. P. M.; Kotliar, G. EDRIXS: An open source toolkit for simulating spectra of resonant inelastic x-ray scattering. *Comput. Phys. Commun.* **2019**, *243*, 151−165.
(148) Deng, Y.; Dong, S.; Li, Z.; Jiang, H.; Zhang, X.; Ji, X. Applications of Conventional Vibrational Spectroscopic Methods for Batteries Beyond Li-Ion. *Small Methods* **2018**, *2* (8), 1700332.
(149) Xu, Z.; Liang, Z.; Guo, W.; Zou, R. In situ/operando vibrational spectroscopy for the investigation of advanced nanostructured electrocatalysts. *Coord. Chem. Rev.* **2021**, *436*, 213824.
(150) Shin, Y. K.; Gai, L.; Raman, S.; van Duin, A. C. T. Development of a ReaxFF Reactive Force Field for the Pt-Ni Alloy Catalyst. *J. Phys. Chem. A* **2016**, *120* (41), 8044−8055.
(151) Clabaut, P.; Fleurat-Lessard, P.; Michel, C.; Steinmann, S. N. Ten Facets, One Force Field: The GAL19 Force Field for Water-Noble Metal Interfaces. *J. Chem. Theory Comput.* **2020**, *16* (7), 4565−4578.
(152) Bramley, G.; Nguyen, M.-T.; Glezakou, V.-A.; Rousseau, R.; Skylaris, C.-K. Reconciling Work Functions and Adsorption Enthalpies for Implicit Solvent Models: A Pt (111)/Water Interface Case Study. *J. Chem. Theory Comput.* **2020**, *16* (4), 2703−2715.
(153) Li, P.; Huang, J.; Hu, Y.; Chen, S. Establishment of the Potential of Zero Charge of Metals in Aqueous Solutions: Different Faces of Water Revealed by Ab Initio Molecular Dynamics Simulations. *J. Phys. Chem. C* **2021**, *125*, 3972−3979.
(154) Fang, Y.-H.; Wei, G.-F.; Liu, Z.-P. Theoretical modeling of electrode/electrolyte interface from first-principles periodic continuum solvation method. *Catal. Today* **2013**, *202*, 98−104.
(155) Jinnouchi, R.; Anderson, A. B. Electronic structure calculations of liquid-solid interfaces: Combination of density functional theory and modified Poisson-Boltzmann theory. *Phys. Rev. B* **2008**, *77* (24), 245417.
(156) Rizo, R.; Sitta, E.; Herrero, E.; Climent, V.; Feliu, J. M. Towards the understanding of the interfacial pH scale at Pt(111) electrodes. *Electrochim. Acta* **2015**, *162*, 138−145.
(157) Xu, P.; von Rueden, A. D.; Schimmenti, R.; Mavrikakis, M.; Suntivich, J. Optical method for quantifying the potential of zero charge at the platinum-water electrochemical interface. *Nat. Mater.* **2023**, *22* (4), 503−510.
(158) Cuesta, A. Measurement of the surface charge density of CO-saturated Pt(111) electrodes as a function of potential: the potential of zero charge of Pt(111). *Surf. Sci.* **2004**, *572* (1), 11−22.
(159) Trasatti, S.; Lust, E. The Potential of Zero Charge. In *Modern Aspects of Electrochemistry*; White, R. E., Bockris, J. O. M., Conway, B. E., Eds.; Springer US, 1999; pp 1−215.
(160) Le, J.-B.; Cheng, J. Modeling electrochemical interfaces from ab initio molecular dynamics: water adsorption on metal surfaces at potential of zero charge. *Current Opinion in Electrochemistry* **2020**, *19*, 129−136.
(161) Schmickler, W.; Santos, E. The metal-solution interface. In *Interfacial Electrochemistry*; Schmickler, W., Santos, E., Eds.; Springer Berlin Heidelberg, 2010; pp 39−50.
(162) Li, X.-Y.; Chen, A.; Yang, X.-H.; Zhu, J.-X.; Le, J.-B.; Cheng, J. Linear Correlation between Water Adsorption Energies and Volta Potential Differences for Metal/water Interfaces. *J. Phys. Chem. Lett.* **2021**, *12* (30), 7299−7304.
(163) Le, J.; Cuesta, A.; Cheng, J. The structure of metal-water interface at the potential of zero charge from density functional theory-based molecular dynamics. *J. Electroanal. Chem.* **2018**, *819*, 87−94.
(164) Le, J.; Fan, Q.; Perez-Martinez, L.; Cuesta, A.; Cheng, J. Theoretical insight into the vibrational spectra of metal-water interfaces from density functional theory based molecular dynamics. *Phys. Chem. Chem. Phys.* **2018**, *20* (17), 11554−11558.
(165) Müller, J. E. Interaction of the Pt(111) surface with adsorbed Xe atoms. *Phys. Rev. Lett.* **1990**, *65* (24), 3021−3024.
(166) Khatib, R.; Kumar, A.; Sanvito, S.; Sulpizi, M.; Cucinotta, C. S. The nanoscale structure of the Pt-water double layer under bias revealed. *Electrochim. Acta* **2021**, *391*, 138875.
(167) Kelly, S. R.; Heenen, H. H.; Govindarajan, N.; Chan, K.; Nørskov, J. K. OH Binding Energy as a Universal Descriptor of the Potential of Zero Charge on Transition Metal Surfaces. *J. Phys. Chem. C* **2022**, *126* (12), 5521−5528.
(168) Ledezma-Yanez, I.; Wallace, W. D. Z.; Sebastián-Pascual, P.; Climent, V.; Feliu, J. M.; Koper, M. T. M. Interfacial water reorganization as a pH-dependent descriptor of the hydrogen evolution rate on platinum electrodes. *Nature Energy* **2017**, *2* (4), 17031.
(169) Li, C.-Y.; Le, J.-B.; Wang, Y.-H.; Chen, S.; Yang, Z.-L.; Li, J.-F.; Cheng, J.; Tian, Z.-Q. In situ probing electrified interfacial water structures at atomically flat surfaces. *Nat. Mater.* **2019**, *18* (7), 697−701.
(170) Monteiro, M. C. O.; Dattila, F.; Hagedoorn, B.; García-Muelas, R.; López, N.; Koper, M. T. M. Absence of CO2 electroreduction on copper, gold and silver electrodes without metal cations in solution. *Nature Catalysis* **2021**, *4* (8), 654−662.
(171) Huang, B.; Rao, R. R.; You, S.; Hpone Myint, K.; Song, Y.; Wang, Y.; Ding, W.; Giordano, L.; Zhang, Y.; Wang, T.; et al. Cation- and pH-Dependent Hydrogen Evolution and Oxidation Reaction Kinetics. *JACS Au* **2021**, *1* (10), 1674−1687.
(172) Velasco-Velez, J.-J.; Wu, C. H.; Pascal, T. A.; Wan, L. F.; Guo, J.; Prendergast, D.; Salmeron, M. The structure of interfacial water on gold electrodes studied by x-ray absorption spectroscopy. *Science* **2014**, *346* (6211), 831−834.
(173) Le, J.-B.; Fan, Q.-Y.; Li, J.-Q.; Cheng, J. Molecular origin of negative component of Helmholtz capacitance at electrified Pt(111)/water interface. *Sci. Adv.* **2020**, *6* (41), eabb1219.
(174) Li, L.; Liu, Y.-P.; Le, J.-B.; Cheng, J. Unraveling molecular structures and ion effects of electric double layers at metal water interfaces. *Cell Rep. Phys. Sci.* **2022**, *3* (2), 100759.
(175) Le, J.-B.; Chen, A.; Li, L.; Xiong, J.-F.; Lan, J.; Liu, Y.-P.; Iannuzzi, M.; Cheng, J. Modeling Electrified Pt(111)-Had/Water Interfaces from Ab Initio Molecular Dynamics. *JACS Au* **2021**, *1* (5), 569−577.
(176) Bender, J. T.; Petersen, A. S.; Østergaard, F. C.; Wood, M. A.; Heffernan, S. M. J.; Milliron, D. J.; Rossmeisl, J.; Resasco, J. Understanding Cation Effects on the Hydrogen Evolution Reaction. *ACS Energy Lett.* **2023**, *8* (1), 657−665.
(177) Ringe, S.; Clark, E. L.; Resasco, J.; Walton, A.; Seger, B.; Bell, A. T.; Chan, K. Understanding cation effects in electrochemical CO2 reduction. *Energy Environ. Sci.* **2019**, *12* (10), 3001−3014.
(178) Resasco, J.; Chen, L. D.; Clark, E.; Tsai, C.; Hahn, C.; Jaramillo, T. F.; Chan, K.; Bell, A. T. Promoter effects of alkali metal cations on the electrochemical reduction of carbon dioxide. *J. Am. Chem. Soc.* **2017**, *139* (32), 11277−11287.
(179) Dattila, F.; Monteiro, M. C. O.; Koper, M. T. M.; López, N. Reply to: On the role of metal cations in CO2 electrocatalytic reduction. *Nature Catalysis* **2022**, *5* (11), 979−981.
(180) Monteiro, M. C. O.; Dattila, F.; López, N.; Koper, M. T. M. The Role of Cation Acidity on the Competition between Hydrogen Evolution and CO2 Reduction on Gold Electrodes. *J. Am. Chem. Soc.* **2022**, *144* (4), 1589−1602.
(181) Marcandalli, G.; Monteiro, M. C. O.; Goyal, A.; Koper, M. T. M. Electrolyte Effects on CO2 Electrochemical Reduction to CO. *Acc. Chem. Res.* **2022**, *55* (14), 1900−1911.
(182) Liu, H.; Liu, J.; Yang, B. Promotional Role of a Cation Intermediate Complex in C2 Formation from Electrochemical Reduction of CO2 over Cu. *ACS Catal.* **2021**, *11* (19), 12336−12343.
(183) Chen, L. D.; Urushihara, M.; Chan, K.; Nørskov, J. K. Electric Field Effects in Electrochemical CO2 Reduction. *ACS Catal.* **2016**, *6* (10), 7133−7139.
(184) Li, J.; Li, X.; Gunathunge, C. M.; Waegele, M. M. Hydrogen bonding steers the product selectivity of electrocatalytic CO reduction. *Proc. Natl. Acad. Sci. U. S. A.* **2019**, *116* (19), 9220−9229.
(185) Zhan, C.; Cerón, M. R.; Hawks, S. A.; Otani, M.; Wood, B. C.; Pham, T. A.; Stadermann, M.; Campbell, P. G. Specific ion effects at graphitic interfaces. *Nat. Commun.* **2019**, *10* (1), 4858.


https://doi.org/10.1021/acs.chemrev.3c00735
*Chem. Rev.* 2024, 124, 8620−8656

(186) Janata, J. Physical Electrochemistry. Fundamentals, Techniques and Applications. By Eliezer Gileadi. *Angew. Chem., Int. Ed.* **2011**, *50* (41), 9538−9538.
(187) Pajkossy, T.; Kolb, D. M. Double layer capacitance of Pt(111) single crystal electrodes. *Electrochim. Acta* **2001**, *46* (20), 3063−3071.
(188) Pajkossy, T.; Wandlowski, T.; Kolb, D. M. Impedance aspects of anion adsorption on gold single crystal electrodes. *J. Electroanal. Chem.* **1996**, *414* (2), 209−220.
(189) Valette, G. Double layer on silver single crystal electrodes in contact with electrolytes having anions which are slightly specifically adsorbed: Part III. The (111) face. *Journal of Electroanalytical Chemistry and Interfacial Electrochemistry* **1989**, *269* (1), 191−203.
(190) Ando, Y.; Gohda, Y.; Tsuneyuki, S. Ab initio molecular dynamics study of the Helmholtz layer formed on solid-liquid interfaces and its capacitance. *Chem. Phys. Lett.* **2013**, *556*, 9−12.
(191) Li, X.-Y.; Jin, X.-F.; Yang, X.-H.; Wang, X.; Le, J.-B.; Cheng, J. Molecular understanding of the Helmholtz capacitance difference between Cu(100) and graphene electrodes. *J. Chem. Phys.* **2023**, *158* (8), 084701.
(192) Hussain, G.; Pérez-Martínez, L.; Le, J.-B.; Papasizza, M.; Cabello, G.; Cheng, J.; Cuesta, A. How cations determine the interfacial potential profile: Relevance for the CO2 reduction reaction. *Electrochim. Acta* **2019**, *327*, 135055.
(193) Yang, H.; Yang, J.; Bo, Z.; Chen, X.; Shuai, X.; Kong, J.; Yan, J.; Cen, K. Kinetic-Dominated Charging Mechanism within Representative Aqueous Electrolyte-based Electric Double-Layer Capacitors. *J. Phys. Chem. Lett.* **2017**, *8* (15), 3703−3710.
(194) Iamprasertkun, P.; Hirunpinyopas, W.; Keerthi, A.; Wang, B.; Radha, B.; Bissett, M. A.; Dryfe, R. A. W. Capacitance of Basal Plane and Edge-Oriented Highly Ordered Pyrolytic Graphite: Specific Ion Effects. *J. Phys. Chem. Lett.* **2019**, *10* (3), 617−623.
(195) Le, J.-B.; Chen, A.; Kuang, Y.; Cheng, J. Molecular understanding of cation effects on double layer and its significance to CO-CO dimerization. *Natl. Sci. Rev.* **2023**, *10*, nwad105.
(196) Bazant, M. Z.; Storey, B. D.; Kornyshev, A. A. Double Layer in Ionic Liquids: Overscreening versus Crowding. *Phys. Rev. Lett.* **2011**, *106* (4), 046102.
(197) Ovalle, V. J.; Hsu, Y.-S.; Agrawal, N.; Janik, M. J.; Waegele, M. M. Correlating hydration free energy and specific adsorption of alkali metal cations during CO2 electroreduction on Au. *Nature Catalysis* **2022**, *5* (7), 624−632.
(198) Conway, B.; Tilak, B. Interfacial processes involving electrocatalytic evolution and oxidation of H2, and the role of chemisorbed H. *Electrochimica acta* **2002**, *47* (22−23), 3571−3594.
(199) Marković, N.; Grgur, B.; Ross, P. N. Temperature-dependent hydrogen electrochemistry on platinum low-index single-crystal surfaces in acid solutions. *J. Phys. Chem. B* **1997**, *101* (27), 5405−5413.
(200) Marković, N.; Ross, P., Jr Surface science studies of model fuel cell electrocatalysts. *Surf. Sci. Rep.* **2002**, *45* (4−6), 117−229.
(201) Skúlason, E.; Tripkovic, V.; Björketun, M. E.; Gudmundsdóttir, S.; Karlberg, G.; Rossmeisl, J.; Bligaard, T.; Jónsson, H.; Nørskov, J. K. Modeling the electrochemical hydrogen oxidation and evolution reactions on the basis of density functional theory calculations. *J. Phys. Chem. C* **2010**, *114* (42), 18182−18197.
(202) Tang, M. T.; Liu, X.; Ji, Y.; Norskov, J. K.; Chan, K. Modeling Hydrogen Evolution Reaction Kinetics through Explicit Water-Metal Interfaces. *J. Phys. Chem. C* **2020**, *124* (51), 28083−28092.
(203) Surendralal, S.; Todorova, M.; Neugebauer, J. Impact of Water Coadsorption on the Electrode Potential of H-Pt(1 1 1)-Liquid Water Interfaces. *Phys. Rev. Lett.* **2021**, *126* (16), 166802.
(204) Kronberg, R.; Laasonen, K. Coupling surface coverage and electrostatic effects on the interfacial adlayer-water structure of hydrogenated single-crystal platinum electrodes. *J. Phys. Chem. C* **2020**, *124* (25), 13706−13714.
(205) Hansen, J. N.; Prats, H.; Toudahl, K. K.; Mørch Secher, N.; Chan, K.; Kibsgaard, J.; Chorkendorff, I. Is there anything better than Pt for HER? *ACS energy letters* **2021**, *6* (4), 1175−1180.
(206) Durst, J.; Simon, C.; Hasché, F.; Gasteiger, H. A. Hydrogen Oxidation and Evolution Reaction Kinetics on Carbon Supported Pt, Ir, Rh, and Pd Electrocatalysts in Acidic Media. *J. Electrochem. Soc.* **2015**, *162* (1), F190.
(207) Sun, Y.; Lu, J.; Zhuang, L. Rational determination of exchange current density for hydrogen electrode reactions at carbon-supported Pt catalysts. *Electrochim. Acta* **2010**, *55* (3), 844−850.
(208) He, Z.-D.; Wei, J.; Chen, Y.-X.; Santos, E.; Schmickler, W. Hydrogen evolution at Pt (111)-activation energy, frequency factor and hydrogen repulsion. *Electrochim. Acta* **2017**, *255*, 391−395.
(209) Zeradjanin, A. R.; Narangoda, P.; Masa, J.; Schlögl, R. What Controls Activity Trends of Electrocatalytic Hydrogen Evolution Reaction? Activation Energy Versus Frequency Factor. *ACS Catal.* **2022**, *12* (19), 11597−11605.
(210) Van den Bossche, M.; Skúlason, E.; Rose-Petruck, C.; Jónsson, H. Assessment of constant-potential implicit solvation calculations of electrochemical energy barriers for H2 evolution on Pt. *J. Phys. Chem. C* **2019**, *123* (7), 4116−4124.
(211) Lindgren, P.; Kastlunger, G.; Peterson, A. A. A challenge to the G∼ 0 interpretation of hydrogen evolution. *ACS Catal.* **2020**, *10* (1), 121−128.
(212) Kronberg, R.; Laasonen, K. Reconciling the experimental and computational hydrogen evolution activities of Pt (111) through DFT-based constrained MD simulations. *ACS Catal.* **2021**, *11* (13), 8062−8078.
(213) Dubouis, N.; Grimaud, A. The hydrogen evolution reaction: from material to interfacial descriptors. *Chemical Science* **2019**, *10* (40), 9165−9181.
(214) Intikhab, S.; Snyder, J. D.; Tang, M. H. Adsorbed Hydroxide Does Not Participate in the Volmer Step of Alkaline Hydrogen Electrocatalysis. *ACS Catal.* **2017**, *7* (12), 8314−8319.
(215) Durst, J.; Siebel, A.; Simon, C.; Hasché, F.; Herranz, J.; Gasteiger, H. A. New insights into the electrochemical hydrogen oxidation and evolution reaction mechanism. *Energy Environ. Sci.* **2014**, *7* (7), 2255−2260.
(216) Shinagawa, T.; Garcia-Esparza, A. T.; Takanabe, K. Insight on Tafel slopes from a microkinetic analysis of aqueous electrocatalysis for energy conversion. *Sci. Rep.* **2015**, *5* (1), 13801.
(217) Schmidt, T.; Ross, P., Jr; Markovic, N. Temperature dependent surface electrochemistry on Pt single crystals in alkaline electrolytes: Part 2. The hydrogen evolution/oxidation reaction. *J. Electroanal. Chem.* **2002**, *524*, 252−260.
(218) Li, J.; Stenlid, J. H.; Ludwig, T.; Lamoureux, P. S.; Abild-Pedersen, F. Modeling potential-dependent electrochemical activation barriers: revisiting the alkaline hydrogen evolution reaction. *J. Am. Chem. Soc.* **2021**, *143* (46), 19341−19355.
(219) Xue, S.; Garlyyev, B.; Watzele, S.; Liang, Y.; Fichtner, J.; Pohl, M. D.; Bandarenka, A. S. Influence of Alkali Metal Cations on the Hydrogen Evolution Reaction Activity of Pt, Ir, Au, and Ag Electrodes in Alkaline Electrolytes. *ChemElectroChem.* **2018**, *5* (17), 2326−2329.
(220) Le, J.-B.; Chen, A.; Kuang, Y.; Cheng, J. Molecular understanding of cation effects on double layer and its significance to CO-CO dimerization. *Natl. Sci. Rev.* **2023**, *10* (9), nwad105.
(221) Shah, A. H.; Zhang, Z.; Huang, Z.; Wang, S.; Zhong, G.; Wan, C.; Alexandrova, A. N.; Huang, Y.; Duan, X. The role of alkali metal cations and platinum-surface hydroxyl in the alkaline hydrogen evolution reaction. *Nature Catalysis* **2022**, *5* (10), 923−933.
(222) Strmcnik, D.; van der Vliet, D. F.; Chang, K. C.; Komanicky, V.; Kodama, K.; You, H.; Stamenkovic, V. R.; Marković, N. M. Effects of Li +, K+, and Ba2+ Cations on the ORR at Model and High Surface Area Pt and Au Surfaces in Alkaline Solutions. *J. Phys. Chem. Lett.* **2011**, *2* (21), 2733−2736.
(223) Liu, E.; Li, J.; Jiao, L.; Doan, H. T. T.; Liu, Z.; Zhao, Z.; Huang, Y.; Abraham, K. M.; Mukerjee, S.; Jia, Q. Unifying the Hydrogen Evolution and Oxidation Reactions Kinetics in Base by Identifying the Catalytic Roles of Hydroxyl-Water-Cation Adducts. *J. Am. Chem. Soc.* **2019**, *141* (7), 3232−3239.
(224) Monteiro, M. C. O.; Goyal, A.; Moerland, P.; Koper, M. T. M. Understanding Cation Trends for Hydrogen Evolution on Platinum and Gold Electrodes in Alkaline Media. *ACS Catal.* **2021**, *11* (23), 14328−14335.


https://doi.org/10.1021/acs.chemrev.3c00735
*Chem. Rev.* 2024, 124, 8620−8656

(225) Watkins, N. B.; Schiffer, Z. J.; Lai, Y.; Musgrave, C. B., Jr; Atwater, H. A.; Goddard, W. A., Jr; Agapie, T.; Peters, J. C.; Gregoire, J. M. Hydrodynamics Change Tafel Slopes in Electrochemical CO2 Reduction on Copper. *ACS Energy Lett.* **2023**, *8* (5), 2185−2192.
(226) Bergmann, A.; Jones, T. E.; Martinez Moreno, E.; Teschner, D.; Chernev, P.; Gliech, M.; Reier, T.; Dau, H.; Strasser, P. Unified structural motifs of the catalytically active state of Co(oxyhydr)oxides during the electrochemical oxygen evolution reaction. *Nature Catalysis* **2018**, *1* (9), 711−719.
(227) Mostafa, S.; Behafarid, F.; Croy, J. R.; Ono, L. K.; Li, L.; Yang, J. C.; Frenkel, A. I.; Cuenya, B. R. Shape-Dependent Catalytic Properties of Pt Nanoparticles. *J. Am. Chem. Soc.* **2010**, *132* (44), 15714−15719.
(228) Timoshenko, J.; Keller, K. R.; Frenkel, A. I. Determination of bimetallic architectures in nanometer-scale catalysts by combining molecular dynamics simulations with x-ray absorption spectroscopy. *J. Chem. Phys.* **2017**, *146* (11), 114201.
(229) Timoshenko, J.; Lu, D.; Lin, Y.; Frenkel, A. I. Supervised machine-learning-based determination of three-dimensional structure of metallic nanoparticles. *journal of physical chemistry letters* **2017**, *8* (20), 5091−5098.
(230) Pourbaix, M. J. N. *Atlas of Electrochemical Equilibria in Aqueous Solutions*; National Association of Corrosion, 1974.
(231) Di Liberto, G.; Giordano, L.; Pacchioni, G. Predicting the Stability of Single-Atom Catalysts in Electrochemical Reactions. *ACS Catal.* **2024**, *14* (1), 45−55.
(232) Persson, K. A.; Waldwick, B.; Lazic, P.; Ceder, G. Prediction of solid-aqueous equilibria: Scheme to combine first-principles calculations of solids with experimental aqueous states. *Phys. Rev. B* **2012**, *85* (23), 235438.
(233) Singh, A. K.; Zhou, L.; Shinde, A.; Suram, S. K.; Montoya, J. H.; Winston, D.; Gregoire, J. M.; Persson, K. A. Electrochemical Stability of Metastable Materials. *Chem. Mater.* **2017**, *29* (23), 10159−10167.
(234) Patel, A. M.; Nørskov, J. K.; Persson, K. A.; Montoya, J. H. Efficient Pourbaix diagrams of many-element compounds. *Phys. Chem. Chem. Phys.* **2019**, *21* (45), 25323−25327.
(235) Zagalskaya, A.; Alexandrov, V. Mechanistic Study of IrO2 Dissolution during the Electrocatalytic Oxygen Evolution Reaction. *J. Phys. Chem. Lett.* **2020**, *11* (7), 2695−2700.
(236) Toma, F. M.; Cooper, J. K.; Kunzelmann, V.; McDowell, M. T.; Yu, J.; Larson, D. M.; Borys, N. J.; Abelyan, C.; Beeman, J. W.; Yu, K. M.; et al. Mechanistic insights into chemical and photochemical transformations of bismuth vanadate photoanodes. *Nat. Commun.* **2016**, *7* (1), 12012.
(237) Morankar, A.; Deshpande, S.; Zeng, Z.; Atanassov, P.; Greeley, J. A first principles analysis of potential-dependent structural evolution of active sites in Fe-N-C catalysts. *Proc. Natl. Acad. Sci. U. S. A.* **2023**, *120* (49), No. e2308458120.
(238) Lavroff, R. H.; Morgan, H. W. T.; Zhang, Z.; Poths, P.; Alexandrova, A. N. Ensemble representation of catalytic interfaces: soloists, orchestras, and everything in-between. *Chem. Sci.* **2022**, *13* (27), 8003−8016.
(239) Sun, G.; Sautet, P. Active Site Fluxional Restructuring as a New Paradigm in Triggering Reaction Activity for Nanocluster Catalysis. *Acc. Chem. Res.* **2021**, *54* (20), 3841−3849.
(240) Shih, A. J.; Monteiro, M. C.; Dattila, F.; Pavesi, D.; Philips, M.; da Silva, A. H.; Vos, R. E.; Ojha, K.; Park, S.; van der Heijden, O.; et al. Water electrolysis. *Nat. Rev. Methods Primers* **2022**, *2* (1), 84.
(241) Monteiro, M. C.; Koper, M. T. Alumina contamination through polishing and its effect on hydrogen evolution on gold electrodes. *Electrochim. Acta* **2019**, *325*, 134915.
(242) Clark, E. L.; Resasco, J.; Landers, A.; Lin, J.; Chung, L.-T.; Walton, A.; Hahn, C.; Jaramillo, T. F.; Bell, A. T. Standards and protocols for data acquisition and reporting for studies of the electrochemical reduction of carbon dioxide. *ACS Catal.* **2018**, *8* (7), 6560−6570.
(243) Chen, R.; Yang, C.; Cai, W.; Wang, H.-Y.; Miao, J.; Zhang, L.; Chen, S.; Liu, B. Use of platinum as the counter electrode to study the activity of nonprecious metal catalysts for the hydrogen evolution reaction. *ACS energy letters* **2017**, *2* (5), 1070−1075.
(244) Dunwell, M.; Lu, Q.; Heyes, J. M.; Rosen, J.; Chen, J. G.; Yan, Y.; Jiao, F.; Xu, B. The central role of bicarbonate in the electrochemical reduction of carbon dioxide on gold. *J. Am. Chem. Soc.* **2017**, *139* (10), 3774−3783.
(245) Trotochaud, L.; Young, S. L.; Ranney, J. K.; Boettcher, S. W. Nickel-iron oxyhydroxide oxygen-evolution electrocatalysts: the role of intentional and incidental iron incorporation. *J. Am. Chem. Soc.* **2014**, *136* (18), 6744−6753.
(246) Márquez, R. A.; Kawashima, K.; Son, Y. J.; Castelino, G.; Miller, N.; Smith, L. A.; Chukwuneke, C. E.; Mullins, C. B. Getting the Basics Right: Preparing Alkaline Electrolytes for Electrochemical Applications. *ACS Energy Lett.* **2023**, *8* (2), 1141−1146.
(247) Niu, S.; Li, S.; Du, Y.; Han, X.; Xu, P. How to reliably report the overpotential of an electrocatalyst. *ACS Energy Lett.* **2020**, *5* (4), 1083−1087.
(248) Hausmann, J. N.; Traynor, B.; Myers, R. J.; Driess, M.; Menezes, P. W. The pH of aqueous NaOH/KOH solutions: a critical and non-trivial parameter for electrocatalysis. *ACS Energy Lett.* **2021**, *6* (10), 3567−3571.
(249) Zamora Zeledon, J. A.; Jackson, A.; Stevens, M. B.; Kamat, G. A.; Jaramillo, T. F. Methods—a practical approach to the reversible hydrogen electrode scale. *J. Electrochem. Soc.* **2022**, *169* (6), 066505.
(250) Wei, C.; Rao, R. R.; Peng, J.; Huang, B.; Stephens, I. E.; Risch, M.; Xu, Z. J.; Shao-Horn, Y. Recommended practices and benchmark activity for hydrogen and oxygen electrocatalysis in water splitting and fuel cells. *Adv. Mater.* **2019**, *31* (31), 1806296.
(251) McCrory, C. C.; Jung, S.; Ferrer, I. M.; Chatman, S. M.; Peters, J. C.; Jaramillo, T. F. Benchmarking hydrogen evolving reaction and oxygen evolving reaction electrocatalysts for solar water splitting devices. *J. Am. Chem. Soc.* **2015**, *137* (13), 4347−4357.
(252) McCrory, C. C.; Jung, S.; Peters, J. C.; Jaramillo, T. F. Benchmarking heterogeneous electrocatalysts for the oxygen evolution reaction. *J. Am. Chem. Soc.* **2013**, *135* (45), 16977−16987.
(253) Boudart, M. Turnover rates in heterogeneous catalysis. *Chem. Rev.* **1995**, *95* (3), 661−666.
(254) Kibsgaard, J.; Nørskov, J. K.; Chorkendorff, I. The difficulty of proving electrochemical ammonia synthesis. *ACS Energy Lett.* **2019**, *4* (12), 2986−2988.
(255) Andersen, S. Z.; Čolić, V.; Yang, S.; Schwalbe, J. A.; Nielander, A. C.; McEnaney, J. M.; Enemark-Rasmussen, K.; Baker, J. G.; Singh, A. R.; Rohr, B. A.; et al. A rigorous electrochemical ammonia synthesis protocol with quantitative isotope measurements. *Nature* **2019**, *570* (7762), 504−508.
(256) Moniri, S.; Van Cleve, T.; Linic, S. Pitfalls and best practices in measurements of the electrochemical surface area of platinum-based nanostructured electro-catalysts. *J. Catal.* **2017**, *345*, 1−10.
(257) Trasatti, S.; Petrii, O. Real surface area measurements in electrochemistry. *J. Electroanal. Chem.* **1992**, *327* (1−2), 353−376.
(258) Yoon, Y.; Yan, B.; Surendranath, Y. Suppressing Ion Transfer Enables Versatile Measurements of Electrochemical Surface Area for Intrinsic Activity Comparisons. *J. Am. Chem. Soc.* **2018**, *140* (7), 2397−2400.
(259) Madon, R. J.; Boudart, M. Experimental criterion for the absence of artifacts in the measurement of rates of heterogeneous catalytic reactions. *Industrial & Engineering Chemistry Fundamentals* **1982**, *21*, 438−447.
(260) Chung, D. Y.; Park, S.; Lopes, P. P.; Stamenkovic, V. R.; Sung, Y.-E.; Markovic, N. M.; Strmcnik, D. Electrokinetic analysis of poorly conductive electrocatalytic materials. *ACS Catal.* **2020**, *10* (9), 4990−4996.
(261) Nørskov, J. K.; Bligaard, T.; Rossmeisl, J.; Christensen, C. H. Towards the computational design of solid catalysts. *Nature Chem.* **2009**, *1* (1), 37−46.
(262) Nørskov, J. K.; Abild-Pedersen, F.; Studt, F.; Bligaard, T. Density functional theory in surface chemistry and catalysis. *Proc. Natl. Acad. Sci. U. S. A.* **2011**, *108* (3), 937−943.
(263) Ulissi, Z. W.; Tang, M. T.; Xiao, J.; Liu, X.; Torelli, D. A.; Karamad, M.; Cummins, K.; Hahn, C.; Lewis, N. S.; Jaramillo, T. F.; et al. Machine-learning methods enable exhaustive searches for active


https://doi.org/10.1021/acs.chemrev.3c00735
*Chem. Rev.* 2024, 124, 8620−8656

bimetallic facets and reveal active site motifs for CO2 reduction. *ACS Catal.* **2017**, *7* (10), 6600−6608.
(264) Takeno, N. Atlas of Eh-pH diagrams. *Geological Survey of Japan Open File Report No. 419*; National Institute of Advanced Industrial Science and Technology Research Center for Deep Geological Environments, Naoto Takeno, 2005.
(265) Danilovic, N.; Subbaraman, R.; Chang, K.-C.; Chang, S. H.; Kang, Y. J.; Snyder, J.; Paulikas, A. P.; Strmcnik, D.; Kim, Y.-T.; Myers, D.; et al. Activity-stability trends for the oxygen evolution reaction on monometallic oxides in acidic environments. *J. Phys. Chem. Lett.* **2014**, *5* (14), 2474−2478.
(266) Jin, S. Are metal chalcogenides, nitrides, and phosphides oxygen evolution catalysts or bifunctional catalysts? *ACS Energy Lett.* **2017**, *2*, 1937−1938.
(267) May, K. J.; Carlton, C. E.; Stoerzinger, K. A.; Risch, M.; Suntivich, J.; Lee, Y.-L.; Grimaud, A.; Shao-Horn, Y. Influence of oxygen evolution during water oxidation on the surface of perovskite oxide catalysts. *journal of physical chemistry letters* **2012**, *3* (22), 3264−3270.
(268) Geiger, S.; Kasian, O.; Ledendecker, M.; Pizzutilo, E.; Mingers, A. M.; Fu, W. T.; Diaz-Morales, O.; Li, Z.; Oellers, T.; Fruchter, L.; et al. The stability number as a metric for electrocatalyst stability benchmarking. *Nat. Catal.* **2018**, *1* (7), 508−515.
(269) Hochfilzer, D.; Chorkendorff, I.; Kibsgaard, J. Catalyst Stability Considerations for Electrochemical Energy Conversion with Non-Noble Metals: Do We Measure on What We Synthesized? *ACS Energy Lett.* **2023**, *8* (3), 1607−1612.
(270) Wang, Z.; Zheng, Y.-R.; Montoya, J.; Hochfilzer, D.; Cao, A.; Kibsgaard, J.; Chorkendorff, I.; Nørskov, J. K. Origins of the instability of nonprecious hydrogen evolution reaction catalysts at open-circuit potential. *ACS Energy Lett.* **2021**, *6* (6), 2268−2274.
(271) Resasco, J.; Abild-Pedersen, F.; Hahn, C.; Bao, Z.; Koper, M. T.; Jaramillo, T. F. Enhancing the connection between computation and experiments in electrocatalysis. *Nature Catalysis* **2022**, *5* (5), 374−381.
(272) Holewinski, A.; Linic, S. Elementary Mechanisms in Electrocatalysis: Revisiting the ORR Tafel Slope. *J. Electrochem. Soc.* **2012**, *159* (11), H864.
(273) Limaye, A. M.; Zeng, J. S.; Willard, A. P.; Manthiram, K. Bayesian data analysis reveals no preference for cardinal Tafel slopes in CO2 reduction electrocatalysis. *Nat. Commun.* **2021**, *12* (1), 703.
(274) Yang, Y.; Xiong, Y.; Zeng, R.; Lu, X.; Krumov, M.; Huang, X.; Xu, W.; Wang, H.; DiSalvo, F. J.; Brock, J. D.; et al. Operando methods in electrocatalysis. *ACS Catal.* **2021**, *11* (3), 1136−1178.
(275) Colic, V.; Pohl, M. D.; Scieszka, D.; Bandarenka, A. S. Influence of the electrolyte composition on the activity and selectivity of electrocatalytic centers. *Catal. Today* **2016**, *262*, 24−35.
(276) Strmcnik, D.; Kodama, K.; van der Vliet, D. v. d.; Greeley, J.; Stamenkovic, V. R.; Marković, N. The role of non-covalent interactions in electrocatalytic fuel-cell reactions on platinum. *Nature Chem.* **2009**, *1* (6), 466−472.
(277) McCrum, I. T.; Janik, M. J. pH and alkali cation effects on the Pt cyclic voltammogram explained using density functional theory. *J. Phys. Chem. C* **2016**, *120* (1), 457−471.
(278) Ledezma-Yanez, I.; Wallace, W. D. Z.; Sebastián-Pascual, P.; Climent, V.; Feliu, J. M.; Koper, M. Interfacial water reorganization as a pH-dependent descriptor of the hydrogen evolution rate on platinum electrodes. *Nat. Energy* **2017**, *2* (4), 1−7.
(279) Resasco, J.; Lum, Y.; Clark, E.; Zeledon, J. Z.; Bell, A. T. Effects of anion identity and concentration on electrochemical reduction of CO2. *ChemElectroChem.* **2018**, *5* (7), 1064−1072.
(280) Roy, C.; Rao, R. R.; Stoerzinger, K. A.; Hwang, J.; Rossmeisl, J.; Chorkendorff, I.; Shao-Horn, Y.; Stephens, I. E. Trends in activity and dissolution on RuO2 under oxygen evolution conditions: particles versus well-defined extended surfaces. *ACS Energy Lett.* **2018**, *3* (9), 2045−2051.
(281) Stoerzinger, K. A.; Rao, R. R.; Wang, X. R.; Hong, W. T.; Rouleau, C. M.; Shao-Horn, Y. The role of Ru redox in pH-dependent oxygen evolution on rutile ruthenium dioxide surfaces. *Chem.* **2017**, *2* (5), 668−675.
(282) Stoerzinger, K. A.; Diaz-Morales, O.; Kolb, M.; Rao, R. R.; Frydendal, R.; Qiao, L.; Wang, X. R.; Halck, N. B.; Rossmeisl, J.; Hansen, H. A.; et al. Orientation-dependent oxygen evolution on RuO2 without lattice exchange. *ACS Energy Lett.* **2017**, *2* (4), 876−881.
(283) Stoerzinger, K. A.; Qiao, L.; Biegalski, M. D.; Shao-Horn, Y. Orientation-dependent oxygen evolution activities of rutile IrO2 and RuO2. *journal of physical chemistry letters* **2014**, *5* (10), 1636−1641.
(284) Rao, R. R.; Kolb, M. J.; Halck, N. B.; Pedersen, A. F.; Mehta, A.; You, H.; Stoerzinger, K. A.; Feng, Z.; Hansen, H. A.; Zhou, H.; et al. Towards identifying the active sites on RuO2(110) in catalyzing oxygen evolution. *Energy Environ. Sci.* **2017**, *10* (12), 2626−2637.
(285) Sun, Q.; Chan, G. K.-L. Quantum Embedding Theories. *Acc. Chem. Res.* **2016**, *49* (12), 2705−2712.
(286) Libisch, F.; Huang, C.; Carter, E. A. Embedded Correlated Wavefunction Schemes: Theory and Applications. *Acc. Chem. Res.* **2014**, *47* (9), 2768−2775.
(287) Lei, J.; Zhu, T. Impact of Potential and Active-Site Environment on Single-Iron-Atom-Catalyzed Electrochemical CO2 Reduction from Accurate Quantum Many-Body Simulations. *ACS Catal.* **2024**, *14*, 3933−3942.
(288) Zhao, Q.; Martirez, J. M. P.; Carter, E. A. Revisiting Understanding of Electrochemical CO2 Reduction on Cu(111): Competing Proton-Coupled Electron Transfer Reaction Mechanisms Revealed by Embedded Correlated Wavefunction Theory. *J. Am. Chem. Soc.* **2021**, *143* (16), 6152−6164.
(289) Zhao, Q.; Martirez, J. M. P.; Carter, E. A. Charting C-C coupling pathways in electrochemical CO2 reduction on Cu(111) using embedded correlated wavefunction theory. *Proc. Natl. Acad. Sci. U. S. A.* **2022**, *119* (44), No. e2202931119.
(290) Chen, Z.; Liu, Z.; Xu, X. Accurate descriptions of molecule-surface interactions in electrocatalytic CO2 reduction on the copper surfaces. *Nat. Commun.* **2023**, *14* (1), 936.
(291) Liu, Z.; Chen, Z.; Xu, X. Accurate descriptions of molecule-surface interactions for understanding CO2 capture by MgO-based sorbents in wet conditions. *Carbon Capture Science & Technology* **2023**, *9*, 100148.
(292) Unke, O. T.; Chmiela, S.; Sauceda, H. E.; Gastegger, M.; Poltavsky, I.; Schütt, K. T.; Tkatchenko, A.; Müller, K.-R. Machine Learning Force Fields. *Chem. Rev.* **2021**, *121* (16), 10142−10186.
(293) Vandermause, J.; Xie, Y.; Lim, J. S.; Owen, C. J.; Kozinsky, B. Active learning of reactive Bayesian force fields applied to heterogeneous catalysis dynamics of H/Pt. *Nat. Commun.* **2022**, *13* (1), 5183.
(294) Jinnouchi, R.; Karsai, F.; Kresse, G. On-the-fly machine learning force field generation: Application to melting points. *Phys. Rev. B* **2019**, *100* (1), 014105.
(295) Wang, C.; Aoyagi, K.; Wisesa, P.; Mueller, T. Lithium Ion Conduction in Cathode Coating Materials from On-the-Fly Machine Learning. *Chem. Mater.* **2020**, *32* (9), 3741−3752.
(296) Quaranta, V.; Behler, J.; Hellström, M. Structure and Dynamics of the Liquid-Water/Zinc-Oxide Interface from Machine Learning Potential Simulations. *J. Phys. Chem. C* **2019**, *123* (2), 1293−1304.
(297) Calegari Andrade, M. F.; Ko, H.-Y.; Zhang, L.; Car, R.; Selloni, A. Free energy of proton transfer at the water-TiO2 interface from ab initio deep potential molecular dynamics. *Chemical Science* **2020**, *11* (9), 2335−2341.
(298) Anstine, D. M.; Isayev, O. Machine Learning Interatomic Potentials and Long-Range Physics. *J. Phys. Chem. A* **2023**, *127* (11), 2417−2431.
(299) Poltavsky, I.; Tkatchenko, A. Machine Learning Force Fields: Recent Advances and Remaining Challenges. *J. Phys. Chem. Lett.* **2021**, *12* (28), 6551−6564.
(300) Lejaeghere, K.; Bihlmayer, G.; Björkman, T.; Blaha, P.; Blügel, S.; Blum, V.; Caliste, D.; Castelli, I. E.; Clark, S. J.; Dal Corso, A.; et al. Reproducibility in density functional theory calculations of solids. *Science* **2016**, *351* (6280), aad3000.
(301) Jain, A.; Ong, S. P.; Hautier, G.; Chen, W.; Richards, W. D.; Dacek, S.; Cholia, S.; Gunter, D.; Skinner, D.; Ceder, G.; et al.

Commentary: The Materials Project: A materials genome approach to accelerating materials innovation. *APL Mater.* **2013**, *1*, 011002.
(302) Kas, J.; Vila, F.; Pemmaraju, C.; Tan, T.; Rehr, J. Advanced calculations of X-ray spectroscopies with FEFF10 and Corvus. *Journal of Synchrotron Radiation* **2021**, *28* (6), 1801−1810.
(303) Carbone, M. R.; Meng, F.; Vorwerk, C.; Maurer, B.; Peschel, F.; Qu, X.; Stavitski, E.; Draxl, C.; Vinson, J.; Lu, D. Lightshow: a Python package for generating computational x-ray absorption spectroscopy input files. *Journal of Open Source Software* **2023**, *8* (87), 5182.
(304) Torrisi, S. B.; Carbone, M. R.; Rohr, B. A.; Montoya, J. H.; Ha, Y.; Yano, J.; Suram, S. K.; Hung, L. Random forest machine learning models for interpretable X-ray absorption near-edge structure spectrum-property relationships. *npj Comput. Mater.* **2020**, *6* (1), 109.
(305) Guo, H.; Carbone, M. R.; Cao, C.; Qu, J.; Du, Y.; Bak, S.-M.; Weiland, C.; Wang, F.; Yoo, S.; Artrith, N.; et al. Simulated sulfur K-edge X-ray absorption spectroscopy database of lithium thiophosphate solid electrolytes. *Sci. Data* **2023**, *10* (1), 349.
(306) Chen, Y.; Chen, C.; Zheng, C.; Dwaraknath, S.; Horton, M. K.; Cabana, J.; Rehr, J.; Vinson, J.; Dozier, A.; Kas, J. J.; et al. Database of ab initio L-edge X-ray absorption near edge structure. *Sci. Data* **2021**, *8* (1), 153.
(307) Mathew, K.; Zheng, C.; Winston, D.; Chen, C.; Dozier, A.; Rehr, J. J.; Ong, S. P.; Persson, K. A. High-throughput computational X-ray absorption spectroscopy. *Sci. Data* **2018**, *5* (1), 1−8.
(308) Ghose, A.; Segal, M.; Meng, F.; Liang, Z.; Hybertsen, M. S.; Qu, X.; Stavitski, E.; Yoo, S.; Lu, D.; Carbone, M. R. Uncertainty-aware predictions of molecular x-ray absorption spectra using neural network ensembles. *Physical Review Research* **2023**, *5* (1), 013180.
(309) Carbone, M. R.; Topsakal, M.; Lu, D.; Yoo, S. Machine-learning X-ray absorption spectra to quantitative accuracy. *Physical review letters* **2020**, *124* (15), 156401.
(310) Kwon, H.; Sun, W.; Hsu, T.; Jeong, W.; Aydin, F.; Sharma, S.; Meng, F.; Carbone, M. R.; Chen, X.; Lu, D.; et al. Harnessing Neural Networks for Elucidating X-ray Absorption Structure-Spectrum Relationships in Amorphous Carbon. *J. Phys. Chem. C* **2023**, *127* (33), 16473−16484.
(311) Rankine, C. D.; Madkhali, M. M.; Penfold, T. J. A deep neural network for the rapid prediction of X-ray absorption spectra. *J. Phys. Chem. A* **2020**, *124* (21), 4263−4270.
(312) Rankine, C. D.; Penfold, T. Accurate, affordable, and generalizable machine learning simulations of transition metal x-ray absorption spectra using the XANESNET deep neural network. *J. Chem. Phys.* **2022**, *156* (16), 164102.
(313) Carbone, M. R.; Yoo, S.; Topsakal, M.; Lu, D. Classification of local chemical environments from x-ray absorption spectra using supervised machine learning. *Phys. Rev. Mater.* **2019**, *3* (3), 033604.
(314) Zheng, C.; Chen, C.; Chen, Y.; Ong, S. P. Random forest models for accurate identification of coordination environments from X-ray absorption near-edge structure. *Patterns* **2020**, *1* (2), 100013.
(315) Tetef, S.; Govind, N.; Seidler, G. T. Unsupervised machine learning for unbiased chemical classification in X-ray absorption spectroscopy and X-ray emission spectroscopy. *Phys. Chem. Chem. Phys.* **2021**, *23* (41), 23586−23601.
(316) Xiang, S.; Huang, P.; Li, J.; Liu, Y.; Marcella, N.; Routh, P. K.; Li, G.; Frenkel, A. I. Solving the structure of "single-atom" catalysts using machine learning-assisted XANES analysis. *Phys. Chem. Chem. Phys.* **2022**, *24* (8), 5116−5124.
(317) Routh, P. K.; Liu, Y.; Marcella, N.; Kozinsky, B.; Frenkel, A. I. Latent representation learning for structural characterization of catalysts. *J. Phys. Chem. Lett.* **2021**, *12* (8), 2086−2094.
(318) Liu, Y.; Halder, A.; Seifert, S.; Marcella, N.; Vajda, S.; Frenkel, A. I. Probing active sites in Cu x Pd y cluster catalysts by machine-learning-assisted X-ray absorption spectroscopy. *ACS Appl. Mater. Interfaces* **2021**, *13* (45), 53363−53374.
(319) Guda, A. A.; Guda, S. A.; Martini, A.; Kravtsova, A.; Algasov, A.; Bugaev, A.; Kubrin, S. P.; Guda, L.; Šot, P.; van Bokhoven, J. A.; et al. Understanding X-ray absorption spectra by means of descriptors and machine learning algorithms. *npj Comput. Mater.* **2021**, *7* (1), 203.
(320) Liang, Z.; Carbone, M. R.; Chen, W.; Meng, F.; Stavitski, E.; Lu, D.; Hybertsen, M. S.; Qu, X. Decoding structure-spectrum relationships with physically organized latent spaces. *Phys. Rev. Mater.* **2023**, *7* (5), 053802.


https://doi.org/10.1021/acs.chemrev.3c00735
*Chem. Rev.* 2024, 124, 8620−8656